Prüfkopfpositionsverfolgung durch Auswertung von akustischen Bildfolgen für eine quantitativ bewertbare manuelle Ultraschallprüfung

---

Optical Flow Transducer Position Tracking for Quantitative Manual Ultrasonic Testing

DISSERTATION

zur Erlangung des Grades des
DOKTORS DER INGENIEURWISSENSCHAFTEN
der Naturwissenschaftlich-Technischen Fakultät III
Chemie, Pharmazie, Bio- und Werkstoffwissenschaften
der Universität des Saarlandes

von
Dipl.-Ing Olga Yastrebova

Saarbrücken
2012

Tag des Kolloquiums: 2.11.2012

Dekan:	Prof. Dr. Wilhelm F. Maier
Vorsitzender:	Prof. Dr.-Ing. Markus Stommel
Berichterstatter:	Prof. Dr. rer. nat. Michael Kröning
	Prof. Dr.-Ing. Dirk Bähre
Akad. Mitarbeiter:	Dr.-Ing. Frank Aubertin

Contents

Посвящается сыну и семье

In den Wissenschaften ist viel Gewisses,

sobald man sich von den Ausnahmen nicht irre machen lässt

und die Probleme zu ehren weiß.

Johann Wolfgang von Goethe

Acknowledgements

First of all, I would like to express my deep gratitude to my supervisor Prof. Dr. rer. nat. Michael Kröning for his personal and scientific support, encouragement, and for giving me the opportunity to work with excellent people.

I am very thankful to Prof. Dr.-Ing. Dirk Bähre for his help and for providing me with a good environment and facilities to complete this thesis.

I gratefully acknowledge all the colleagues from the Institute of Production Engineering, Saarland University and Institute of Nondestructive Testing (IZFP-Saarbrücken) for the wonderful atmosphere and time we have spent together.

I am much obliged to all my friends for their continuing help. I give my special thanks to Sergey Pushkarev for his moral support and help.

Finally, I would like to express my heartfelt gratitude to my family for their constant support, endless patience and love, especially to my son Kirill for his faith in me.

Saarbrücken, June 2012

Olga Yastrebova

Abstract

Ultrasonic inspection methods are used to prevent failure of pressurized components. However, flaw evaluation depends on skills of trained inspectors. Automated scanning has become mandatory for more reliable inspection performance. However, manipulator techniques are often not applicable. The control of transducer position during manual scanning could provide an equivalent inspection quality but with the advantage of easy access and scanning. Ultrasonic multi-channel equipment enables real-time imaging of inspection results during scanning. Migration codes reconstruct reflector images with a resolution given by the aperture of the transducer array element. Optical flow algorithm can be applied to identify image changes of sector scan sequences of linear arrays for quantitative transducer motion tracking. These are the basics for the development of an *“Acoustic Mouse”*, so called as analogous to the optical mouse of computer technology.

We developed an optimized optical flow algorithm for linear arrays. By optical flow estimate of sector scan sequences we could demonstrate a transducer positioning accuracy better than half of the wavelength. However, optical flow estimate of noise images requires the use of longitudinal waves and appropriate focusing to reduce the contribution of grain boundary reflection. Further, optical flow images can be used to identify transducer positions after lift-off situations. The time needed for transducer repositioning is in the range of 2 seconds.

Zusammenfassung

Die Ultraschall Impuls-Echo Methode zeichnet sich durch eine hohe Empfindlichkeit beim Nachweis von rißartigen Fehlern aus, die zum Versagen von druckführenden Komponenten führen können. Allerdings kann nur mit großem Aufwand eine hinreichend sichere Aussage über Fehlerart und Größe getroffen werden. Dies führt zur Forderung, kritische Bauteile automatisiert zu prüfen. Eine manuelle Prüfung würde eine Erfassung der Prüfkopfposition erfordern.

Mit Gruppenstrahlern kann ein Reflektorbild in Echtzeit gemessen werden. Für die Rekonstruktion werden Migrationsalgorithmen verwendet, mit denen eine Auflösung bis zu einer halben Wellenlänge erreicht werden kann. Damit sind die Grundlagen gegeben für die Entwicklung einer akustischen Maus, ein Analogon zur optischen Maus der Computertechnik.

Die Tauglichkeit dieses Konzeptes wurde nachgewiesen: ein optimierter Algorithmus zur Bestimmung von Bildänderungen und der anschließenden Prüfkopfpositionsbestimmung wurde entwickelt und experimentell überprüft. Der Algorithmus basiert auf den Prinzipien des optischen Flusses. Die Analyse von Rauschbildern setzt die Verwendung longitudinaler Wellen und eine gute Fokussierung zur Einschränkung des Beitrages der Reflektionen an den Korngrenzen voraus. Die optischen Flußbilder können als Positionssignatur verwendet werden, die nach einer Prüfkopfabhebung das Auffinden der bereits geprüften Positionen ermöglicht. Die erreichten Genauigkeiten liegen im Bereich einer halben Wellenlänge.

Chapter 1. Introduction

The value of nondestructive testing (NDT) is related to the more precise assessment of fitness of purpose of materials, technical components and systems. NDT is a mandatory part of quality control of manufacturing, and pre- and in-service inspections. More recently, NDT is also used for the control of manufacturing processes as part of scrap-free production. We focus on NDT used for the assessment of structural integrity of systems which failure might cause serious damage to humans and environment. Two general NDT parameters determine the value of NDT for structural integrity assessment: the probability of flaw detection (PoD) (Georgiou, 2006), (Rummel, 2008) and the quantitative evaluation of detected material flaws, their type, geometry, size, and location in the structure geometry (QNDT) (Achenbach, 2000). Both parameters are matter of current and continuing engineering research and development because of missing general procedures.

Especially planar flaws like cracks or lack of fusions in welding increase the risk of failure of a structure under load because of their stress intensifying effect. They must be detected for the assessment of the remaining risk of structure failure. Ultrasonic testing (UT) enables a good detection of this type of flaw even at non-accessible surfaces or when flaws are buried in the structure volume. Contrary to most of the alternative nondestructive testing methods acoustic UT is sensing also closed planar defects even when residual stress state may compress the flaw faces up to the elastic limit. We may express this feature of UT by the term *contrast sensitivity* for planar defects.

However, the excellent contrast sensitivity of UT is counterbalanced by two problems. UT is a scanning nondestructive testing method, and the evaluation of inspection results is based on a rather simple correlation of reflector amplitudes measured as time signals (A-Scan). The A-Scans are calibrated using reference reflectors like notches, side drilled (SDH) or flat bottom holes (FBH). Most commonly, manual scanning of UT is applied, and both, PoD and QNDT are limited significantly by the human factor and the weak geometry correlation between reference reflector amplitudes and found flaw amplitudes. Therefore, the remaining risk of failure after inspection can only roughly be assessed by rather conservative upper limit assumptions.

As a result automated UT scanners have become mandatory for the inspection of safety relevant components. Automated scanning enables the 3rd party control of inspection performance, the inspection can be repeated and results can be compared to identify changes of the flaw state. Advanced techniques based on phased array ultrasonic instruments (PA) have improved the contrast sensitivity by the higher number of applicable angle of incidence (Meyer, 2000). The knowledge of accurate transducer position data during scanning enables imaging of UT data. The imaging capacity of PA UT systems can be considered the first but important step towards quantitative ultrasonic testing (QUT).

Very often, mechanical or robotic scanners are just not applicable because of access conditions. Further, the expensive component specific scanner design and the sometimes time consuming assembling of the scanner on the component prevent the use of automated inspection systems. Therefore, manual scanning will be applied also in the future.

1.1. Reason for Research

In consideration of the necessary advances towards QUT realized by automated scanning and reflector imaging but also having in mind the limited use of automated scanners we see the need for manual scanning with implemented QUT features. We assume that the real-time tracking of transducer position during manual scanning is a must for manual QUT with required reporting, imaging, and flaw evaluation features. In the past, several approaches have been made based on external triangulation techniques. One of the earliest systems, SUTARS was developed by Southwest Research Institute, San Antonio, TX, USA already in 1981. These developments stand for the important use of manual UT but with implemented position tracking and recording.

1.2. Motivation

Advanced computing for real-time signal and image processing and latest progress in ultrasonic real-time imaging with array transducers complemented by various advanced robotic tools motivate for a different approach to track and record the transducer location during manual scanning. Just using an optical or laser mouse when working with the PC imparts the expectation that we can extract the position information out of ultrasonic images. Modern laser and optical mice take successive images of the surface on which the mouse operates. As computing power grew, it became possible to embed special-purpose image-processing chips in the mouse itself. This advance enabled the mouse to detect relative motion, translating the movement of the mouse into the movement of the PC cursor.

When by targeted processing of UT images the resulting acoustic image patterns mark the transducer position we may call the technique *"Acoustic Mouse"*. We know that any A-Scan contains information about the transducer position as part of the backscattered acoustic noise. However, this information is covered by common measurement errors, for example by already slightly changed coupling conditions. Therefore, as a basic requirement for the *"Acoustic Mouse"*, we have to filter the error induced changes of the position information.

Figure 1 shows a set of A-Scans measured manually at the same position on a test specimen. The A-scans indicate the problem of reproducing the position signature of A-Scans. Slight changes of the transducer position or of the coupling cause significant changes of the A-scan. Therefore, a direct approach to extract the position information from A-scan data is not promising success. However, processed images like sector scans measured by array transducer offer opportunities for effective filtering. Recent advances in 2D and 3D ultrasonic imaging applying migration codes and beam forming techniques may also anticipate the successful implementation of image processing techniques for transducer position tracking (Bolotina, 2012).

The ultimate goal of the outlined research is a manual ultrasonic testing technique comparable or even equivalent with fully automated ultrasonic inspection systems. The objective of research is the development of an acoustic motion tracking system called *"Acoustic Mouse"* (AM). The *"Acoustic Mouse"* will allow the manual performance of inspection with full information and control on the scanned inspection volume by advanced visualization techniques including high resolution flaw reconstruction.

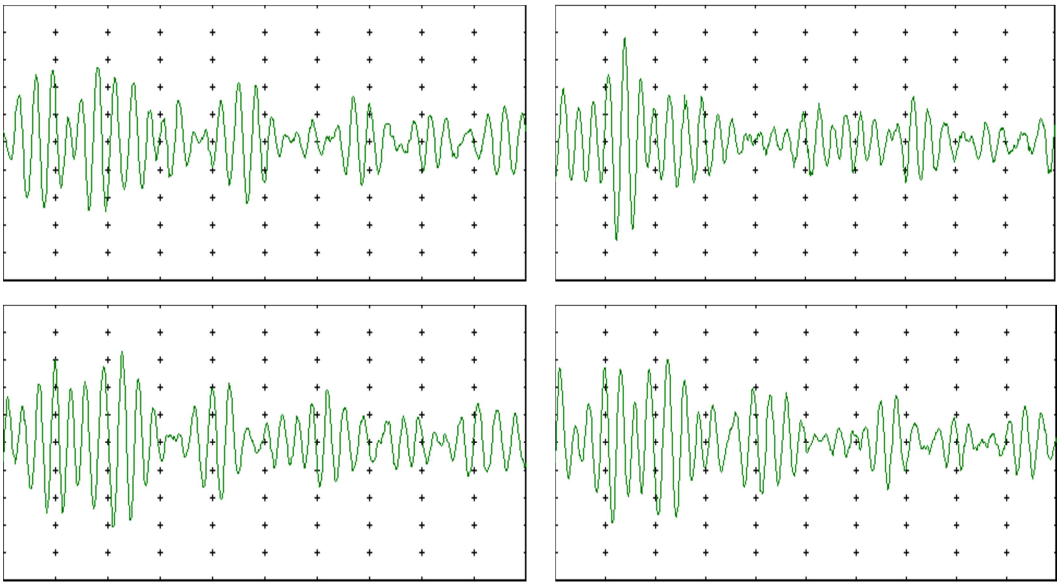

Figure 1: Comparison of RF A-scans measured at the same specimen position (Transducer: 5 MHz Shear Wave 60°).

1.3. Basics of Ultrasonic Testing

We discuss only known and state-of-the-art details of ultrasonic testing when this information is helping for a better understanding of the presented research. In general we refer to NDT engineering textbooks (Krautkrämer, 1990) and NDT handbooks (ASNT).

1.3.1. Pulse-Echo UT Method

The UT method most commonly used for material inspection is the pulse-echo method. This method is an echo-sounder technique. The ultrasonic pulse is usually generated by piezo-electric conversion and is called transmitter pulse. Other conversion techniques like electro-magnetic conversion (EMAT) will not be considered. The pulse propagates through the material that we assume to be isotropic. Part of the acoustic wave is scattered back to the transducer and converted again by the reciprocal piezo-effect. The received electric time signal, the received pulse, is called A-scan. The amplitudes of the A-scan indicate the intensity of reflection that in some way but not well defined correlates with the reflector dimension, the arrival time of reflector amplitudes is used for their localization assuming straight propagation along the center line of the wave field intensity profile. Standard sensitivity setting for reflector detection and reporting references to measured amplitudes of defined calibration reflector geometries, and acceptance criteria consider in addition length or area of localized acoustic reflections and in special cases the systematic appearance.
The use of piezo-transducers has set most of the standards for UT as required by codes and regulations. UT has to be performed in compliance with the ASME code, section V (United States and countries applying the US standards) (ASME, 2010) or following in Europe the EN standards as the normative reference (for example EN 583 Nondestructive Testing – Ultrasonic examination, EN 1712, EN1713, EN 1714: Nondestructive Testing of welds – Ultrasonic testing of welded joints; Acceptance level; characterization of indications in welds; EN 1330-4, EN 12668-1: UT equipment; in Germany: DIN 54 125: manuelle Prüfung von Schweißverbindungen mit Ultraschall).

Here we refer briefly to some of the technical rules that we use for our research for better transparency of our R&D approach.

The transducer aperture forms the acoustic beam by wave interference. Frequency and aperture determine the beam profile with near-field NF (or Fresnel zone), far-field FF (or Fraunhofer zone), beam focus *F*, and beam spread *D* (or divergence). Figure 2 shows a typical ultrasonic beam generated by a piston source transducer with a circular aperture.

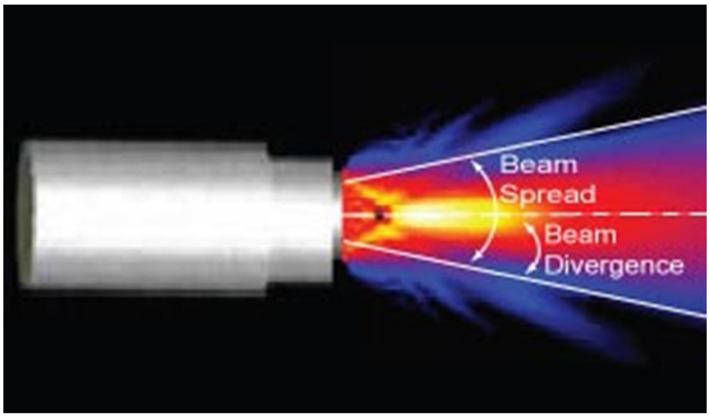

Figure 2: Typical Ultrasonic Sound Field (Larson, 2011).

Figure 3 shows the 2D simulation of the monochromatic 4 MHz beam profile in water transmitted by an aperture of 10 mm. The interference pattern in the near-field including the sound pressure maxima can be clearly seen. The last maxima or the natural transducer focus indicates the end of the near-field with irregular variations of sound pressure. The pressure is presented in logarithmic scale.

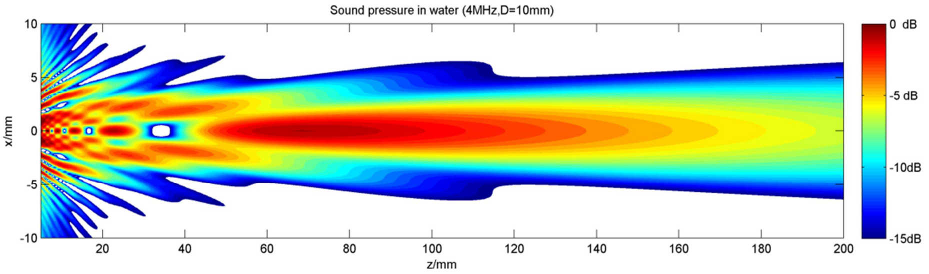

Figure 3: Harmonic Sound Field with Near-field, Natural Focus, and Far field (Wikipedia, 2011).

The end of near-field or near-field distance R_{nf} is given by the expression:

$$R_{nf} = \frac{A^2 - \lambda^2}{4\lambda} \qquad 1.3\text{-}1$$

where A is the source aperture, λ is the wavelength.

The distance of the last pressure maximum is called focal length F, the lateral and the axial 6 dB drop define the focal zone. For flat transducers the focus diameter ϑ and the focal length F are given by the technical estimates:

$$\begin{gathered} \vartheta \sim .26\,A \\ R_{nf} \;\leq\; F \;\leq\; 2R_{nf} \end{gathered} \qquad 1.3\text{-}2$$

When the transducer is rather resonant the near-field cannot be used for reflector detection because of pressure variation. However, broad band pulses average the interference pattern with a resulting homogeneous near-field as Figure 4 is showing.

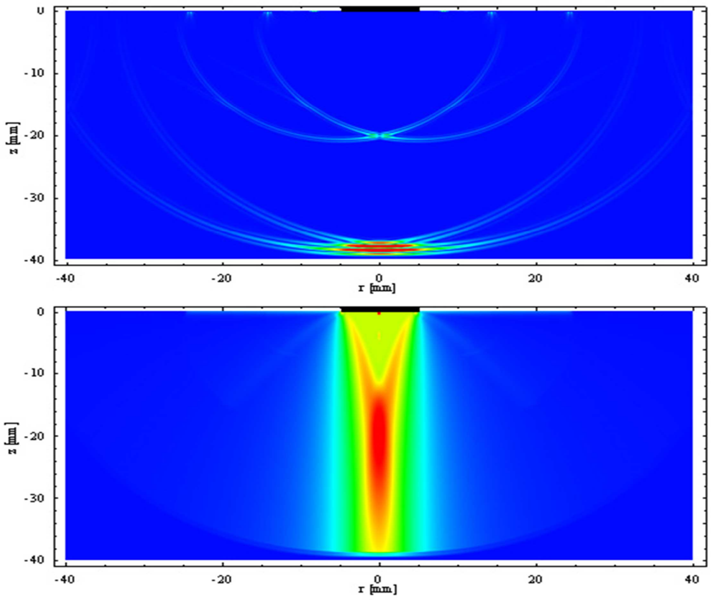

Figure 4: Simulated 2D ultrasonic broad band pulse and intensity profile in steel (A = 10 mm, f = 4 MHz)[1].

At both edges of the aperture shear waves are generated propagating at a speed about half of the longitudinal wave.

As pictures above show, sound propagation is highly directive for standard apertures of around ten wavelengths. For the simulated case of Figure 4 the 10 mm aperture can be expressed by a multiple of wavelengths in steel by:

$$\lambda = \frac{c_l}{f} = 1{,}48\ mm \qquad 1.3\text{-}3$$

$$A = 6{,}7\lambda$$

where c_l – the sound velocity of the longitudinal mode in steel, f – the center frequency.

The dimensioning of extended source aperture is a result of practical engineering. Ultrasound offers the possibility to detect flaws in large components respectively in large distances. Directed beams can localize the flaw much better, and when beam is spread as indicated by the intensity profiles over a large area the acoustic energy eventually dissipates resulting in limited sensitivity for receiving backscattered information about flaws. Further, the use of Huygens point sources with apertures less than half a wavelength would require piezoelectric elements with extremely low capacity values. Low capacity value causes electro-technical problems for the design of effective transmitter and receiver circuits.

The well-known optic laws of diffraction, refraction, and reflection applied to ultrasonic testing are the basis for two fundamental features of ultrasonic testing:

---

[1] *Pictures delivered by Dr. F. Schubert Fraunhofer IZFP - Dresden with appreciation*

For the detection of planar flaws we need normal incidence of the wave field to receive the backscattered reflection. Depending on possible critical flaw geometries and a risk classification of the inspected component the inspection procedure requires various angles of incidence.

The required angle of incidence is realized by plastic wedges of different sound velocity and low attenuation. Snell’s law can be used for the wedge design of the specified angle of sound incidence as long as the beam is directed. A typical angle beam transducer design is shown in Figure 5.

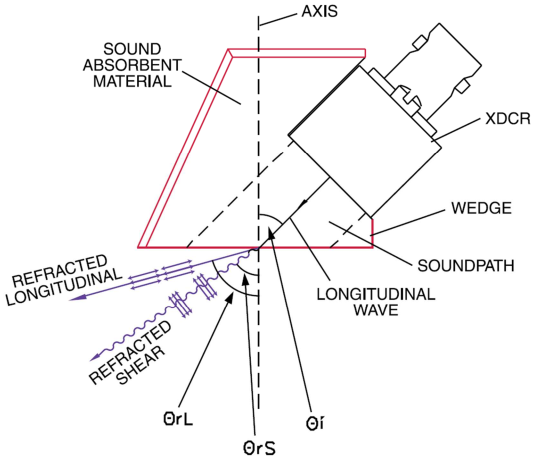

Figure 5: Typical Design of an Angular Beam Transducer (Θi –incident angle of the wedge, ΘrL- angle of the refracted longitudinal wave, ΘrS – angle of the refracted shear wave) (Olympus, 2011)

Both modes, the longitudinal mode (c_l = 5920 mm/sec in steel) and the slower shear mode (c_t = 3250 mm/sec in steel) can be realized by the appropriate wedge design. Above the first critical angle of 90° refracted longitudinal mode only shear waves are transmitted into the specimen.

Reflection, transmission and more general scattering of acoustic waves at a boundary between two materials, also called acoustic interface, are governed by the acoustic impedances Z_1 and Z_2 of the materials. The acoustic impedance Z of a material is defined as the product of its density ρ and sound velocity c.

$$Z = \rho \cdot c \qquad 1.3\text{-}4$$

For any two materials, the reflection coefficient R as a percentage of incident energy pressure may be calculated through the formula

$$R = \frac{Z_2 - Z_1}{Z_2 + Z_1} \qquad 1.3\text{-}5$$

The loss of energy (in dB) on transmitting a signal from medium 1 into medium 2 is given by

$$dB_{loss} = 10 \log_{10} \frac{4Z_1Z_2}{(Z_2 + Z_1)^2} \qquad 1.3\text{-}6$$

For the metal/air boundary the reflection coefficient approaches 100%. Therefore, virtually all of the sound energy is reflected from a crack face in the path of the wave.

The reflection coefficient approaches 100% for the metal/air boundaries commonly seen in ultrasonic flaw detection applications. Therefore, virtually all of the sound energy is reflected from a crack or other discontinuity in the path of the wave. This is the fundamental principle that makes ultrasonic testing highly sensitive for flaw detection.

1.3.2. Ultrasonic Attenuation

Three factors govern the distance a sound wave will travel in a given medium: beam spreading, scattering, and absorption. Attenuation comprises scattering and absorption. *As a general rule, materials that are hard and homogeneous will transmit sound waves more efficiently than those that are soft and heterogeneous or granular* (Olympus, 2011). *"Acoustic Mouse"* will be developed for fine grain isotropic steel as used for pressurized components. There are almost no losses by absorption, and absorption will not contribute to transducer position evaluation. However, since the acoustic image of microstructure given by scattering is supposed to become the signature for transducer tracking we have to understand the nature of acoustic scattering or noise.

1.3.2.1. Scatter Volume

The acoustic beam features focal diameter, beam spread and pulse length (given by the band width) define the volume out of which back-scattered acoustic energy is received by the transducer. As a rule we may assume that the measured acoustic noise decreases with the scatter volume. In the focal zone we get the best sensitivity for geometric reflectors and the best signal-to-noise ratio. Further, when we assess the position signature by image processing, the position is more accurately defined when the axial and lateral scatter volume is limited.

A matter of investigation is the robustness of position measurement since we don't know the contribution of interference and multiple scattering. The relevant theoretical publications (Wang, 1996) make reason for hope that codes will be available in the future to separate the contribution of wave interference and multi-scattering from the scatter compound geometry itself. In consequence, we have to do experiments with slightly changing measurement positions.

In conclusion we expect best results when processing images comprising the focal zone of the transducer. Further, we should only consider todays broad band transducers and small focal diameters that limit the scatter compound volume further. For best focusing up to the Rayleigh limit of half a wave length we will apply array transducers.

1.3.2.2. Nature of Acoustic Scattering

Changes of velocity and/or density at the acoustic interface will cause wave scatter. Most of the metallic structural materials are alloys with microstructure dimensions about fifty times smaller than the applied wavelength. Therefore, the material is acoustically isotropic when the microstructure is composed of grains with stochastic orientation. The sound velocity does not depend on the direction of sound propagation. There are materials with macroscopic grain structures. For example, austenitic weld material consists of columnar grains that cause severe inspection problems by scattering and non-predictable sound propagation (Pudovikov, 2008). Figure 6 shows columnar grains, their orientation and statistical distribution that leads to the transverse acoustic isotropy.

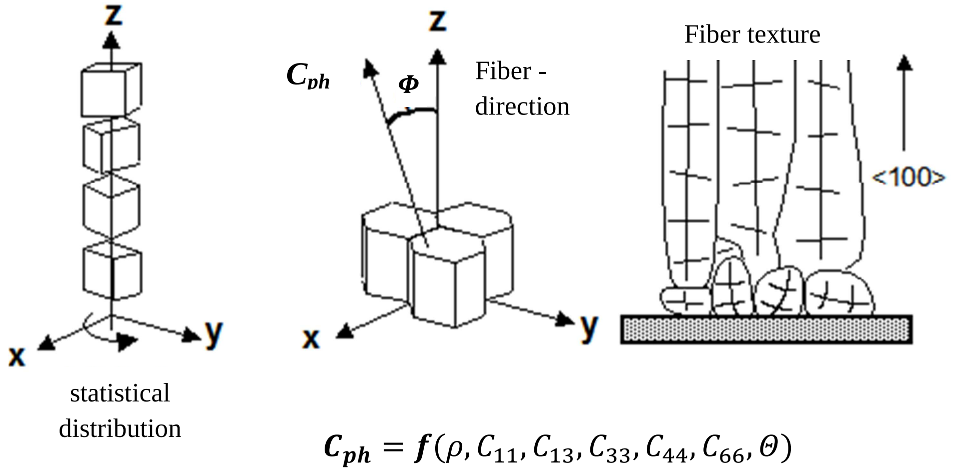

$$\boldsymbol{C_{ph}} = \boldsymbol{f}(\rho, C_{11}, C_{13}, C_{33}, C_{44}, C_{66}, \Theta)$$

C_{ph} - Phase Velocity; C_{ij} - Elastic Constant; ρ - Density, $\boldsymbol{\Phi}$ - Fiber Orientation

Figure 6: Transverse isotropic structure of stainless steel weld joints (Schneiden-Schweißen-Heft-2, 1974), (Pudovikov, 2008)

In anisotropic materials the effects of grain boundary scattering can be observed directly by A-scans. Scatter by fine grain isotropic microstructure appears as noise as shown in Figure 1.

The intensity of back-scattered acoustic noise depends on the acoustic crystal anisotropy that was investigated already about 30 years ago for better understanding of the inspection of austenitic welds (Boehm, 1992). Figure 7 presents qualitatively the changes of phase velocity C_{ph} and group velocity C as a function of the intersection angle with austenitic columnar grains.

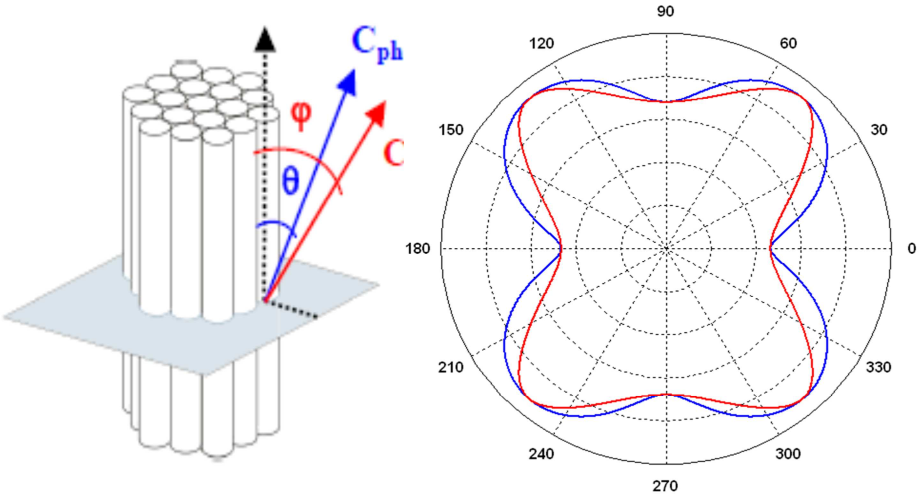

Figure 7: Velocity Changes in Austenitic Columnar Grains

(*Cph* - Phase Velocity; *C* - Group Velocity, *Θ* - Phase Angle, *φ* - Group Angle)

(Boehm, 1992), (Pudovikov, 2010).

During the transition of ultrasonic beam through grain boundaries as acoustic interfaces the wave encounters reflection, refraction and mode conversion, phenomena contributing to the mechanism of scattering. In some general way the attenuation of ultrasound by the microstructure can be correlated to mechanical properties. However, the quality of mechanical property evaluation strictly depends on accurate and careful attenuation measurements (Green, 1981), (Vary, 1988).

Attenuation is denoted by the attenuation coefficient α usually expressed by

$$I = I_0 e^{-\alpha x} \qquad 1.3\text{-}7$$

where I_0 is the initial intensity, x is the distance of wave propagation. The attenuation coefficient α is a function of frequency f. This equation is analogue to the Beer-Lambert law formulation for light absorption. The attenuation can be attributed to different physical processes, the geometric attenuation (α_G), the attenuation due to absorption (α_A), and the attenuation due to scattering (α_S). Thus α can be separated in three components:

$$\alpha = \alpha_G + \alpha_A + \alpha_S \qquad 1.3\text{-}8$$

Geometric attenuation is due to beam spreading. The cross section of a beam expands along the distance of propagation for transducers with finite apertures. Attenuation increases with smaller apertures A and larger wavelengths λ according to:

$$\alpha_G \sim \frac{1.7\lambda}{A^2} \qquad 1.3\text{-}9$$

(for circular flat apertures).

Geometric attenuation must be taken into account for the inspection procedure and determines the transducer and scanning parameters. Therefore, we may not consider further the geometric attenuation as a variable for the *"Acoustic Mouse"* development.

Metallic materials are not strictly homogeneous. Different type of crystal defects can be considered scattering centers:

- Point defects, vacancies, interstitial atoms, solute atoms of an alloying element
- Linear defects, especially dislocations
- Planar defects, interfaces and grain boundaries
- Volume defects, pores, precipitates and inclusions

Point and linear defects normally have stress fields that only extend a few atomic distances. This means that within a few nanometers the disturbance decays in a perfect crystal. This dimension is much smaller than the wavelength of typically used ultrasonic testing frequencies, i.e. 1.18 mm for 5 MHz for a longitudinal wave in steel. Crystal defects in the range between µm and mm are grains, particle inclusions and pores.

In a material, physical properties can have a strong dependence on crystallographic direction. This is called anisotropy. Normally, these differences are averaged out for a polycrystalline material, if all orientations are statistically distributed and the grain size is small. Some manufacturing processes yield microstructures (as shown in Figure 6) with preferred orientations; the material is called textured. Welding, casting and rolling often lead to textures.

The grain boundaries contribute most significantly to the backscattered acoustic noise. For that reason we discuss briefly the elastic anisotropy of materials.

The elastic constants S_{ij} and C_{ij} are called the elastic compliances and elastic stiffnesses, respectively. In the cubic system there are only three independent elastic compliances S_{11}, S_{12}, and S_{44} with corresponding elastic stiffnesses C_{11}, C_{12}, and C_{44}. In a single crystal of a cubic metal the tensile and shear moduli vary with the crystal orientation according to

$$\frac{1}{E} = S_{11} - 2\left[(S_{11} - S_{12}) - \frac{1}{2}S_{44}\right](l^2m^2 + m^2n^2 + l^2n^2)$$

1.3-10

$$\frac{1}{G} = S_{44} - 2\left[(S_{11} - S_{12}) - \frac{1}{2}S_{44}\right](l^2m^2 + m^2n^2 + l^2n^2)$$

where *l*, *m*, *n* are the direction cosines of the specimen axis to the crystallographic axes.

For an isotropic crystal holds:

$$S_{44} = 2(S_{11} - S_{12}) \text{ and } C_{44} = \frac{1}{2}(C_{11} - C_{12}) \qquad 1.3\text{-}11$$

Therefore:

$$E = \frac{1}{S_{11}} \text{ and } G = \frac{1}{S_{44}} \qquad 1.3\text{-}12$$

Hence, the degree of anisotropy can be specified by:

$$\frac{2(S_{11}-S_{12})}{S_{44}} \text{ or } \frac{C_{11}-C_{12}}{2C_{44}} \qquad 1.3\text{-}13$$

In Table 1 we list the principal elastic compliances and elastic stiffnesses at room temperature for Aluminum, Iron, and Copper with their anisotropy factors *g*. The applied units are *1/TPa* for S_{ij} (elastic compliances) and *GPa* for *Cij* (elastic stiffnesses).

	S_{11} [1/TPa]	S_{12} [1/TPa]	S_{44} [1/TPa]	C_{11} [GPa]	C_{12} [GPa]	C_{44} [GPa]	Anisotropy Factor g
Aluminium	16	-5.8	35.3	108	62	28.3	1.2
Iron	7.67	-2.83	8.57	230	117	135	2.5
Copper	15	-6.3	13.3	169	122	75.3	3.2

Table 1: Elastic properties of Al, Fe and Cu (all cubic systems) (Totemeier, 2004).

To some extent the anisotropy factor *g* is related to the applicability of UT. For example, aluminum can be inspected easily, copper with coarse grain or textures needs specific procedures with limited results.

Figure 8 illustrates the anisotropy of several cubic metals. The plot on the left shows the elastic modulus as a function of direction in 3D space, while the plot on the right shows a section through the 3D plot in the *z=0* plane. The anisotropy factor *g* is determined by equation $g = \frac{2(S_{11}-S_{12})}{S_{44}}$.

Aluminium (Al):

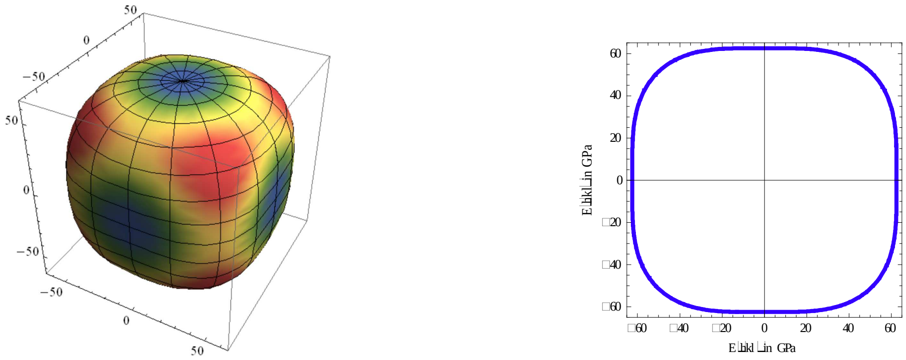

Iron (Fe):

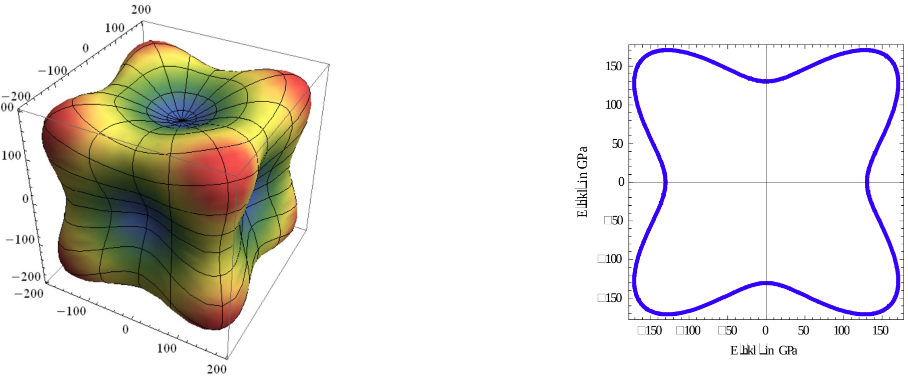

Copper (Cu):

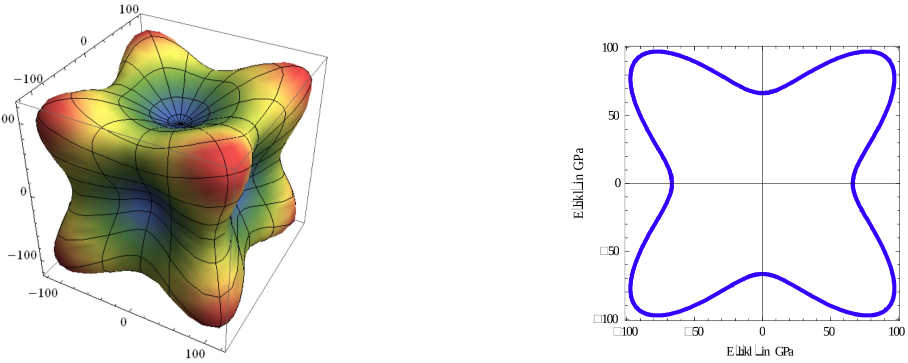

Figure 8: Elastic Moduli as a Function of Crystallographic Direction (Wolfram, 2011).

Scattering in polycrystalline materials caused by crystal anisotropy is given by the following expressions (Mechel, 2008):

$$\alpha_L = \frac{8\pi^3}{375} \cdot \frac{V f^4 g^2}{\rho_0^2 c_l^8} \left[2 + 3 \left(\frac{c_l}{c_t} \right)^5 \right] \qquad 1.3\text{-}14$$

$$\alpha_T = \frac{6\pi^3}{375} \cdot \frac{V f^4 g^2}{\rho_0^2 c_t^8} \left[3 + 2 \left(\frac{c_t}{c_l} \right)^5 \right] \qquad 1.3\text{-}15$$

With the scattering parameters

$$S_L = \frac{8\pi^3}{375} \cdot \frac{g^2}{\rho_0^2 c_l^8} \left[2 + 3 \left(\frac{c_l}{c_t} \right)^5 \right] \qquad \text{(longitudinal mode)} \qquad 1.3\text{-}16$$

$$S_T = \frac{6\pi^3}{375} \cdot \frac{g^2}{\rho_0^2 c_t^8} \left[3 + 2 \left(\frac{c_t}{c_l} \right)^5 \right] \qquad \text{(shear mode)} \qquad 1.3\text{-}17$$

the attenuation coefficient α is written as

$$\alpha_{L,T} = S_{L,T} V f^4 \approx S_{L,T} d^3 f^4 \qquad 1.3\text{-}18$$

where $S_{L,T}$ is the scattering parameter for longitudinal and transverse waves according to the index chosen. The volume of the scatterers is $V \approx d^3$ with d the grain size dimension. α increases significantly with growing frequency f and larger grain size d. Therefore, usually only fine grained steel can be inspected using common technical inspection frequencies in the range of 1 MHz to 5 MHz. Further, scattering of shear waves is much stronger because of its slower sound velocity c_t or smaller wavelength for a given frequency, respectively. The ratio of sound velocities $(c_l/c_t)^5$ is about 32. As a result the attenuation coefficient for shear waves is about one order of magnitude higher than that one for longitudinal waves as shown for some metals in Figure 9.

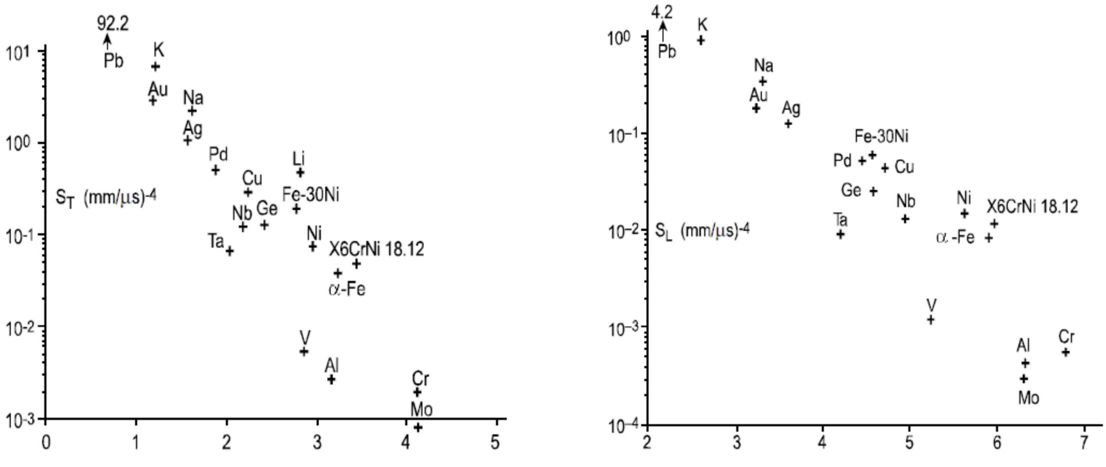

Scattering parameter for shear waves c_t (mm/µs) Scattering parameter for L-waves c_l (mm/µs)

Figure 9: Scattering Parameters for Longitudinal and Shear Waves (Arnold, 2008).

The grain size of technical steels is given by reference micrograph numbers. Table 2 contains the ASTM series of reference diagrams with the average grain diameter and grain cross section. For illustration Figure 10 shows typical austenitic steel micrographs of the three groups of reference micrographs.

a) fine grained b) middle grained c) coarse grained

Figure 10: Micrographs of Austenitic Steel (Lober, 2011).

Grain Size ASTM #	Grain Diameter [µm]	Grain Cross Section [μm^2]	Steel Quality
-3	1000	1.000.000	
-2	800	640.000	
-1	550	302.500	
0	350	122.500	
1	250	62.500	Coarse Grained
2	180	32.400	
3	120	14.400	
4	90	8.100	
5	60	3.600	
6	45	2.025	Fine Grained
7	35	1.225	
8	22	484	
9	16	256	
10	12	144	Very Fine Grained
11	8	64	
12	6	36	
13	4	16	
14	3,5	12	
15	3	9	

Table 2: ASTM Grain Size Reference Series (MPA, 2011).

The ASTM series number N is related to the number of grains G in 1 square inch by

$$G = 2N - 1 \qquad 1.3\text{-}19$$

ASTM grain size number 1 indicates a grain of a cross section of one square inch – a very coarse grained microstructure not testable by ultrasound with commonly required frequencies.

The above considerations are valid for pure poly-crystals. Technical materials contain also other scatter sources – various phases and/or volume defects (voids, inclusions). Nevertheless, we may expect the most significant contribution to scattering in metals by the ratio of mean grain size d to wavelength λ. This ratio has to be considered by NDT practitioners when establishing an inspection procedure. The experimental data as shown in Figure 11 contain all possible scatter sources in steel (Kretov, 1995), (Serabian, 1980).

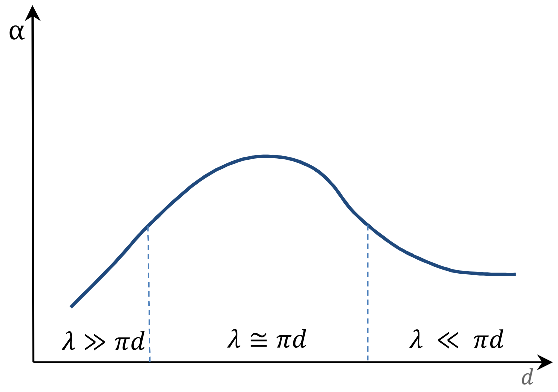

Figure 11: Effect of Grain Size to Wave Length Relation on Ultrasonic Attenuation.

For $\lambda \ll \pi d$, the diffusion scattering, the sound is absorbed in each grain as in one large crystal. Attenuation is defined by absorption:

$$\alpha_D = C_D d^{-1} \tag{1.3-20}$$

For $\lambda \cong \pi d$ we observe the stochastic or phase scattering process:

$$\alpha_p = C_p d f^2 \tag{1.3-21}$$

For $\lambda \gg \pi d$ the Rayleigh scattering process occurs:

$$\alpha_r = C_r d^3 f^4 \tag{1.3-22}$$

C_D, C_p, and C_r are constants of density and elastic anisotropy factors, geometric factors, and velocity (Lifsitz, 1950), (Mason, 1948). For ultrasonic testing frequencies between 0,5 MHz and 10 MHz the wavelength λ is around ten to fifteen times longer than the average grain diameter d. In this interval the ultrasound is weakly scattered and typically there is sufficient high signal to noise ratio for defect detection (Kretov, 1995).

Raleigh scattering forms most of the “acoustic noise” that is usually not evaluated for flaw detection and assessment. However, we assume that the acoustic noise depends on the microstructure that is specific for the position. Geometric extended reflectors are by far more position related and may be evaluated for position data and position changes. However, in high quality steels as used for structures extended material flaws or material inhomogeneity are rather rare. Further, only point reflectors will provide accurate data as required. Back-wall reflection, for example, is independent of the transducer position, and compound reflector geometries, such as crack faces, require careful analysis of the radio frequency (RF) A-scans to separate individual and interfering scatter centers (Yastrebova, 2008). Figure 12 outlines these principles.

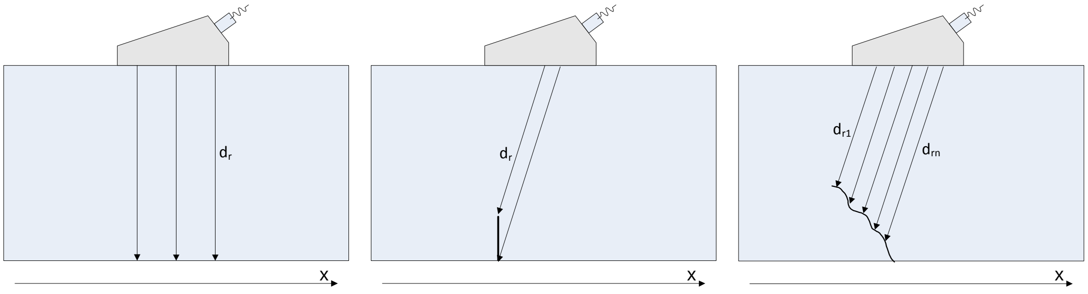

a) Back-wall
$x \neq f(d_r)$

b) Point scattering (crack tip, corner reflector)
$x = f(d_r)$

c) Compound scattering (crack face)
$x \sim r(d_{r1}, d_{r2}, \dots, d_{rn})$

Figure 12: Evaluation of Geometric Scattering for Transducer Position Data
(x: transducer position, d_r: distance to the reflector)

1.3.3. Absorption in Solids

Absorption usually is not contributing to attenuation of ultrasound in steels to be considered. Absorption is due to the wave interaction with the material. Acoustic energy is transformed into other forms of energy, most often heat. Internal friction is one process that contributes to absorption losses. Another process is the direct conversion of sound energy into heat due to thermo-elastic effects, dislocation damping and hysteresis of crystals in material (Kolsky, 1963), (Lücke, 1956).

Direct absorption usually increases with increasing frequency:

$$\alpha_h = C_h f \quad \textit{(Hysteresis losses)} \qquad 1.3\text{-}23$$

$$\alpha_t = C_t f^2 \quad \textit{(Thermoelastic effect)} \qquad 1.3\text{-}24$$

Stress-strain dampening causes hysteresis losses. Thermodynamic losses are a result of heat generation during the transition from dilatation to compression state by longitudinal wave (Mason, 1958).

Scattering and absorption have to be encountered as limiting factors for ultrasonic testing. Absorption is decreasing the amplitude of the acoustic wave. This effect can be compensated by higher transmitter voltage and amplifier settings. In many cases UT procedures have to be qualified by specific choice of transducers for appropriate signal-to-noise ratio. The scattered noise is called “echo grass” by testing engineers. Usually, also lower frequencies have to applied with reduced reflector resolution and sensitivity for the detection of small flaws (Baldev Raj, 2007).

1.3.4. Ultrasonic Arrays

With the progress in micro-electronics and instrument manufacturing, array transducers could be used for material inspections. Array transducers enable significant progress in UT both for improved contrast and for higher resolution sensitivity. They are considered the key to quantitative imaging of flaws (Bolotina, 2012). There are two types of array operation: phase controlled operation and position controlled operation. The phase controlled system is called Phased Array and has become a standard in ultrasonic testing already. The position controlled system is called Migration Array because it uses migration codes for image reconstruction (Bolotina, 2012).

1.3.4.1. Phased Arrays

The active piezo-electronic element of Phased Array transducer is composed of array elements according to the sampling theorem. Phased Array transducers enable electronic control of angle of incidence and focal zone. However, the resulting wave field corresponds completely to the wave field of a standard transducer of same frequency and aperture of same dimensions as the array aperture. In that respect, the use of phased array transducer does not improve the quality of inspection especially not the resolution sensitivity. The number of elements must be higher than 12 for sufficient suppression of diffraction side lobes, the element aperture is half the wave length with a pitch of half a wavelength. However, one phased array transducer can replace several standard transducers with the special advantage of better contrast sensitivity or defect detectability due to the higher number of angles of incidence. Linear phased arrays can be considered part of the current state-of-the-art of ultrasonic automated inspections (Moles, 2007).

Linear arrays sweep respectively focus the ultrasonic beam only in one plane. For 3D sweeps or focusing matrix arrays have to be applied.

Figure 13 shows the basic principle of phase controlled summation of array element A-scans.

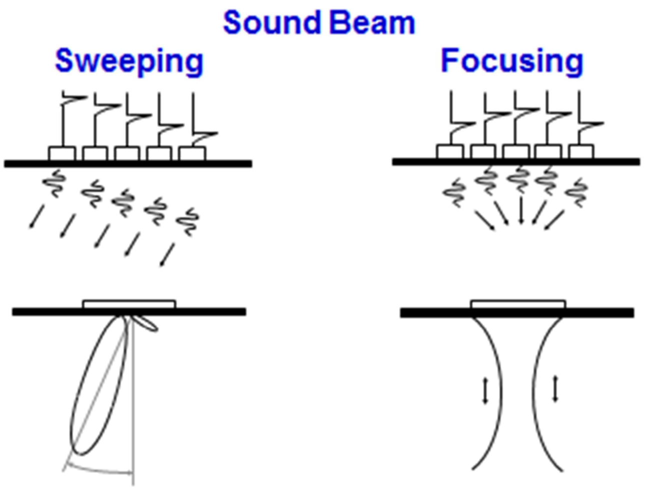

Figure 13: Principle of Phase Controlled Ultrasonic Beams.

The best contrast sensitivity can be achieved by sector scan measurements. A sector scan produces an image that shows a slice through the object being inspected (Figure 14). The angle sweep of the longitudinal wave pulse in Figure 14 was between -70° and +70° with the increment of 2°. Each ray seen in Figure 14a represents the A-scan of a transducer with an aperture size equivalent to the array aperture and the corresponding angle of incidence. Therefore, the focal zone at the end of the near-field that determines the resolution sensitivity is not improved compared with standard single element transducers even when the processed image of Figure 14b looks already impressive.

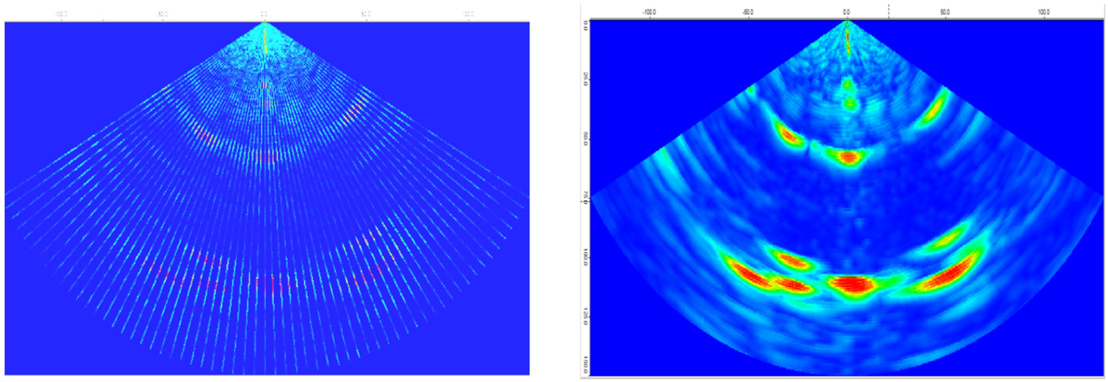

a) Ray Image

b) Processed Image

Figure 14: Phased Array Sector Scans (Bolotina, 2010).

The advantage of phased array transducer is in some way balanced by the complex configuration of the transducer itself. In Figure 15, a radiograph of a linear phased array transducer shows the complex wiring and cabling that limits just by practical aspects the number of elements. Nevertheless, ultrasonic imaging in material inspection has been launched by the use of Phased Array equipment.

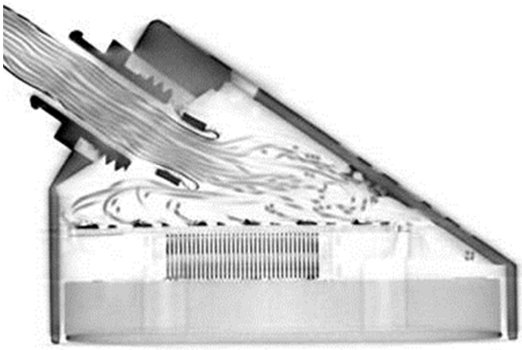

Figure 15: Configuration of a Linear Phased Array Transducer[2].

In industry, PA technicians require more experience and training than conventional technicians. The images of phased array inspections also increase the risk of false evaluation of results when the inspector ignores proved A-scan analysis. The phased array inspection is still a method that applies similar standard principles of single element transducers with aperture limited resolution sensitivity.

1.3.4.2. Migration Arrays

Present-day computing offers the possibility for processing the RF A-scan data of all the array elements in parallel. This type of array technique was called migration array (Bolotina, 2012) because position controlled reconstruction codes of reflectors are applied known for example in Geophysics as migration (Biondi, 2006). The processing of RF A-scans of array elements with known position data is the viable gate to improve contrast and resolution sensitivity but in compliance with reasonable technical complexity of the data acquisition system. The complexity is shifted to signal processing and the codes applied.

Acoustic Migration has become a common principle for the reconstruction of scattering structures in acoustic wave-fields. Different approaches have been developed for different technical problems mainly for seismic exploration. Reverse-time acoustic migration reconstructs the source wave-field forward in time and the receiver wave-field backward in time. It then applies an imaging condition to extract reflectivity information out of the reconstructed wave-fields (Sava, 2008).

The term migration was used in geophysics first time. Migration is the application of a method by which acoustic reflectors can be reconstructed when the acoustic wave field is known at the surface (Gajewski, 2010). When we measure the wave-field $w(x,y,z=0;t)$ at the surface of the specimen we may reconstruct the field $w(x,y,z)$ called depth migration. Depth migration solves the inverse problem of imaging reflector

---

[2] *Radiograph delivered by Fraunhofer IZFP - Dresden with appreciation*

geometries in the volume below the measured wave-field at the surface called aperture or when measured by scanning synthetic aperture.

The application of depth migration in geophysics is directed to measure the structure of the subsoil by seismic waves. This problem is much more complex than reflector imaging in NDT. For example, subsoil structure consists of layers with different acoustic properties, wave velocities have to be assumed and model based corrected for more accurate structure information. In NDT, depth migration usually can be performed under almost ideal conditions: we know the velocity of ultrasound and the surface topography. Subsoil effects like significant attenuation or multi-scattering at layered structures does not complicate depth migration in NDT.

However, we may learn from migration application in geophysics how to inspect structured, anisotropic or dispersive materials.

Migration applied in NDT enables some advanced features of ultrasonic testing that have been developed and demonstrated in the last years (Bulavinov, 2005), (von Bernus, 2006), (Bulavinov, 2007), (Bolotina, 2010), (Bolotina, 2012). The features used for the development of the *“Acoustic Mouse”* are outlined briefly.

The measurement of A-scans by the array elements is position controlled. For each measured A-scan we add the accurate position data of the receiving array element. The material discontinuity is activated by scatter of the transmitter pulse. The scattered pulse is received by all or selected array elements forming a synthetic aperture. The A-scan and position data are stored for further processing. One important feature results from this type of measurement illustrated by Figure 16: There is no need for phase control electronics. The instrument consists of a set of parallel ultrasonic boards with fast data links to the signal processor unit and adequate storage capacity.

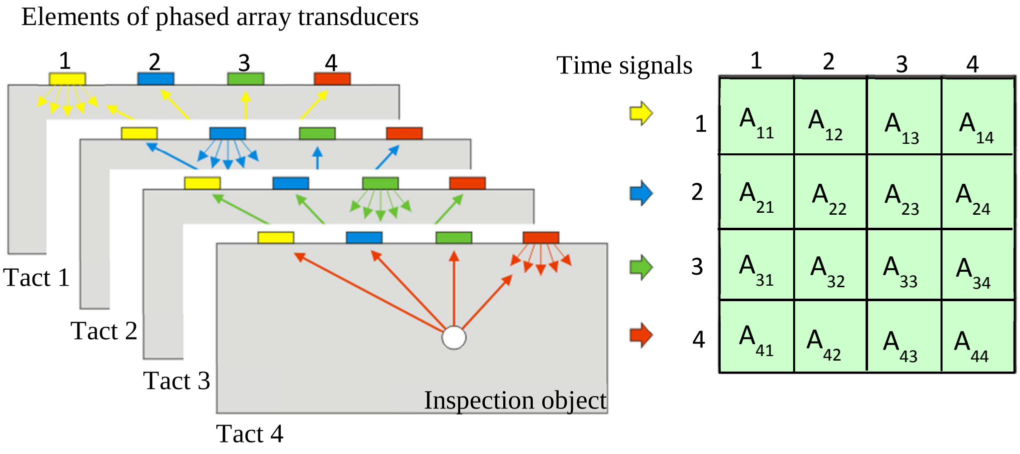

	1	2	3	4
1	A_{11}	A_{12}	A_{13}	A_{14}
2	A_{21}	A_{22}	A_{23}	A_{24}
3	A_{31}	A_{32}	A_{33}	A_{34}
4	A_{41}	A_{42}	A_{43}	A_{44}

a) Sampling Mode of Measurement

b) Information Matrix A_{ij}

Figure 16: Principle of Sampling Arrays and the information matrix of an array with four elements (von Bernus, 2006).

In case that all array elements are used as transmitter but consecutively and all elements are receiving A-scans we have measured the full possible information content of the array as described by the information matrix $A_{i,j}$ with i the number of the transmitting element and j the number of the receiving element. This type of measurement with consecutive transmitter pulses and parallel receiving by all elements is called sampling array because the information provided by ultrasonic array is sampled into the columns $A_{i(j=1\text{-}n)}$.

The information content of an acoustic array of transmitting and receiving elements was described in detail by (Chiao, 1994). Technically we may assume linearity required for the Lorentz Reciprocity Theorem that allows the exchange of transmitter and receiver function (Altman, 1991). Therefore, the full matrix of A-scans comprises redundant information but affected by measurement errors:

$$A_{i,j} = A_{j,i} \quad \textit{(Reciprocity Theorem)} \tag{1.3-25}$$

The redundancy can be used for measurement error averaging and for information matrices build-up by compound scans.

The matrix diagonal $A_{i,j}$ with $i = j$ comprises the information of a synthetic aperture focus scan used as flaw evaluation method SAFT (synthetic aperture focus technique). The element *(1,1)* is moved along the array aperture virtually through the positions *(2,2), (i,i)* up to the position *(n,n)*. Therefore, we may assume that position controlled measurement called here migration measurement provides more information than a SAFT scan when we use the information of matrix elements $A_{i,j}$ with i different from j.

We may state that migration is based on measurement principles commonly known in NDT as SAFT with features known from Phased Arrays. Linear migration arrays of more than 12 elements that follow the Sampling Theorem (skip less than half the wavelength) can be used as phased array transducers. 12x12 element matrix arrays which elements are also distributed according to the Sampling Theorem allow the electronic phase control for arbitrary space angles of ultrasonic pulse propagation but also migration for 3D imaging of flaws.

1.3.4.3. Synthetic Aperture Focusing Technique SAFT

SAFT has been applied for flaw evaluation since more than 30 years (Müller, 1988). Especially for heavy wall components ultrasonic inspection results with non-acceptable findings had to be analysed for repair decisions. Most often the length of indication was overcalled due to the beam spread of applied transducer sound fields at long distances and the 12db drop criteria for length measurement. For more accurate length measurements focusing transducers and synthetic focusing techniques have been introduced. Today SAFT application is part of the state-of-the-art of ultrasonic testing and controlled by guidelines (BS7910, 2005). Synthetic focusing data for flaw evaluation can be acquired by almost all automated ultrasonic systems with RF A-scan data storage capacity.

Whereas phased array measurements are controlled by adjustable phase relations SAFT measurements are controlled by position. When scanning a point (line) source transducer (element aperture in scanning direction less than half the wavelength) measuring RF A-scans the length of scan is forming the synthetic aperture (SA) and A-scan data can be used for reconstruction of reflectors. The dimension of SA determines the synthetic end of near-field according to standard computation rules as a function of frequency. All reconstructed reflectors inside of the synthetic near-field are imaged by synthetic focusing with limits practically close to the Raleigh criteria of half the wave-length. In good approximation the resolution Δx in scan direction of SAFT measurement is given by:

$$\Delta x = A_e/2 \qquad 1.3\text{-}26$$

where A_e is an aperture of Transducer and $\Delta x \geq \lambda/2$. Δx is independent of wavelength and distance within the synthetic near-field but limited by the Rayleigh criterion for data without measurement errors.

This rule shows the importance of small element aperture. For more detailed understanding the physics of synthetic aperture measurements we refer to literature written for synthetic aperture radar (SAR) applications (W.M. Brown, 2004).

The length of the effective synthetic aperture depends both on the divergence of the transducer element and the reflector properties. We may achieve the best possible resolution with the largest synthetic aperture when half-wavelength transducer elements are used for imaging of point reflectors for example side drilled holes. Both, the reflector and the transducer are sources resp. antennas that correspond to elementary Huygens waves.

When scanning the single element of SAFT measurement the synthetic aperture is growing until no reflected signal can be received by the element. For point reflectors the synthetic aperture is given by the beam divergence of the element. The above mentioned resolution contrast can be achieved only for point reflectors and point transducers. For extended planar reflectors, for example an extended lack of fusion with a slope of 45° or just the back-wall of the specimen in parallel alignment to the scanned surface, the synthetic aperture will collapse to one measurement position. The divergent beam of the ultrasonic transmitter pulse is folded with the directed reflection of the planar reflector. The synthetic near-field is limited in depth and the high resolution contrast is lost when the reflector is now located in the synthetic far-field.

Further, there are limitations given by the interaction of the acoustic pulse with real reflector geometries. For example, a side drilled hole generates reflector artefacts by surface waves propagating around the side drilled hole. We have to consider standard laws of wave interaction with material inhomogeneity.

The idea of SAFT reconstruction can be put across easily but quality of realization depends on some problems of measurement and data management that challenge for advanced codes. The problems are linked to the accuracy of position information of sampled wave field data, the characteristics of scanned transducer, the way the synthetic aperture is filled, and real-time imaging of reflector geometry.

Figure 17 illustrates the SAFT reconstruction of point reflectors. The scan results in RF echo dynamic curves here called data hyperbola for each reflector. Due to the beam divergence we can only assume the reflector position on a circle with radius corresponding to the time of flight. The circles for all transducer positions are superimposed with the result of reflector image in the spatial model.

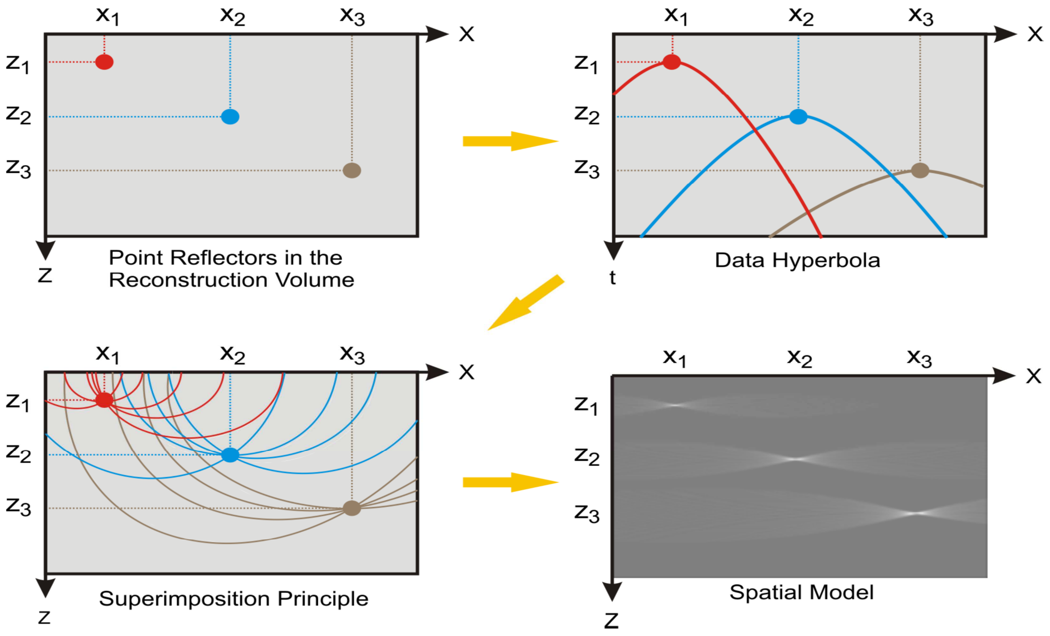

Figure 17: Principle of SAFT Measurement and Image Reconstruction (Bulavinov, 2005).

The illustrated SAFT reconstruction enables plausible understanding of some rules to be considered when SAFT is applied:

- Broad band pulses improve the resolution in space since the reconstruction radius range is narrowed.
- Larger beam divergence by smaller transducer aperture improves the lateral resolution by confining the superimposition by steep crossing angles of contributing time-of-flight radii.
- Since we measure RF A-scans, accurate position data are needed for constructive summation of reflector amplitudes. As a rule the relative position error should not exceed a quarter of a wave length.

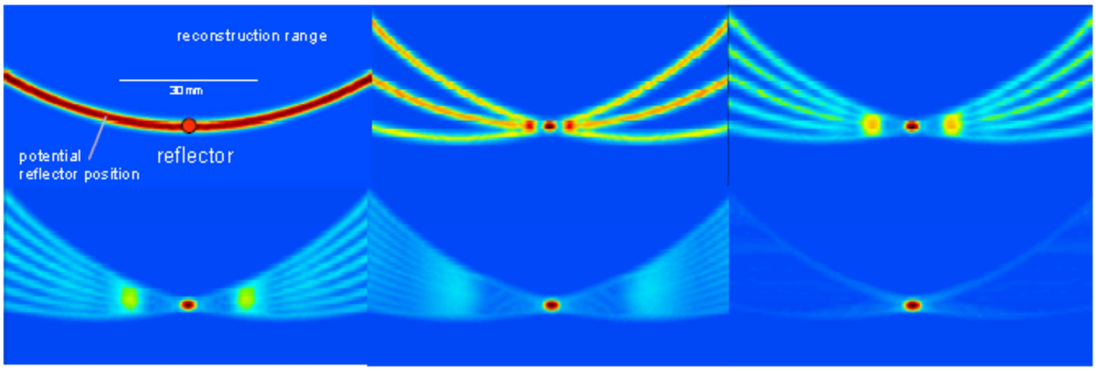

Figure 18: SAFT Reflector Reconstructions with Increasing Number of Probe Positions (Boehm, 2009).

Figure 18 from (Boehm, 2009) illustrates the special meaning of the number and density of measurement positions for the reflector reconstruction due to diffraction phenomena of wave physics. When we sample the wave data according to the Sampling Theorem we can avoid reconstruction artefacts by diffractions seen in Figure 18 for small number of measurement positions. In consequence we have to take one A-Scan at positions after scanning a distance of only half a wave length (corresponding to the skip distance of a phased array). Further, as it can be seen in Figure 18, the reconstructed reflector amplitude increases with the number of contributing measured amplitudes.

1.3.4.4. Migration Array Imaging Technique MAIT

Migration takes advantage of RF A-scans measured by an array. We may scan the array or reconstruct in one position. In conventional way of speaking the first one could be named as a compound scan, the second one a sector scan of an array. The difference is with the additional information provided by the pitch and catch measurements. In addition to the circles that describe the assumed reflector position we use also the elliptic reflector locus curve given by two elements of the array. Therefore, migration array data provide better information about details of geometric reflectors with higher reconstruction amplitudes and more effective noise averaging.

Figure 19 shows for illustration the elliptic reflector locus curve of a pitch and catch measurement.

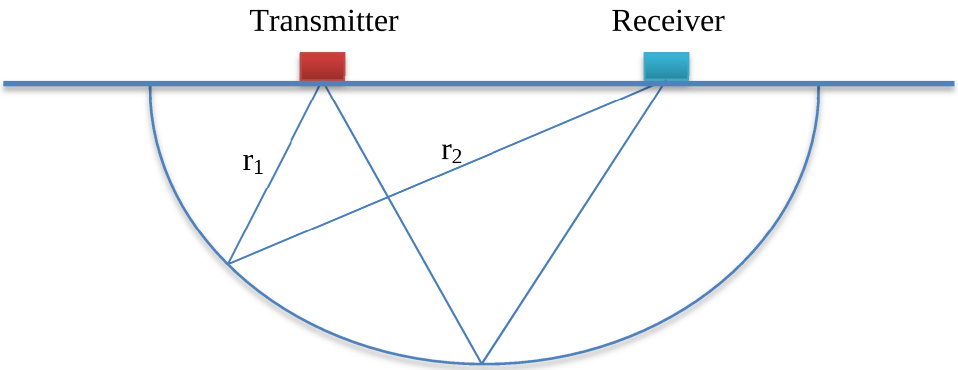

Figure 19: Elliptical Reflector Locus Curve for Array Elements Transmitter and Receiver.

The number N_{RLC} of independent reflector locus curves increases with the number n of array elements according to:

$$N_{RLC} = n(n+1)/2 \qquad 1.3\text{-}27$$

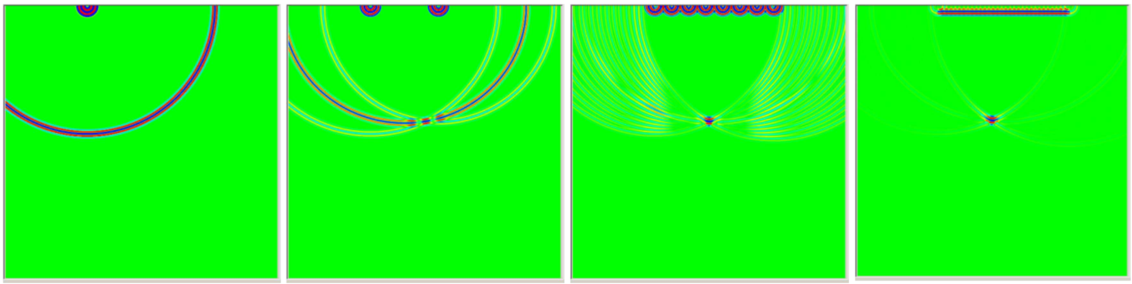

Figure 20: Effect of Increasing the Number of Array Elements (Zhantlessov, 2012).

An array with 16 elements will give already 136 reconstruction locus curves. Increasing the number n we get higher reflector amplitudes, resolution is improving and reconstruction artefacts are disappearing as it can be seen in Figure 20 above. The result of simulation presented in Figure 20 corresponds to Figure 18 for SAFT scans.

Most commonly, migration codes are based on Kirchhoff algorithm (Chang, 2001), (Bleistein, 2001). We have used the SynFoc© code, the first commercial software for NDT application developed by Lucidsoft[3].

Simple Kirchhoff migration algorithm is described with:

$$C(t) = \sum_i w_i B_i(t - t_i) \qquad 1.3\text{-}28$$

where $C(t)$ is the computed RF echo return, w_i is the weight assigned to returned signal $B_i(t)$ from element i and t_i is the time delay for element i. The surface-related coordinates are known by scanning. The wave-field W at a given point (x, y, z, t) is a summation of waves propagating from other points at earlier times. The summation process induces, especially when the aperture is limited and "i" is small.

Therefore, SynFoc© code extends the Kirchhoff approach by introducing an operator G which enforces goodness for fit on $C(t)$:

$$C(t) = G \sum_i w_i B_i(t - t_i) \qquad 1.3\text{-}29$$

G is function of distribution $w_i B_i(t - t_i)$ at time t. In perfectly focused condition all values of $w_i B_i(t - t_i)$ should be in phase and the amplitude should be same (Bolotina, 2012). By taking into account this information algorithmic noise caused by limited bandwidth of the ultrasonic signals can be eliminated or reduced. Various parameters are possible to enforce this fitness rule like deviation, entropy etc. SynFoc© used standard deviation as the enforcing parameter. This technique works well when coverage is good and inversion is well conditioned. Even though this condition theoretically leads to unity, in practice because of the measurement errors it requires a certain band (Bolotina, 2012).

---

[3] *www.lucidsoft.net*

Tighter conditions give better resolution in general, but can lead to suppression of weak indications - a consequence that enhances resolution if it is applied to detected images but with the unfavorable effect of a loss of contrast sensitivity and an increasing level of the side-lobes of the point-spread function (den Dekker, 1997). Since we have in mind the tracing of transducer position by analysis of backscattered noise we cannot afford tighter conditions. The further advantage of LucidSoft© is fast computing since the calculation of G is independent of neighborhood points and can be calculated in-line with the summation. It is well suited for parallel computing of migration images.

At the Fraunhofer Institute *Nondestructive Testing* IZFP[4] the Sampling Phased Array was developed (Bulavinov, 2005) with specialized features of the general migration approach. Nevertheless, the experimental results made with the multichannel prototype equipment prove also the basic features of migration we plan to apply for the "*Acoustic Mouse*"[5]. These features have been published and we take the opportunity for citation.

The first proof was the experimental verification of the equivalency of phase controlled (phased array operation mode) and position controlled (sampling mode) measurement. The tip indication of the fatigue crack in the test specimen shown in Figure 21 was used to compare the A-scans. The migration A-scan was synthesized from the migration sector image (Bulavinov, 2005).

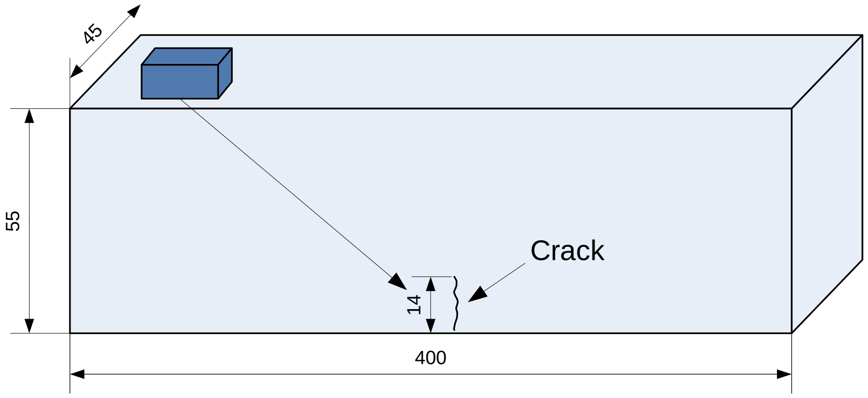

Figure 21: Steel Test Specimen with Fatigue Crack (all numbers in mm).

---

[4] *www.izfp.fraunhofer.de*

[5] *We are very grateful to Dr. A. Bulavinov for the opportunity to use his equipment for our experiments*

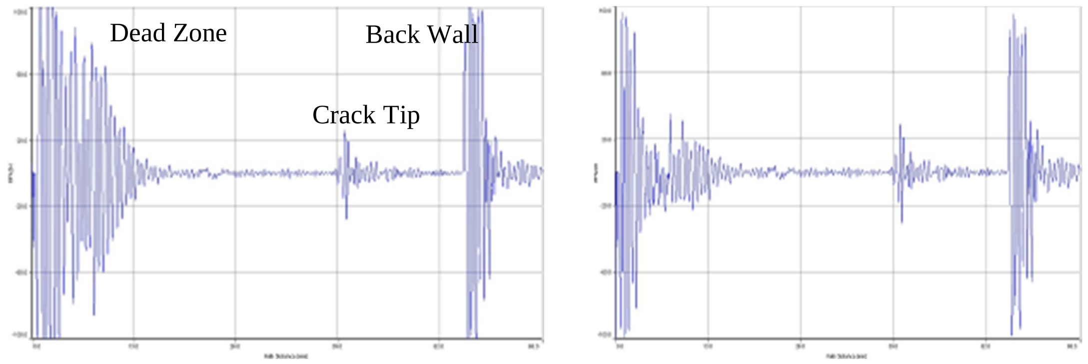

a) Conventional Phased Array

b) Sampling Mode

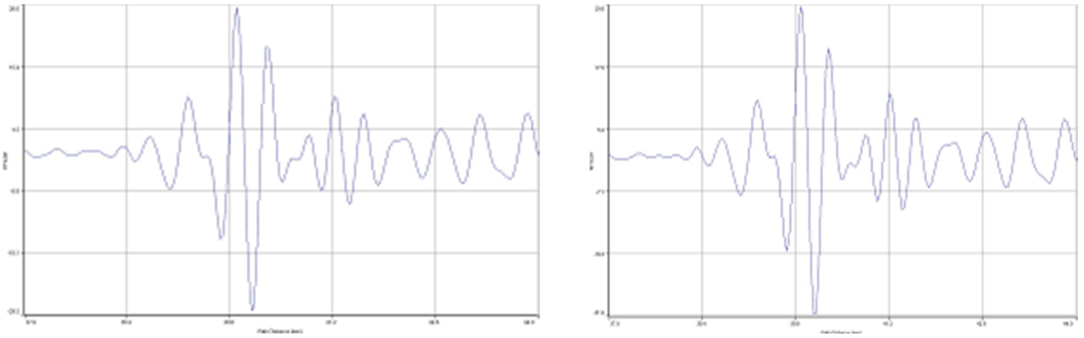

c) Crack Tip RF Signal of Phased

d) Crack Tip RF Signal of

Figure 22: Comparison of A-Scans.

The A-scans were taken for an incidence angle of 0°. The 5 MHz commercial Olympus linear array transducer with 64 elements had elements apertures of 0.5 x 12mm with the skip of 0.6 mm. Only the central group of 16 elements has been used due to the 16 channel design of the used sampling phased array prototype.

The back wall RF signal of Figure 22a was over amplified for a better visualization of the tip signal. The tip signals measured by Phased Array mode and Sampling mode are the very same ones that prove the equivalency of both operation modes for reflector A-scan imaging. We may state:

The proved equivalency allows the use of migration sector images in compliance with the current state-of-the-art of ultrasonic testing.

Further, the dead zone of the A-scan beneath the scanned surface is much smaller due to the impact of pitch and catch locus curves. Consequently, subsurface flaws can be detected much better by applying sampling operation mode.

The second feature of migration useful for the "*Acoustic Mouse*" development is the synthetic focusing throughout the near-field of the array aperture. This was discussed and demonstrated by experiment by (Bulavinov, 2005) and later publications (Bulavinov, 2007), (von Bernus, 2006), (Bolotina, 2012). For illustration of the image quality achieved by migration we discuss the results of the related first experiments (Bulavinov, 2005).

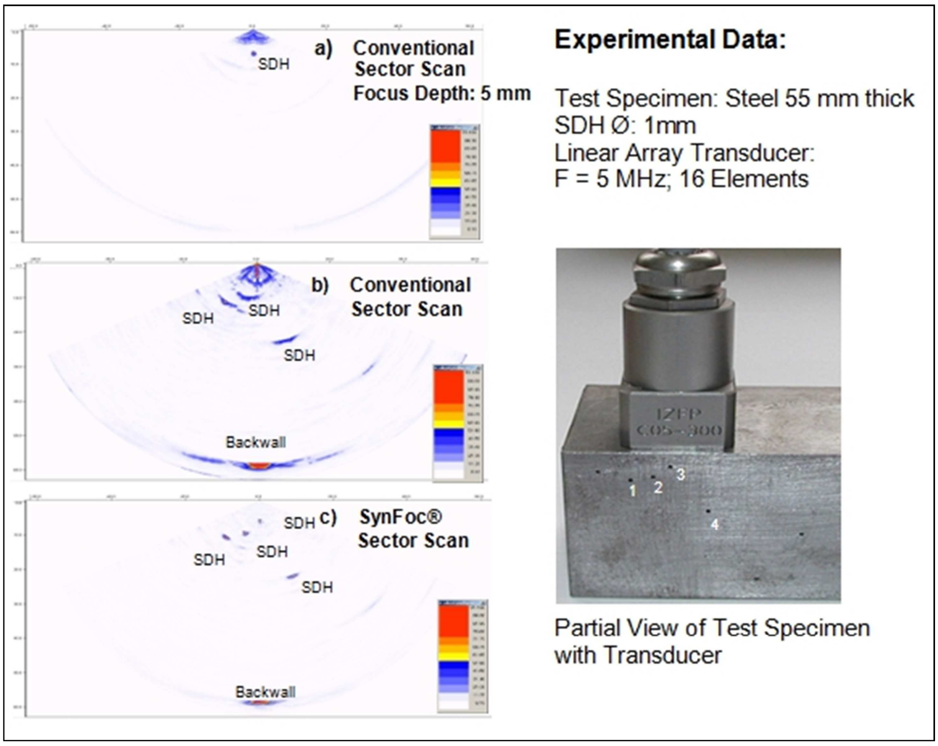

Figure 23: Comparison of Phased Array Sector Scans and Migration Sector Image.

Figure 24 shows the full test specimen used. The orange colored half circles indicate the near-field of the array. The linear array transducer (see Figure 23) of 5 MHz with 16 elements was built by Fraunhofer IZFP with element apertures comparable to the Olympus linear Array transducer.

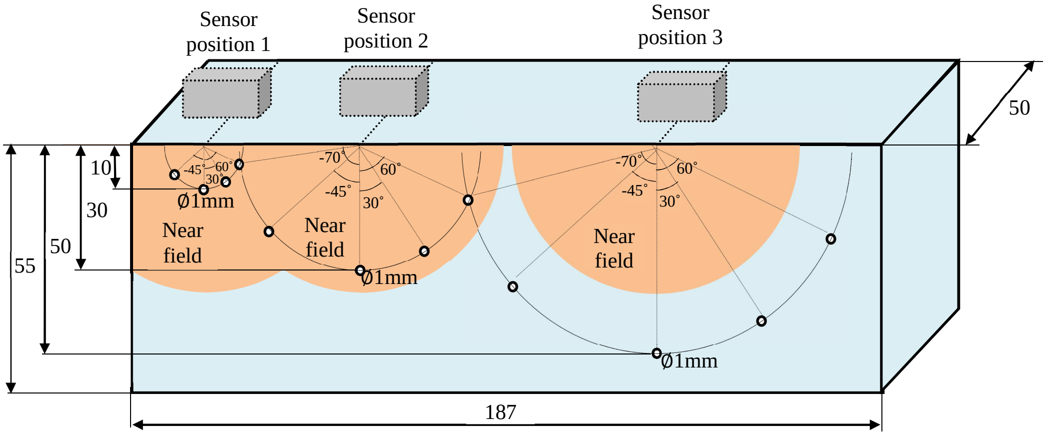

Figure 24: IZFP Steel Test Specimen with Side Drilled Holes SDH (all numbers in mm) (Bulavinov, 2005).

As it can be seen in Figure 23b the sector scan image measured by the non-focused phased array mode has a lateral resolution determined by the full array aperture not better than conventional plate transducers with same aperture would enable. The side drilled hole near the surface (SDH 3) cannot be detected by the same sector scan. However, we may focus the phased array on SDH 3. Now it is well imaged but even the back wall image disappears outside the focal zone (see Figure 23a). By migration (Figure 23c) we image all reflectors with high resolution almost homogeneous in the near-field of the array.

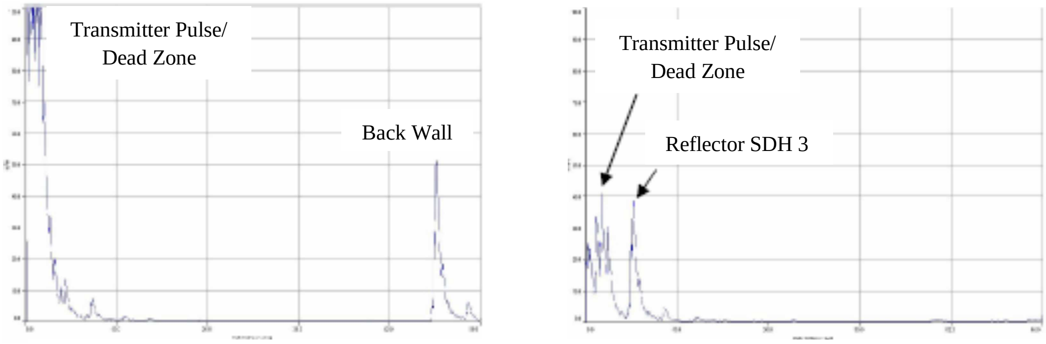

a) A-Scan Signal of Back Wall

b) A-Scan Signal of Near Surface SDH 3

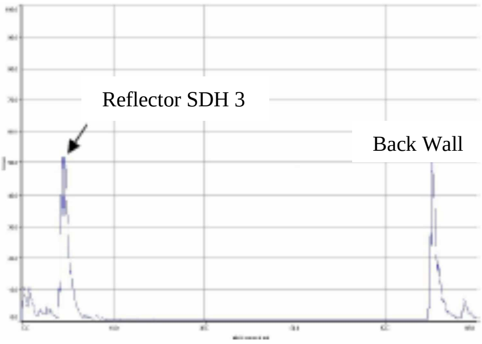

c) Migration A-Scan

Figure 25: Comparison of A-Scans.

The comparison of A-scans in Figure 25 underlines our second statement on the advantageous use of migration:

Migration Sector Scan Images enable the simultaneous and homogeneous imaging of all reflectors within the near-field of the array with high resolution

We intend to evaluate sector scans for position tracking of linear scans. Manual scanning is rather non-uniform and uneven and scanning speed may jump up to 1000 mm/sec. As a consequence we have to reconstruct sector scans at a repetition rate of 1000 per second for the scan index of 1mm. Phased Array sector scan imaging is by far too slow but even the sampling mode with all transducer elements in consecutive transmitter function creates time problems: Applying a 16 element linear array transducer we would have to transmit 16 times pulses in almost the same position. For scanning speeds up to 1000 mm/sec we would need a pulse repetition frequency of 16000 per second much too high for standard ultrasonic instruments with repetition frequencies less than 5 kHz. In consequence, we would have to increase the scan index up to 3mm significantly larger than half the wavelength of technical frequencies (for example: the longitudinal wavelength λ_l in steel for technical frequencies between 2 MHz and 5 MHz is in the range between 1.2mm and 3mm).

However, migration allows also reducing the number of array elements with transmitter function. This important feature enables fast scanning with real-time sector imaging. In Figure 26 we compare the A-scans with RF crack tip diffraction signals. Figure 26a shows the fully sampled migration A-scan from Figure 22d, Figure 26b the migration of the central column of the information matrix, respectively only the central element number 7 of 16 was used as transmitter.

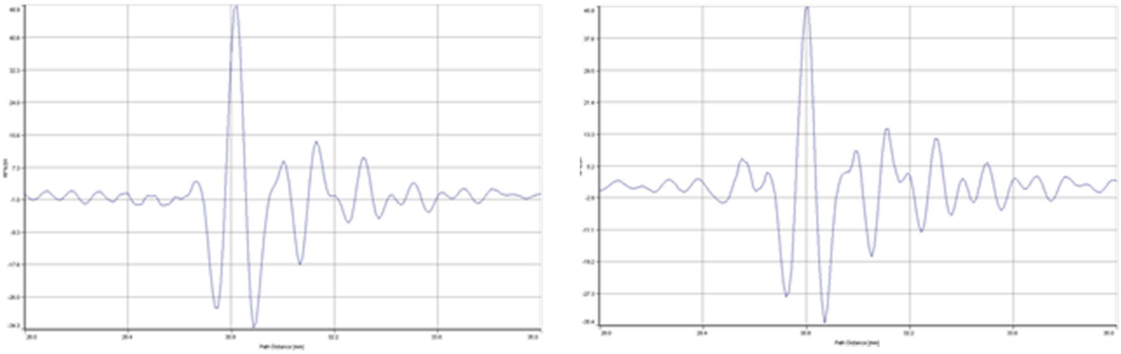

a) 16x16 Migration Image

b) 1x16 Migration Image

Figure 26: Comparison of A-scans with full and with sparse information (Bulavinov, 2005).

The difference is caused by the electronic noise that modifies the A-scan of the 1x16 migration. The noise results from the high amplification setting. It can be reduced by appropriate instrument design or filtering. Further, the interaction of transmitted sound pulses with geometric reflectors in one transducer position is different that can be compensated by compound scanning. Therefore, the third valuable feature for the "*Acoustic Mouse*" development is expressed by the statement:

Fast manual scanning with real-time sector scan imaging for position tracking can be achieved by sparse migration sector scan imaging.

1.3.5. Ultrasonic Imaging

Ultrasonic imaging terminology is part of standards and codes (ASME, 2010). Common images are A-scans, B-scans, C-scans. B-scan presents the data in the cross section parallel to the scanning direction; the C-scan is the top view on the inspected area. Additional features of imaging are various views with gates for selectable regions of interest like the end view through all the inspected volume against the scanning direction.

All these images are based on A-scans using the central ray trace of sound propagation. Therefore, the images are based on one-dimensional measurements. The A-scan presents the data in one dimension, the B- and C-scan in two dimensions. For complex geometries like nozzles the A-scans are presented in three dimensions. Therefore we have to distinguish between the dimensionality of measurement and data presentation.

The phased array sector scan represents the one-dimensional measurement because it consists of multiple A-scans taken along with the beam sweep. It can be visualized in 2D or 3D. The 3D image we get when we add the measured sector scans of parallel scans to one 3D image. The sector scan is a slice of the final image. The migration sector scan can be considered a 2D measurement with the same possibilities of imaging. However, the sector scan measurements detect reflectors only in the plane of the cross section defined by the beam sweep or the reconstruction plane.

We get the full contrast sensitivity only by a 3D measurement that is visualized in 3D but can be presented also by different selectable 2D views.

Figure 27 illustrates the different imaging and measurement principles (Reddy, 2011).

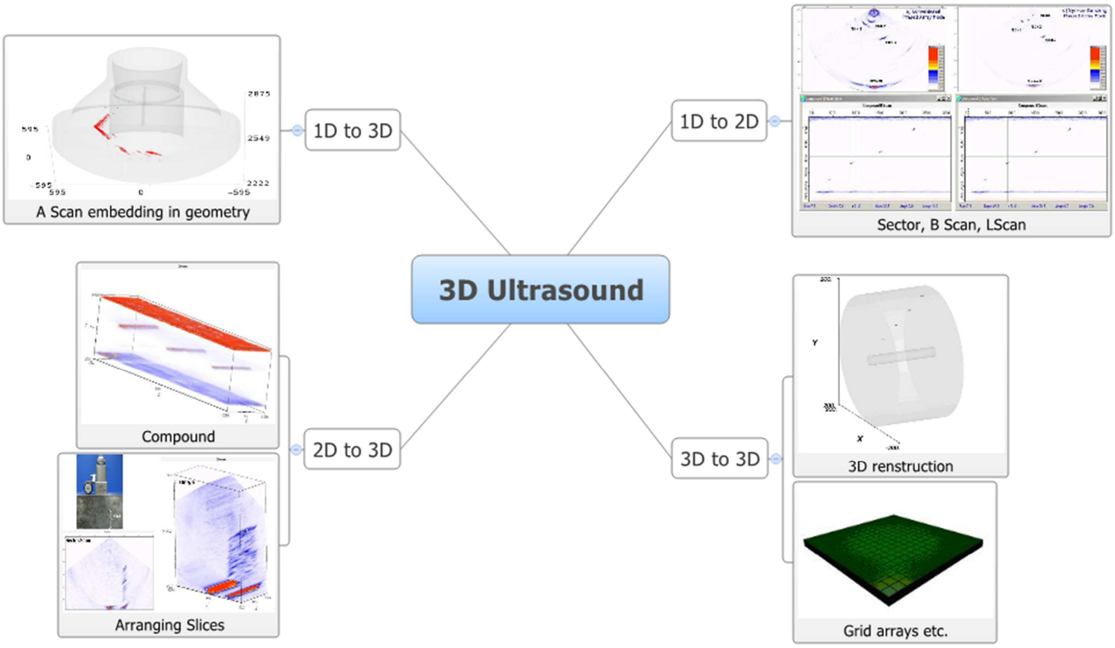

Figure 27: Ways of Ultrasonic Imaging.

We propose for the “*Acoustic Mouse*” 2D measurements (migration sector scan) but with 1D A-scan and 2D C-scan control during scanning in compliance with existing codes.

1.3.6. Elastodynamic Waves

The simulation of acoustic wave propagation in materials has become a common tool for the modeling of inspection problems. We have used in-house codes developed by Lucidsoft as part of their software portfolio (Reddy, 2011). Here we describe the basics of the applied elastodynamic code.

The solution of the wave equation for uniform and isotropic materials are two distinct wave modes, the longitudinal wave and the shear wave, propagating at a phase speed independent of frequency. We are aware of anisotropic and also dispersive structural materials but we limit our considerations to isotropic materials. The assumption of acoustic isotropy enables fast computations for simulations and migration. Efficient solver codes have been developed and can be found as free software.

The equations of motion for elastic media can be derived (Wikipedia, 2011) taking into account three tensor partial differential equations.

Hooke's law that governs the strain to stress relation,

$$\boldsymbol{\sigma} = \mathsf{C} : \epsilon \qquad 1.3\text{-}30$$

where σ is the Cauchy stress tensor, ϵ is the infinitesimal strain tensor, C is the fourth-order stiffness tensor, and $A : B = A_{ij}B_{ij}$ is the inner product of two second-order tensors (summation over repeated indices is implied).

The strain-displacement equations,

$$\epsilon = \frac{1}{2}[\boldsymbol{\nabla u} + (\boldsymbol{\nabla u})^T] \qquad 1.3\text{-}31$$

where u is the displacement vector, $\nabla(\bullet)$ represents the gradient operator.

The equation of motion (Newton's second law),

$$\boldsymbol{\nabla} \cdot \boldsymbol{\sigma} + \boldsymbol{F} = \rho\, \ddot{\boldsymbol{u}} \qquad 1.3\text{-}32$$

where F is the body force per unit volume, ρ is the mass density, $\nabla \cdot (\bullet)$ is the divergence operator, $\ddot{u}$ is a second derivative of the displacement vector with respect to time.

These equations are governing a linear elastic boundary value problem.

In Appendix A we derive the two expressions for the longitudinal and for the shear wave mode.

Chapter 2. The Evolution of Quantitative Ultrasonic Inspection

The need for and the objectives of Quantitative Ultrasonic Testing, here called QUT, have motivated us for the *"Acoustic Mouse"* development. The results of our development will be accepted and applied by industry when they contribute to the realization of QUT. We discuss some of the main requirements and trends towards QUT as they are specific for the *"Acoustic Mouse"* design. Further, we aim for the replacement of mechanical scanners required for QUT, and we should understand the achievements and the state-of-the-art of automated inspections with mechanical scanners. Therefore, we discuss the evolution of quantitative ultrasonic testing by its contribution to structural integrity, and the development and principles of automated scanning.

Quantitative Nondestructive Testing (QNDT) provides sufficient information about defect states in components that enables the assessment of further use under specific, given load conditions. QNDT must detect all material deficiencies that may cause failure within the designed life-time. Together with physical models for computational analysis, component design and manufacturing procedures, QNDT is applied to meet the requirements of reliability engineering of structures under load (Hellier, 2001), (Kröning, 2011).

Cracking is one of the most severe deficiencies for structural components under changing loads. The effect of cracking on structures can be assessed by Fracture Mechanic (FM) codes based on principles of Continuum Mechanics (Subra, 2003), (Stephens, 2001). Ultrasonic testing is considered to be the most adequate nondestructive testing technique for detection and evaluation of cracks in structures (Kiric, 2006), (Kurai, 2009), (Kiric, 2008).

By ultrasound even closed cracks under compressive residual stress can be detected, which are transparent for other nondestructive techniques like magnetic or X-ray testing. Another advantage of ultrasonic testing is the coverage of the full inspection volume: surface and volume defects of arbitrary orientation can be detected in contrast to pure surface inspection techniques.

In the following parts of the thesis we describe the evolution to modern ultrasonic QNDT to provide a basic understanding of the *"Acoustic Mouse"* as a tool for manual ultrasonic inspections with results that can be evaluated quantitatively.

2.1. Roots of Nondestructive Testing and Reliability Engineering

The industrial revolution of the IXX century is characterized by the beginning use of machines in all areas of industry. Machines run by steam power have revolutionized production of goods and traffic systems but have created also the demand for energy. However, the era of industrial revolution was also marked by many dramatic accidents caused by failures of pressurized steam vessels. Still in mind are the accidents on the "Sultana" on April 1865 when three of four boilers exploded (Salecker, 1996) or the accident in Hartford, Connecticut in 1854, when an almost new boiler exploded with tremendous force. The dramatic consequences of these and other accidents pushed the development of structural safety engineering including nondestructive testing methods. Safety engineering codes became mandatory with regulations according to the available state of the art. In 1864 the Boiler Inspection Act was passed in the State of Connecticut (Hellier, 2001). Nowadays, the American Society of Mechanical Engineers (ASME) Boiler and Pressure Vessel Code is the most applied code for pressurized components and systems. The *Dampfkesselverordnung* is one of the oldest regulations put into force in Germany at this time. The related mandatory codes and technical recommendations aim to minimizing the risk of component failure (Dampfkesselbestimmungen, 2004), (Weber, 1963).

At that time, the beginning of the *Mechanical Age*, when engines began to replace or to support human labour, the knowledge and technical background was rather limited for the development of non-destructive methods. Therefore the opportunity for an insight of structures was very exciting when W.C. Röntgen described X-rays first time in 1895 (Gherman, 1994), (Glasser, 1993). Röntgen was awarded the Noble Prize in Physics, 1901. Very soon after the detection X-rays were already used for the inspection of industrial components, and R. Seifert, an assistant to W.C. Röntgen founded his company around 1930, that has survived generations (Deutsch, 2000). Other techniques like magnetic leakage flux has been also developed, and the number of steam vessel explosions could be reduced dramatically (Chuse, 1993).

This achievement was not only due to the introduction of NDT regulations and the development of NDT techniques. At the same time, the material scientists and engineers, for example A. Wöhler (1819 -1914), have developed destructive testing techniques for the characterization of material properties fit for purpose and to assess the operational stability and the life time of safe component operation (Wöhler, 1855). Both, the assurance of material properties and the assurance of defect free components have become essential for the design, production and operation of structural components made of steel.

2.2. Ultrasonic Testing and Fracture Mechanics

When welding of steel joints was developed with the advantage of – at this time – lightweight construction of structures, cracks have posed the major risk of structural failure. X-ray techniques are not fit for use when cracks are closed or misaligned. At this time, in 1929, a new non-destructive testing method was developed in Leningrad by S.Y. Sokolov: the first ultrasonic system (Hellier, 2001). Sokolov was the first engineer who proposed ultrasonic waves for the detection of discontinuities in metals. For that reason he might be called the father of ultrasonic testing. Later he described piezoelectric transducers for transmitting and receiving ultrasound (Sokoloff, 1937).

A series of cargo ship accidents caused by poor structure quality prompted US scientists and engineers to develop mathematical codes for the probability of failure assessment of cracked structural components under vibrational load (Courant, 1943), (Razvan, 2009). Since that time, fracture mechanics has become an applied structural reliability tool that combines load, material properties and material defects with dominant role of cracking.

The reliability postulation of crack free structures has also pushed the development of NDT methods for crack detection. Surface cracks are of special meaning due to load accumulation at the surface and the consequent risk for crack growth until failure. Surface inspection techniques (Penetrant Testing PT, Magnetic Powder Testing MP, Eddy Current Testing EC) have been developed and have become mandatory for surface crack detection (Cartz, 1995), (E. Bray, 1989). The inspection demand for buried near surface cracks (or lack of fusions) or for cracks in non-accessible surfaces has pushed the development of ultrasonic equipment for crack inspections especially of welds (Papadakis, 1999). Ultrasonic and Eddy Current testing are scanning techniques and their application lead to manipulator supported automated inspection systems. In line with these improvements of available inspection technologies, detailed NDT standards and procedures have been written for industrial applications with increasing international cohesion and acceptance (Harold, 1992).

2.2.1. Acceptance Criteria for Ultrasonic Indications

Until today, there is no general quantitative ultrasonic testing method QUT with accurate information about the flaw to be used for FM evaluation. The information about the defect state must comprise probability of detection (PoD) of defects, their type (cracks, lacks of fusion, voids, slag inclusions and others), their position in the structure, and their size. For that reason, the sensitivity settings are very conservative. Moreover, any finding is processed by fracture mechanic procedures as crack-like with stress intensity factors corresponding to an infinite sharp crack edge.

Figure 28 shows for illustration the critical crack size in a primary circuit component of a German Nuclear Power Plant compared with the calibrated reflector size that controls the sensitivity of inspection. The critical crack size leading to fracture is a 1260 mm long crack with a depth of 84 % of the wall thickness. Any reflector with amplitudes equal or higher than the calibrated reference reflector, a 3mm deep and 10mm long notch must be detected, reported and evaluated.

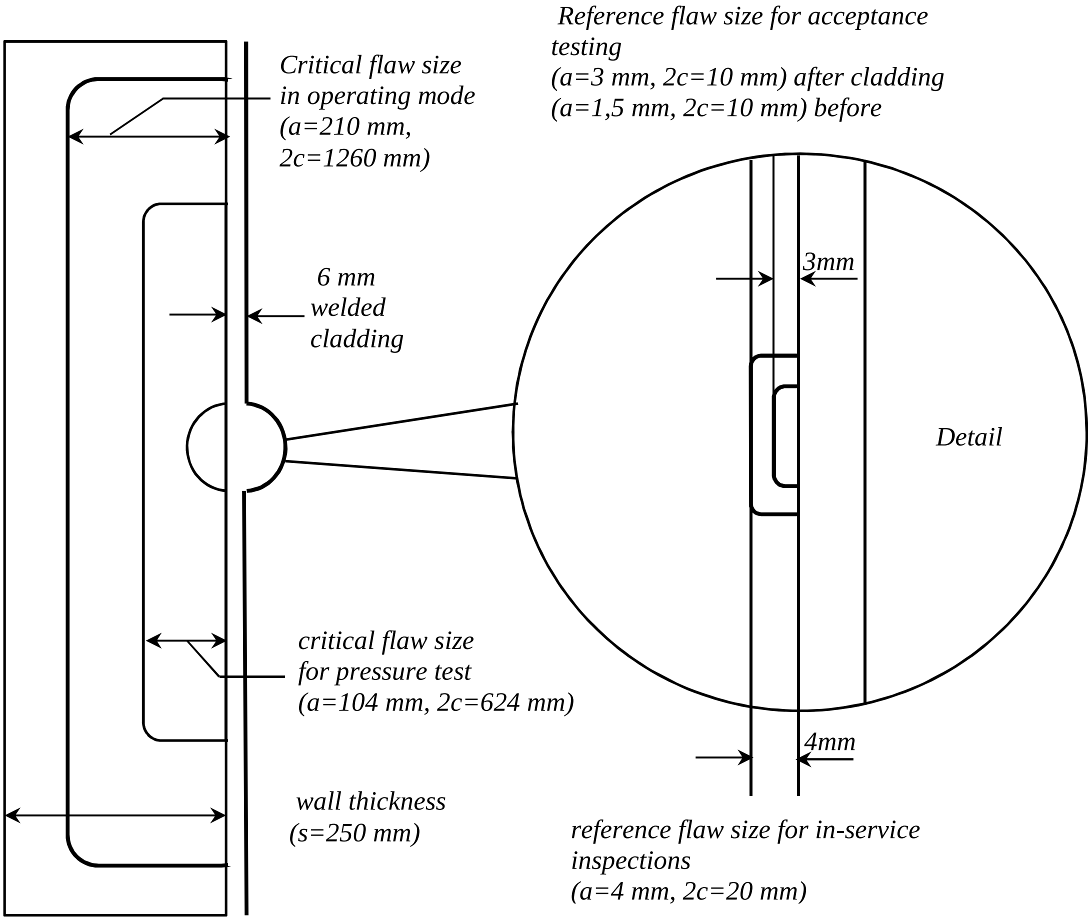

Figure 28: Relation of Critical Flaw Dimensions and Registration Sensitivity (Kröning, 2011).

As a rule for well-designed ultrasonic inspection systems, the sensitivity for flaw detection is much higher. The limit for flaw detection is defined by 6dB above the noise level. This large difference between critical and detectable flaw sizes has pushed production to high quality standards – a concept proven by the experienced extremely low number of failures. This experience based concept is part of the German basis safety (*Basissicherheit*) concept for nuclear engineering (Kußmaul, 1984), for example. However, the basis safety concept of mechanical engineering suffers high costs of production and is limited by light-weight engineering objectives.

2.2.2. Quantified Value of Ultrasonic Inspection

Basis Safety is a deterministic approach especially in respect to the defect state after NDT. A deterministic approach – using conservative, worst-case values for all input variables simultaneously – would often result in a safety strategy that could not be implemented in practice (Selby, 2011). A step beyond conventional, deterministic fracture mechanics is the probabilistic fracture mechanics (PFM) approach. It uses selected random variable inputs for situations that involve a significant degree of uncertainty. Important input data of concern are crack data - initiation rate, crack detection and sizing, crack growth rate – that describe the defect state, loads, and material properties. For each variable the statistics has to be analyzed and probability distributions have to be established.

The basic calculations of Probabilistic Fracture Mechanics (PFM) analysis comprise to steps. In step 1, a value for each input variable is selected randomly based on its probability distribution. The full data set is used for the calculation of the time to failure in step 2. The basic calculations are repeated applying “Monte Carlo” technique until the failure probability is of good statistics. PFM analysis yields a failure probability, rather than a specific calculation of crack size or lifetime.

The defect state for example is assumed by upper limit estimates of crack dimensions. When we know the probability of crack detection and the statistic distribution of remaining cracks after inspection we could assess the probability of failure by defect states more precisely. The advantage of this procedure would be a structural design less conservative. For that reason, mechanical engineers designing light weight structures, for example in aviation industry, have looked for advanced methods of reliability engineering. The replacement or extension of deterministic fracture mechanics by probabilistic codes is one of the major advancements in light weight engineering.

A failure assessment diagram (FAD) is used for the presentation of failure probabilities. The FAD accounts for the possibility of fracture and plastic collapse of ductile construction materials (Kuna, 2010). For the plastic collapse the J-Integral is applied by most of the practiced codes (Nuclear), (BS7910, 1997). The two possibilities are plotted on the axes of the FAD as K_r and S_r. S_r is a load ratio defined as a reference stress over the lower yield strength of 0.2% proof stress. The reference stress characterizes the possibility of plastic collapse. K_r is the fracture ratio and is defined as the applied stress intensity factor over the material toughness. A flaw is stable if the assessment point lies inside the FAD curve.

Figure 29 shows a typical failure assessment diagram, inside the FAD line the acceptable area, outside the area with critical flaw growth to failure.

Fracture mechanical assessment by fail/safe decision

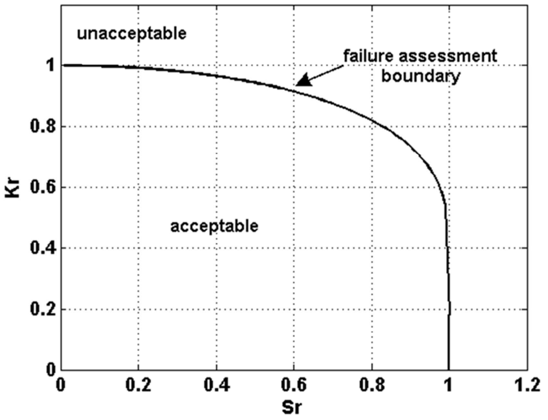

$$S_r = \frac{\sigma_{ref}}{\sigma_f}$$

Measure of ductile response of material to loading

$$K_r = \frac{K_1}{K_{1C}}$$

Measure of brittle response of material to loading

Figure 29: Failure Assessment Diagram FAD.

The recent development of probabilistic fracture mechanic codes may motivate design engineers to quantify the value of NDT for its contribution to structural reliability of technical systems (Cioclov, 1999), (Cioclov, 2005). By known probability of detection (PoD) we can assess the effect of NDT on the remaining risk of failure (Cioclov, 2000), (Bulavinov, 2007).

The failure assessment diagrams in Figure 30 show the effect on failure probability when defect state is known after inspection. The blue point operations are based on data gained by experiments for lightweight materials (Cioclov, 2005).

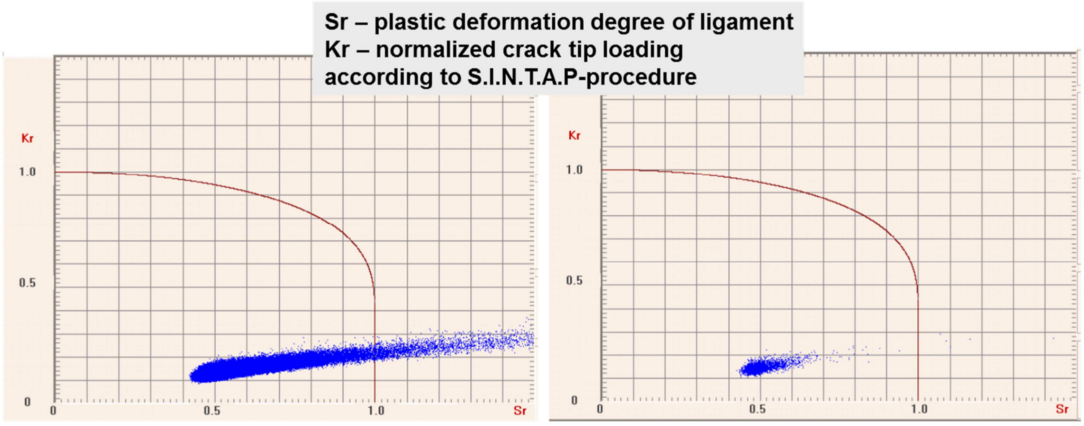

Sr – plastic deformation degree of ligament
Kr – normalized crack tip loading
according to S.I.N.T.A.P-procedure

FA-Diagram without (left) and with (right) consideration of NDT

Figure 30: The Quantitative Contribution of NDT to Structural Failure Assessment.

Each blue dot in the failure assessment diagram FAD represents the result of Monte-Carlo simulation by computing one set of the randomly distributed material, load and defect size data. On the right the limited possible maximum defect (crack) size by NDT reduces the risk of failure (blue dots outside of the FAD curve) significantly.

For illustration, the global failure risk $\boldsymbol{R}$ is a result of probability of failure *PoF* and consequences of failure *CoF* concurring according to:

$$\boldsymbol{R} = PoF * CoF \qquad 2.2\text{-}1$$

The risk reduction factor *RRF* achieved by NDT can be defined by:

$$RRF = \left(1 - \frac{PoF_{with\ NDT}}{PoF_{without\ NDT}}\right) * 100 \qquad 2.2\text{-}2$$

Here, the crack initiation rate and the crack growth rate are not taken into account (Gandossi, 2007).

In most cases the risk is reduced by one order of magnitude and more as the following numbers in Table 3 taken for a pipe system prove (Selby, 2011):

No inspection		**2 inspections (10yr, 30yr)**		**4 inspections (10yr, 20yr, 30yr, 40yr)**	
Prob. TWC	Prob. Fail.	Prob. TWC	Prob. Fail.	Prob. TWC	Prob. Fail.
3.22E-02	2.43E-02	2.35E-03	1.46E-03	6.14E-04	1.44E-04

Table 3: Effect of In-service Inspections on Probability of Through-Wall Crack (TWC) and Rupture – circumferential flaws only.

2.2.3. Probability of Detection

The assessment of risk of failure of loaded technical structures depends on the probability of detection (PoD) of defects (Rummel, 1998). The PoD is limited by the inspection physics, the shape and position of flaw in addition to human or performance errors. Consequently, NTD methods and procedures have to be assessed for PoD of defects (Achenbach, 2000) as one step towards quantitative NDT (QNDT). However, quantitative assessment of ultrasonic findings is still difficult because of the weak correlation between measured reflectivity and type and geometry of reflecting material discontinuity.

The reliability of detection by NDT was subject of a study by the European Community Plate Inspection Steering Committee PISC. The PISC-II study proved the probability of detection depending on flaw type and geometry. Volumetric flaws can be detected more reliable than planar cracks – a result of insufficient contrast sensitivity as defined above. The flaw evaluation depends strongly on their geometric details, their size and location (PISC II, 1986), (Silk, 1987). An early analysis of defect detection probability was also made by Haines 1983. He showed, as an example, that notch like flaws with a depth of 25mm and a length of 125mm can be detected in 200 mm thick pressurised water reactor vessel seam weld with a PoD of 99%. This number was obtained for 2 MHz 45° shear wave transducers by the corner effect and was justified for flaws tilt up to 20° (Silk, 1987).

These observations seem to go without saying. However, there is still the need for full understanding of probability of detection or probability of missing the most critical flaw. Further, the PoD is the approach to quantify the reliability of NDT. Therefore, a large amount of information is made available both as part of current research (Müller, 2006) but also already as industrial applications (Cobb, 2009), (Georgiou, 2006).

For the simplest “hit and miss” situation – we distinguish only between flaw detected and missed – the PoD is usually expressed as a function of flaw size. There are some basic assumptions applied for almost all inspection procedures: the probability of detection is growing with the flaw size, the procedure but also the applied method limits the detection of flaws with dimensions below a threshold, and for large flaw dimensions the PoD reaches saturation but below 100%. The PoD approach is limited or difficult to understand because of the impact of many random variables. In reality a PoD is a function of many other physical and operational parameters, such as, the material, the geometry, the flaw type, the NDT method, the testing conditions and the human impact (e.g. certification, education and experience of NDT personnel).

For calculating the PoD we have to find the functional relationship between sensor signal ***s*** and flaw size ***a*** such that the residuals are normally distributed with a constant variance as recommended by written procedure (MIL-HDBK-1823, 1999). Typically, this linear relationship is found in the log-log space:

$$\log_{10}(s) = c_1 \log_{10}(a) + c_0 + \vartheta \qquad 2.2\text{-}3$$

where ϑ – is a zero mean Gaussian random variable, and c_1 and c_0 are given by the linear fit of experimental data. The expected response $\log_{10}(s)$ is a random variable with mean equal to $\log_{10}(s) = c_1 \log_{10}(a) + c_0$ and standard deviation $\sigma(\vartheta)$. Introducing a detection threshold – the smallest flaw size a_{min} being found and reported, the probability of detection, $PoD(a)$, can be computed from the standard normal cumulative distribution function Φx as

$$PoD(a) = \Phi x = \frac{1}{\sqrt{2\pi}} \int_{-\infty}^{x} e^{-u^2/2}\, du \qquad 2.2\text{-}4$$

where $x = \left(c_1\, log_{10}(a) + c_0 - log_{10}(a_{min})\right)/\sigma_\vartheta$.

An example for establishing the PoD curve for a very specific inspection task and procedure is given by (Müller, 2006). In the course of welding procedure optimization and verification the PoD was developed given by Figure 31.

Automated inspection procedures enabled the reduction of human factors. Errors of human performance, the insufficient later control of inspection for example by third party experts do not allow the assessment of NDT reliability by PoD. Further, characterization and sizing of detected flaws by manual inspection is affected may be even more by the individual performance. Most important feature of automated systems is the position monitoring during scanning. The recorded position data enable the full reporting of inspection details including coverage of inspection volume, control of coupling (for UT) and so forth. Manual scanning as a quantitative ultrasonic inspection method needs position tracking of transducer.

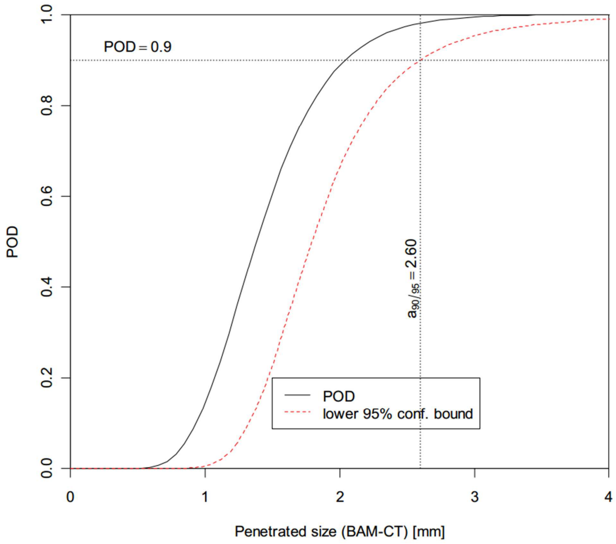

Figure 31: PoD of Specified Defect Types in Canister Welding for the High Energy Computed Tomography (Müller, 2006).

2.3. Manual and Automated Inspection Techniques

Ultrasonic testing is considered to be one of the most widely applied non-destructive testing techniques for flaw detection. Modern ultrasonic automated test techniques offer economical means for high speed, large or small scale testing of materials and structures. Manual scanning of ultrasonic transducers supported by the “*Acoustic Mouse*” should enable same or at least equivalent inspection results as automated scanning. For that reason we outline aspects of manual and automated ultrasonic inspection.

2.3.1. Manual Ultrasonic Inspection

Until today manual ultrasonic inspection is common practice in industry. The instrument used is portable, cost effective and can easily be operated by professional inspectors. As discussed above, the detected reflectors indicate only flaws with reference to generic calibrated reflector geometries. Until today, manual UT does not visualize flaw or reflector geometries. Nevertheless, there are some advantages of manual testing when reliable and professional inspectors are doing the inspection: the contrast sensitivity for the detection of planar reflectors is better due to transducer squivelling during scanning. Further, once the reflector is detected, the inspector takes time for careful coupling optimizing the insonification direction. Automated scanning asks for a certain scan index. The maximum echo amplitude might be received between the scan lines. Transducer squivelling can be realized by phased array transducers but is still not common state of applied automated procedures.

The problem with manual scanning is human performance and human error that cannot be controlled. The probability of detection of flaws depends strongly on the individual qualification and performance of inspector, and may vary uncontrollably ("Human Factor"). For that reason, safety relevant components are inspected by two or three independent parties (KTA 3201.4). The influence of human factor on probability of inspection was discussed carefully when PoD has become an issue, for example on the 4th European-American Workshop on Reliability of NDT in Berlin, 2009 (Bertovic).

Another problem is posed by systematic geometric indications. For example, only by special training inspectors will find cracks or lack of fusion near by the weld root with geometry as welded.

The assessment of critical findings is also depending on expert experience that is difficult to formalize. Figure 32 illustrates the manually performed evaluation of root indications found by the inspection of an austenitic pipe-to-elbow weld. This contour analysis took half an hour time when done in the early 80th (Kröning, 1982). Later metallographic analysis of inspection results proved a reliability of flaw evaluation for this procedure of up to 90% when pipe systems of concern have been replaced (Kröning, 2011).

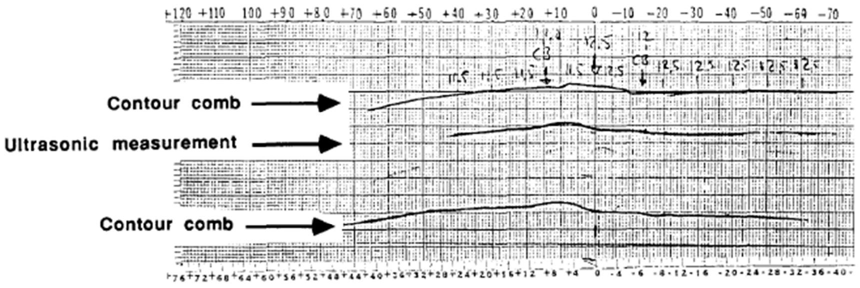

Example of reflector analyses in actual geometry of test specimen

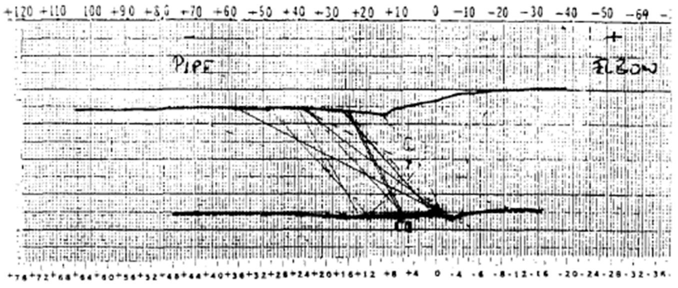

Figure 32: Manual Evaluation of Root Indications with Contour Analysis (Dalichow, 1986).

The need for expert knowledge for flaw evaluation has caused concerns that inspection system knowledge might have replaced the expert knowledge of manual scanning that combines in-situ signal assessment with the experience about real flaws and how to find them. These inspector skills are specifically addressed by all programs of professional education and qualification of UT-inspectors (SNT, 2001), (ANSI, 2001), (Personalzertifizierung, 2008).

2.3.2. Automated Ultrasonic Systems

We use the experience made in nuclear industry as an example for the development of automated systems. High speed scanning as required for inspection systems in-line of production cannot be achieved by manual scanning. Further, quantitative, risk based NDT is especially pushed by nuclear industry due to nuclear safety requirements (IAEA, 2006).

Nuclear Power Plant (NPP) construction and operation with challenging requirements for safety and reliability has promoted the development of automated inspection technologies and the quantitative understanding of the contribution of NDT to technical safety. In Germany, a special law (Atomgesetz, 1959), (BMU, 1999) was issued to guarantee technical safety of nuclear components and operations according to the latest state of Science and Technology. Inspections during manufacturing, pre-service and in-service inspections are mandatory and regulated by national codes and requirements, for example the American Boiler and Pressure Vessel Code ASME, Section XI (ASME, 2001).

In compliance with code requirements 25 % of the reactor coolant piping system welds must be inspected during outage as part of plant maintenance (Workman, 2007). The inspection procedure has to be validated including the qualification of personnel (ENIQ, 2007), the performance is controlled by third party independent authorities (KTA 3201.4), (KTA 3211.4).

The radiation exposure of personnel in nuclear power plants and the related ALARA principle (as low as reasonably achievable) require short inspection times with minimal radiation exposure (IRCP, 2007). Automated, remote controlled scanners and robotic devices for areas with hazardous radiation are applied when access is reasonably viable. In summary, the exposure of inspectors to radiation and also the remaining risk of "human failure" have challenged for automated inspections.

In Germany, pioneering experiments have been performed about 35 years ago that demonstrated the benefits of automated ultrasonic inspection in respect to reliability of inspection performance. Figure 33 visualizes results of a first professional commercial ultrasonic system mainly applied for pipe weld inspections (Kröning, 1986). The top views (C-scans) in the upper part of Figure 33 show indications later being evaluated as lack of fusion. The lower part of Figure 33 shows the signal amplitudes measured from both directions. The dotted line level corresponds to the calibrated registration sensitivity.

For illustration, Figure 34 shows a typical lack of fusion between the central and final runs of the welding to be found by ultrasonic testing (Rihar, 2000). The data have been taken by the P-SCAN-System (see also Figure 36), one of the earliest and later most successful automated pipe inspection systems (P-scan, 2011). The clearly visible root defect was not found by manual inspections because of interfering systematic root signals of similar position and time of flight. At this time, around 1985, also imaging principles have been developed and standardized as A-, B-, C-, and D-scans as illustrated in Figure 35.

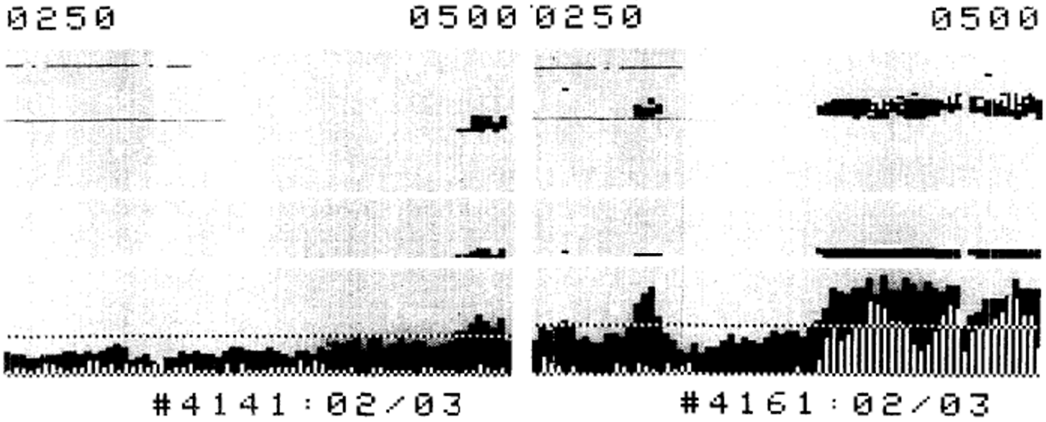

Figure 33: C-SCAN Presentation of Pipe Weld Defect (Kröning, 1986).

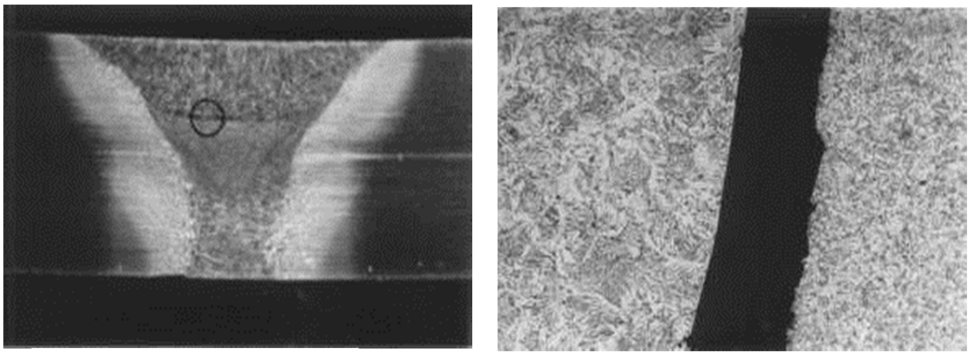

a) macrograph x3.5

b) micrograph: x100

Figure 34: Open Lack of Fusion between the Central and Final Runs (Rihar, 2000).

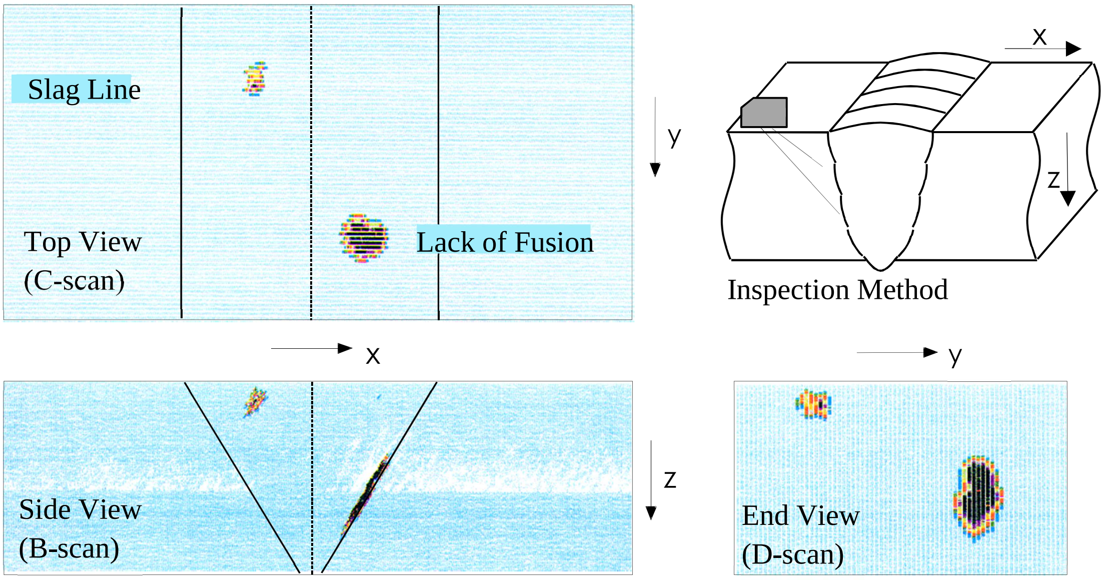

Figure 35: Imaging Basics of Pipe Weld Defects.

Figure 36 illustrates a more advanced P-scan pipe-to-pipe manipulator with ultrasonic imaging as applied for pipe weld inspections since 2001.

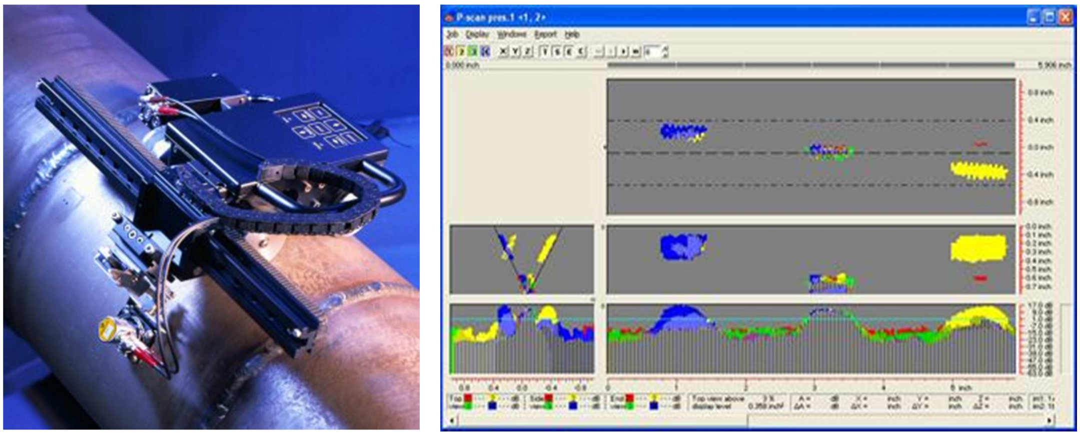

Figure 36: P-scan 4th Generation pipe scanner and data presentation[6].

Since automated inspection performance has become mandatory as part of reliability engineering or due to quality requirements of production the more complex and expensive part of inspection systems are the inspection manipulators. Very often, they are custom tailored fit for the specific inspection task. Figure 37 shows as an example the wheel set inspection station of freight wagons developed by Fraunhofer IZFP. The manipulator and the ultrasonic transducer system is designed for scanning both the wheel rim and the solid axle. The system comprises also the Eddy Current system for the rolling surface inspection (Rockstroh, 2005).

a) Inspection Station

b) Transducer System

Figure 37: Testing of Freight Wagon Wheel Sets (AURA Kaiserslautern).

The progress achieved in robotics has enabled a robot based scanner engineering platform (Li, 2011). Tailored robotic solutions are offered increasingly by robot

---

[6] Pictures belong to Force Technology Denmark, http://www.p-scan.com

suppliers for various areas including product inspection and testing. Due to the reprogrammable capability and other robotic features like high efficiency, repeatability and high endurance, the application of industrial robotic modules as scanner systems has become already a viable procedure in NDT system development. For example (Figure 38), Sackenreuther et al. have used two synchronized robots for their phased array inspection system replacing a standard mechanical scanner as illustrated above (Sackenreuther, 2009).

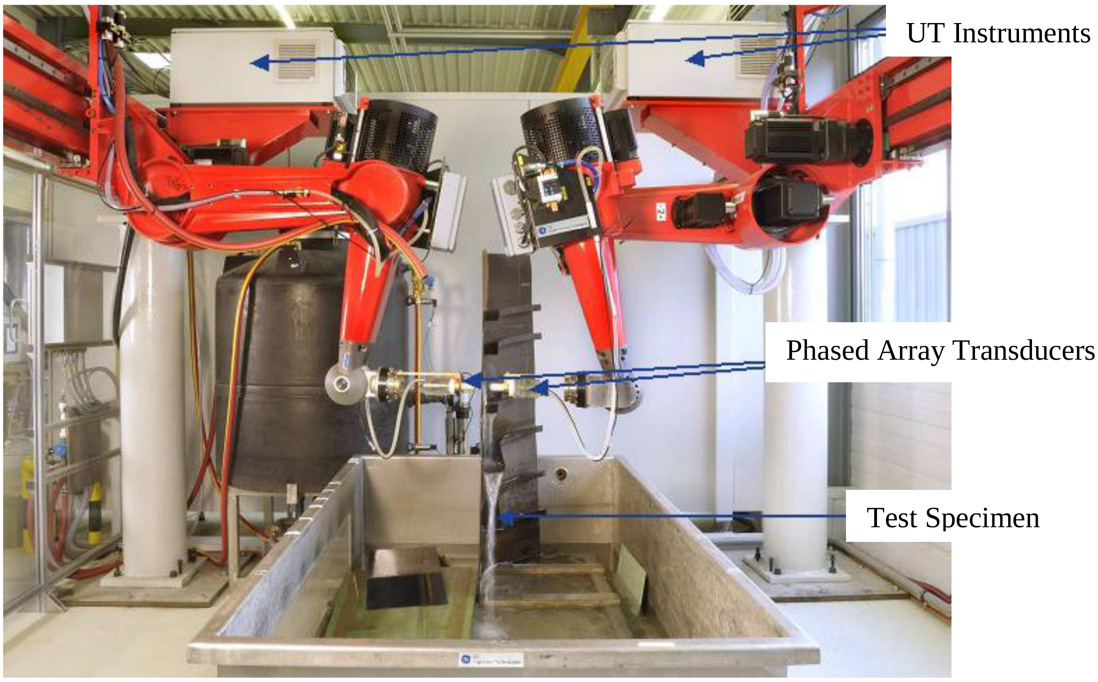

Figure 38: Synchronized Robot used for Ultrasonic NDT (Li, 2011).

2.3.3. Conclusions on Automated Scanning

Automated inspection systems provide reliable information on inspection performance (for example on system parameters and coupling) and inspected volume. Also, systematic indications can be discovered and assessed to a certain degree. However, the use of advanced manipulator systems is also limited due to several reasons:

a) The installation of manipulators is component specific, and requires time and relatively high financial investment.
b) Limited access and scanning conditions challenge for sophisticated solutions.
c) Long inspection times, mostly due to problems with the installation of the manipulator on the component.
d) Risk for noncompliance with existing standard procedures due to scanning limitations
e) Need for special training and qualification of personnel and for inspection procedure validation on representative test samples.

Pipe weld inspections may serve as an example. Today, safety relevant pipe systems are designed for better inspection conditions. Weld crowns and roots are ground flat and the elbow side of the weld is straight. Nevertheless, pipes of smaller diameter pose typical problems because of limited access or space for scanning and the need for transducer wedges which limit the full coverage of required incidence directions. A major problem of automated scanning is caused by the number of transducers necessary for all requested angles of incidence. Big sensor systems are difficult to be assembled, operated and controlled. Also, manual scanning enables transducer swivelling for reliable detection of misaligned planar flaws that cannot be achieved by reasonable automated scanning techniques. As a typical view on pipe systems in a power plant, Figure 39 (Mischerwelding, 2011) indicates the limited space for manipulator operations.

Figure 39: Typical Pipe System[7].

About 80% of pipe welds are pipe to elbow joints. The standard weld preparation usually does not allow the required inspection from elbow side by simple manipulator techniques as it can be seen in Figure 40. When scanning on the elbow side at the inner radius of elbow the angle of incidence is smaller, at the outside radius higher with effective changes of calibrated sensitivity. Further, the change from concave to convex surface limits the use of transducers with larger apertures. Last but not least, very often scanning on the elbow side cannot be achieved by reasonable manipulator systems at the inner radius of elbow.

When planning automated in-service inspections additional time and labour needed for cabling, scaffolding has to be considered. For comparison, a trained inspector may inspect a standard weld of such a pipe system within about 15 minutes. In case that

---

[7] The picture is taken from http://www.mischerwelding.sk/praceen.html

there are indications to be reported and to be evaluated by specific procedures, each analysis of an indication takes about other 15 minutes.

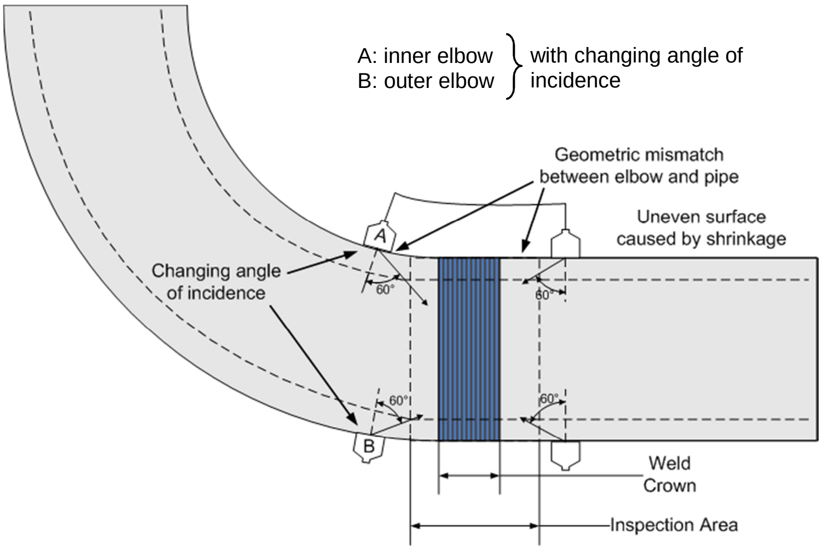

Figure 40: Geometry of Pipe-to-Elbow Joint.

The following conclusion can be drawn:

- Manual inspection is rather fast and does not suffer so much access or scanning limitations. Flaw detection is basically alright. Almost all flaw orientations can be found but recording depends on human performance which cannot be controlled and documented. Evaluation of systematic indications may pose severe problems because there is no visualization supporting signal analysis during scanning. As a result, critical defects can be called “geometry”.
- Automated inspection with standard ultrasonic multichannel systems at different levels of automation provides results with reported information on inspection performance. Systematic indications are visualized. The need for manipulation systems may limit the application to components with reasonable surface contours which are accessible. Practical aspects do not allow for transducer swivelling. Flaws which are misaligned to the sound beam propagation may be missed.

2.3.4. Manual Scanning supported by Transducer Position Tracking Systems

The complementing advantages of manual and automated scanning launched developments of transducer position tracking systems TPTS. The TPTS should allow manual scanning combined with the measurement of transducer position. Semi-automated techniques have been developed by different groups to offer and provide best practice services. Part of these developments has been directed to manual handling of the transducer with integrated position tracking. These systems support manual scanning by monitoring the sensor position using applicable triangulation techniques to compute and present ultrasonic data in the component's geometry (SwRI, 1978), (Spears). All developed systems with manual transducer handling have failed in practice even in view of the above mentioned advantages. Nevertheless, the practitioners have not lost the vision of manual inspection performance with reported and controllable performance and visualization of inspection results that might become even quantitative in the future. Here we outline two developments in support of the specification of the *"Acoustic Mouse"*.

The Search Unit Tracking and Recording System SUTARS was developed by the Southwest Research Institute, San Antonio, Texas, USA in the late 1970ies (SwRI, 1978). The main system feature is the transducer position measurement by airborne ultrasound. A longitudinal acoustic pulse is generated by electrostatic discharge. The transit time of the acoustic pulse is measured by microphones mounted on the UT transducer. Multiple discharge generators permit the exact determination of probe position and probe orientation in space by triangulation technique. Since the position data are available in real time, the SUTRAS system is suitable for manual scanning with merged position and ultrasonic testing data.

Other SUTARS features relate to the processing, archiving and display of the ultrasonic inspection data. Gates can be configured in the A-scan representation of the UT data, i.e. one can select a region of interest in a weld – the base metal, the HAZ (Heat Affected Zone) or the weld metal – for processing. In this way it is possible to differentiate direct reflections and multiple reflections. SUTARS can process echo amplitudes, transit times, probe positions and different angles of incidence. Results are imaged as B- and C-scans or can just be presented in a tabular format.

Today, advanced ultrasonic systems based on digital data processing at high speed are combined with the SUTARS position tracking system. Therefore, the SUTARS concept is viable today as well. However, especially the electro-magnetic noise generated by the sparks has prevented its practical use in industry.

At the Fraunhofer Institute Nondestructive Testing, IZFP, Saarbrücken (Gebhardt, 1996) the feasibility of an inertial system for transducer position tracking was investigated. Just like in this study the task was to obtain accurate position data in real time and match these with the UT inspection data.

A fixed reference point is required when starting scanning. The movement of the UT transducer is tracked by the inertial system that consists of an accelerometer with three independent axes and of three gyroscopes. The track or position of the transducer can be determined by double integration of the acceleration vector a. The differential equation describes this relationship.

$$a(t) = \frac{d^2}{dt^2} r(t) \qquad 2.3\text{-}5$$

The acceleration a is measured and with the knowledge of a reference point, the position of the transducer r can be calculated exactly. What has to be considered is the fact that position errors accumulate. If the error of the inertial system is relatively large, this problem can be overcome by returning to the reference location and resetting the system.

The advantage of this approach compared with automated mechanical scanning is that the probe can be moved freely and almost arbitrary geometries can be tested. It is also possible to mark scanned areas on the test object and areas that still have to be inspected.

This pioneering research and development asks for highly accurate micro-accelerometers and electronic devices that have not been available at this time. With differential gyroscopes the transducer rotation could be calculated with an error of less than 1° during an inspection interval of four minutes. The error of transducer positioning for translational movement was much larger and could lead to a wrong positioning of up to 500 mm within 100 seconds of measuring time. This worst case finding challenged the inspector for unreasonably frequent resetting along a reference grid to overcome this limitation. Recent advances in sensor technology and computational power may make the inertial position measurement concept feasible for field applications in future.

The experience available until today allows the conclusions that we may substitute manual scanning for mechanical scanning when:

- No additional technique is needed for position measurement. As a result of this requirement the ultrasonic signals themselves have to be evaluated for position measurement;
- The relative accuracy of position measurement is in the range of half the wavelength to process data for advanced 2D or later 3D image reconstruction;
- After transducer lift-off, its position can be reproduced with an accuracy of approximately half the wavelength;
- Manual scanning provides reliable data for all required incidence angles and all required scanning directions;
- Redundant data can be evaluated for the correct maximum amplitude A-scan image at optimized coupling conditions.

These experienced based conclusions have initiated a new approach – the “*Acoustic Mouse*” (Bernus, 2006).

Chapter 3. Objectives of Research and Development

The general objective of research and development is the replacement of mechanical scanners by manual scanning of one probe with same or even improved quantitatively assessable inspection results (defect imaging) and viable control of the full coverage of inspection volume.

3.1. Concept of "*Acoustic Mouse*"

The "*Acoustic Mouse*" concept is designed analogue to the advanced "Optical Mouse" developed by Microsoft 1999 (Wikipedia, 2011), (Microsoft, 1999).

The ultrasonic signals carry information about the sensor position provided by acoustic scattering sources in the material under inspection. In principal all three types of scattering, the 'geometric scattering' by material discontinuities larger than the wavelength, the 'Rayleigh scattering' by dimensions less than half the wavelength and 'stochastic scattering' by dimensions in between as outlined above may be considered for fingerprinting the transducer position. The first type represents reflections from the component geometry (e.g. back-wall echo) or from extended flaws; the second one is forming the acoustic noise scattered by grain boundaries and small reflectors. The stochastic scattering by intermediate size material discontinuities may mark the position of the transducer the best due to the in general well localized point source characteristics of scattering.

The relative accuracy should be better than half the wavelength to process the measured data by migration or synthetic aperture codes for high resolution ultrasonic imaging. Analogue to the manipulator supported scanning the position information must be processed in real time during scanning. Last but not least, the use of the "*Acoustic Mouse*" must allow easy going manual inspection that includes control of full coverage of the inspection volume specified by the inspection procedure including the occasional lift-off of the transducer, the identification of already inspected areas and the processing of redundant data when the transducer is in the same scan position.

3.2. Basic Specification of *“Acoustic Mouse”*

In the following, some basic features of the *“Acoustic Mouse”* are defined for practical reasons:

a) Transducer design

Most favourable is the use of one transducer for position tracking and inspection. Because of the desired quantitative flaw imaging with a minimum number of probes the *“Acoustic Mouse”* should be designed as an array transducer without any special features (additional cabling etc.).

b) Signal processing

The data must be processed in real-time according to common manual scanning speed up to 500 mm/sec.

c) Positioning index

The distance between two computed transducer positions should be about half the wavelength for the formation of synthetic apertures. Larger distances may become feasible when image reconstruction techniques are applied that don’t require the validity of the ‘Sampling theorem’ (Bolotina, 2012).

d) Positioning accuracy

The absolute accuracy of computed sensor position should be in the range of some millimetres. The absolute accuracy determines the error of flaw location. The relative accuracy should be better than half the wavelength for two reasons: the ultrasonic measurement data (A-Scans) will be processed as RF-data with the assumption of correct phase information related to neighboured measurement positions, secondly, the inspector has to lift the probe sometimes, for example to apply fresh coupling liquid. The *“Acoustic Mouse”* has to find the old position through comparison of newly measured data with existing data.

e) Redundant data management

During manual scanning the sensor will take data from same measurement position repeatedly. Thus, redundant data set have to be processed. Since coupling may vary in the range of about 6dB, the ‘best’ data set must be identified. In case of noisy measurement data averaging techniques might be applied.

f) Coverage of inspection volume

The inspector has to be informed about the continuing coverage of the scanned surface including appropriate control of coupling.

3.3. Scientific and Technical Problems

We limit our research and development to the processing of acoustic noise data. The acoustic noise structure is a fingerprint of the transducer position as outlined above. However, the information is covered by measurement errors caused by changing coupling conditions. Further on, grain boundary noise is highly sensitive to smallest transducer position changes due to interference phenomena. Both problems have to be investigated and solved when acoustic noise is taken into consideration for transducer position tracking.

We propose the processing of 2D sector scans measured by linear arrays and reconstructed by migration. Migration sector scans consist of redundant data that can be computed for assumed correct element position or time-of-flight data. As a thesis we assume that stochastic filtering enables both the reduction of coupling induced measurement errors and of grain boundary noise. The processed sector scans are reconstructed ultrasonic images that can be assessed by appropriate processing of image sequences taken during scanning; we propose the “optical flow” image processing technique applied in robotics that enables the assessment of image changes for position tracking.

The 2D sector scan analysis can be generalized for 3D cone scans measured by matrix arrays when matrix arrays will be available. We assume that 3D cone-scan measurement data are less sensitive to grain boundary noise due to focussing in 3D.

Chapter 4. The “Optical Flow”

Optical flow is the pattern of apparent motion of object details in a visual scene caused by the relative motion between an observer and the scene. If a time series of images is taken from objects moving in the scene, or the observer himself is moving, we can track the object or observer motion. Sequences of ordered images allow the estimation of motion as either instantaneous image velocities or discrete image displacements.

Major applications of optical flow are motion estimation and video compression. Optical flow enables to estimate the three-dimensional structure of the scene, the 3D motion of objects or the observer in 3D relative to the scene. Therefore, optical flow was used by robotics researchers for object detection and tracking, movement detection, and robot navigation (Aires, 2008). One application very similar to the objectives of *“Acoustic Mouse”* development is the optical mouse. The first commercially successful optical computer mice were the Microsoft IntelliMouse, introduced in 1999 using technology developed by Hewlett-Packard (Microsoft, 1999). Optical mice use optical sensors to image surface texture in materials such as mouse pads. The surface is lit at a grazing angle by a light emitting diode. Images of the surface are captured in continuous succession with a repetition rate of about one kHz. They are compared with each other to determine how far the mouse has moved.

Motion estimation is the process of determining motion vectors that describe the transformation from one 2D image to another. However, sequences of ultrasonic images carry object motion in three dimensions relative to the transducer. As long as we reconstruct 2D images (for example sector scans) taken by linear arrays we have to overcome an ill-posed problem as the real-world relative reflector motion is in three dimensions. There are two strategies for transducer tracking by optical flow evaluation: we solve the ill-posed problem by numerical approximation supported by global image assumptions or we measure 3D images by matrix arrays.

The objective of this thesis is the general prove of the usability of optical flow in acoustic image sequences for transducer tracking. We limit our experiments to 2D measurements on test specimens with reference reflectors that are quasi two dimensional such as side drill holes. However, the acoustic noise and revealed point like reflectors are still three dimensional and may question some of our conclusions.

4.1. Sensor Position Tracking

Based on general optical flow algorithms we developed a novel sensor tracking algorithm. In the following, we describe and explain the variation calculus theory that is used for the tracking algorithm. First of all, we describe the physical background, estimate the data needed for the computations and how it can be acquired. After that, we describe the optical flow and how variation methods become handy to calculate the optical flow field of two images. In this part, therewith, we introduce a formulation of the problem and we show the numerical scheme of the introduced formulation. We finish with the calibrating parameters and their meaning for the estimation process.

4.1.1. Image Object Motion

The sensor position tracking algorithm developed uses a 2D representation of the Sampling Phased Array (SPA) ultrasonic data (Bulavinov, 2005). The SPA instrument and its use were described in chapter 1.3.4. The data obtained with a linear phased array transducer are processed and imaged as a sector-scan.

As discussed already, sector scan reconstruction by migration offers advantages: the sector image comprises all angles of incidence within the sector angle, the reflector image is well focused throughout the synthetic near-field of the array, the sector scans can be reconstructed at repetition frequencies of kHz for real-time measurements when only one element is transmitting the ultrasonic pulse, and we may process and filter the data in real-time for better visualization (resolution and contrast improvement) and for minimizing the errors produced by coupling instabilities. The algorithm developed for transducer tracking is based on sector scan image analysis and processing. In simple words, the algorithm analyses the image of the sector-scan and estimates the direction (left or right) and distance from the transducer’s previous position. Most suitable image objects are real reflectors presented with high resolution of reflector details. However, in general we may not rely on the existence of geometric reflectors. The sector images may offer only acoustic noise caused by grain boundaries or by Rayleigh scattering of small material inhomogeneity.

Acoustic noise can be seen from any transducer position. It forms a material fingerprint but very sensitive to slightest transducer position or coupling changes. Since sector scans are two-dimensional but acoustic noise signals are generated by the three-dimensional ultrasonic pulse, we have to face instabilities common for ill-posed problems. In addition, grain boundary reflections are contributing to the acoustic noise rather chaotic and stochastic due to the variety of reflection conditions including multiple scattering and interference phenomena. Therefore, processed image objects used for transducer tracking are most likely locally confined sources of Rayleigh scattering as outlined in chapter 1.3.2. We assume that the same scattering source will appear again on the subsequent sector scan after the transducer movement. From the transducer point of view the material structure is moving in either direction. This means, that this motion can be technically tracked.

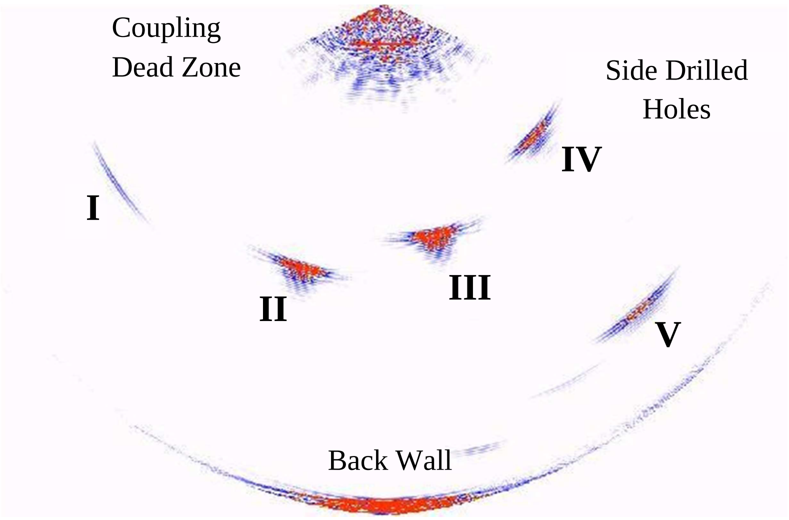

Figure 41: Sector Scan with Geometric Reflectors, Artifacts, Coupling and Acoustic Noise.

The sector scan in Figure 41 is taken on the test specimen described in Figure 24. The transducer was in the position indicated by black color in Figure 24. The data are not filtered and resolution is poor because the side drilled holes of Ø1 mm are outside the near-field of the array aperture. We intended a non-optimized reflector imaging to study the effects of reflector and reconstruction artifacts seen in Figure 41. Reflector artifacts are multiple indications behind the reflector, reconstruction artifacts can be best seen by the circle shaped presentation of the back wall. The technical details of sampling phased array measurement and the experimental details are described in chapter 1.3.4 – “Ultrasonic Arrays”.

Comparing two sector scan images (see Figure 42) at slightly different transducer positions, we can extract information about the distance in logical units (pixels, for example) between corresponding similarities that belong to both images. The distance can be transformed in metric units by using a resolution parameter called often “pixel size” parameter. The resolution parameter should be calibrated when the sector-scan is reconstructed and should not be changed. The slight transducer displacement is already visible.

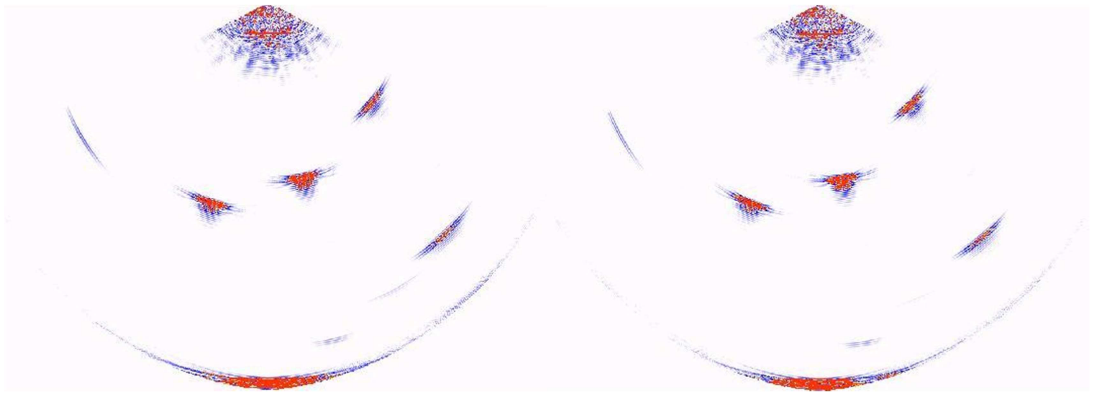

Figure 42: Comparison of two Sector Scans at Slightly Different Transducer Positions.

4.1.2. Image Windows

Certainly, we have not to process the full sector scan. The dead zone, for example, consists of signals caused by coupling conditions and its structure does not depend primarily on the local material properties. The back wall image does not depend on the transducer position, too.

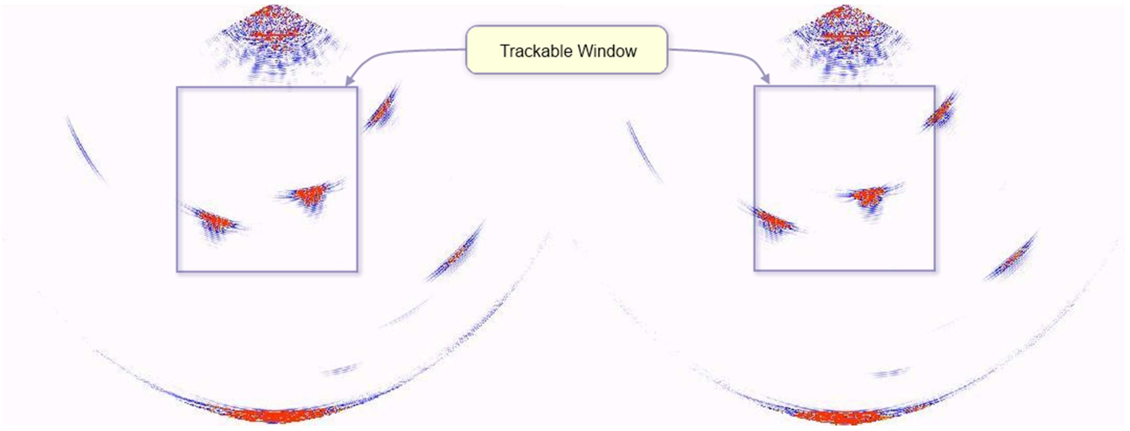

Figure 43: Image Window for Transducer Tracking.

Further, when we go for real-time processing, the processed image part should be as small as possible but large enough for robust transducer tracking. Therefore, we have to identify criteria for areas of interest as shown in Figure 43. The area of interest can vary in size depending on the inspection problem, synthetic near-field, frequency, resolution, and so forth.

4.2. Offset Vector Field

Moving the transducer leads to motion of reconstructed objects in the sector scan. The object motion must be quantitatively assessed for transducer tracking. One representation of the object motion is the offset vector field. Each element of the vector field indicates the size and direction of its offset. Optical flow estimation enables the calculation of the offset field from two consecutive sector-scans.

4.2.1. Optical Flow

Without a doubt, the measurement of Optical flow measurement is a fundamental problem in image sequence processing. Optical flow estimation has been investigated by computer vision researchers for a long time (Horn, 1981), (Healy, 2002), (Galvin B., 1998), (Bruhn, 2003) and is still an ongoing topic of research. The task of optical flow estimation is the computation of the optical flow field for a given pair of images. This task is still challenging, especially when the images contain severe occlusions and non-rigid motion. Once computed, the optical flow field can be used for a wide variety of tasks ranging from passive scene interpretation to autonomous, active exploration. These tasks usually require the computed 2D motion field to be accurate and dense, providing a close approximation to the real 2D motion field. Current techniques allow relative errors in the optical flow computation results to be less than 10% (Weickert, 2003).

The idea of optical flow calculation for 2D images is to maintain the brightness constancy assumption. This assumption relates the image gradient ∇I to the components u and v of the local optical field. Since this is an ill-posed problem, some additional constraints are required to regularize the motion field during the flow estimation.

One particular case of optical flow estimation is the determination of the shift between views of the two given images called disparity estimation (Alvarez, 2002). When the sensor position is always horizontal and the motion is only in one direction the task of calculating the correct shift for the whole image range is a one-dimensional problem. Nevertheless, the estimation task is related to the calculation of the 2D displacement field, which is the optical flow vector field.

Many methods for determining optical flow have been proposed so far and they continue to appear. One of the known techniques is the Phase Correlation Technique (De Castro, 1987). It uses a Fourier transformation to obtain a spectrum correlation for the final determination of the image shift. This technique is rather simple and very effective in particular cases. However, it determines the shift properly only for the whole image, not regions or pixels. Further, this technique does not allow finding the proper shift if two images are similar in shape but differ in content like in our case with two sector scans. In case of low resolution input sub-pixel precision can be another problem of this method.

Block- or region-based methods define velocity as the shift that yields the best fit between image regions at different times. Finding the best match amounts to maximizing a similarity measure (over the shift), such as the normalized cross-correlation, or to minimizing a distance measure, such as the sum-of-squared difference (Fuh, 1989).

Energy-based techniques (Barron, 1994) involve estimating the image energy through a Fourier filter that reveals the velocity in the frequency domain. Phase-based techniques are similar, exploiting the behavior of band-pass filters to induce the velocity of image regions.

Discrete optimization methods are techniques of optical flow estimation that quantize the search space, and the subsequent image matching is addressed through label assignment at every pixel in such a way that the corresponding deformation minimizes the distance between the source and the target image. The optimal solution is often recovered through “min-cut max-flow” algorithms (Glocker, 2008), (Healy, 2002).

Differential techniques compute velocity from spatio-temporal derivatives of image intensity or filtered versions of the image (Bruhn, 2003), (Alvarez, 2002), (Weickert, 2003). Variational methods in general are differential methods of estimating optical flow, based on partial derivatives of image signals. Most of them are modifications of the Horn-Schunk (Horn, 1981) method with different smoothness and data terms. Our approach is related to these methods that is why we describe the variational methods further.

Optical flow field of image sequences can be represented by means of a vector grid (see Figure 44, a-d) or it can be color-coded using a color-wheel (see Figure 44, e-f). As one can see, color-coding gives better understanding of the whole image motion, while a vector grid representation is suitable for a rough result analysis.

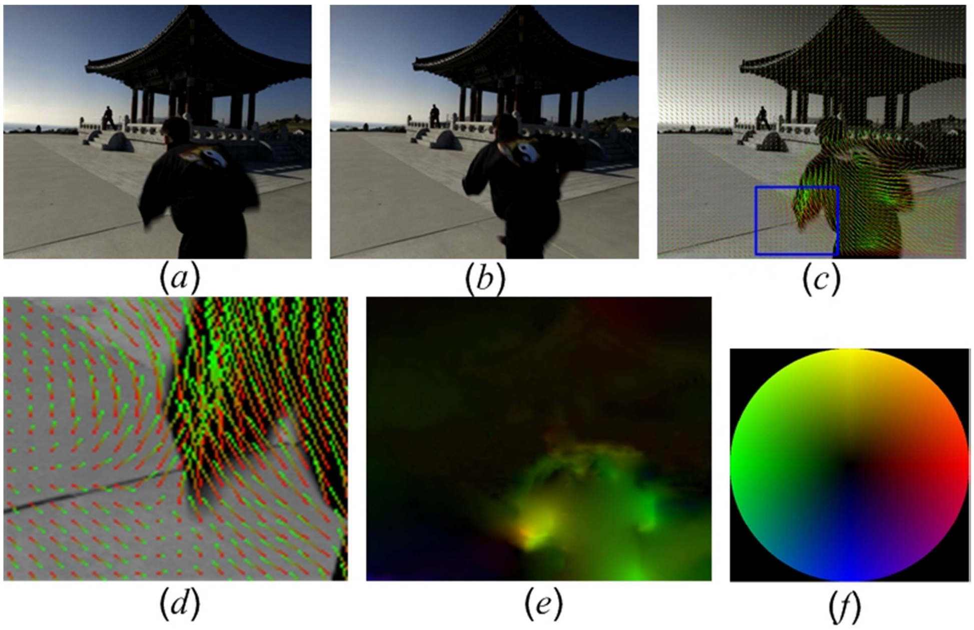

Figure 44: Optical Flow Example (Xiao, 2006).

The image sequence is given by Figure 44a and b, the optical flow vector field by c. Figure 44d is the enlarged detail of figure c. The color-coded vector field is shown in Figure 44e. The color-wheel (Figure 44f) codes the direction and the distance.

In our case, the transducer motion is only one-dimensional, in horizontal direction. Therefore, the optical flow field is of one-dimensional nature, too. This particular case can be considered as a disparity estimation problem corresponding to the problem of finding a structure or shading from an image pair with known camera calibration and placement parameters.

4.2.2. Disparity Estimation

Estimating the disparity field between a pair of images taken by two equidistant cameras is a common task in image processing and computer vision. Disparity estimation simplifies the determination of the depth map of stereo images.

When estimating disparity, the correspondence between two images is sought, i.e. the corresponding pixel from the second image is sought for each pixel from the first image in such a way that the corresponding pixels are the projections of the same 3D point (Alvarez, 2002), (Kosov, 2009). Camera calibration setup should be known. In this case we can calculate a depth map from the disparity field. Usually, one uses a stereo setup that places the corresponding pixels in one line in each of the input images. Thus, this problem becomes a 1D problem – a particular case of the general optical flow calculus.

The difference between disparity-driven and depth-driven method calculations is the following: for reconstructing a 3D depth map, one can directly calculate an optical flow between several view images and find a depth map as a solution to the optical flow functional that brings the implicitness in sub-functions under the functional. The Euler-Lagrange equations for the disparity-driven methods have a linear form while they are nonlinear for the depth-driven method. Therefore, we cannot choose a linear numerical scheme for solving them (Kosov, 2007).

The disparity estimation task is widely used in robotics, stereo reconstruction and other tasks. Using two cameras, calibrated as a stereo pair, one can calculate a 3D depth during the motion to obtain a reconstruction of the whole volume (Slesareva, 2005), (Zimmer, 2008), (Kosov, 2007).

In case of ultrasonic transducer tracking (or *“Acoustic Mouse”*) we reconstruct two consecutive sector-scans. The calculated disparity field between these two sector-scans is actually a map of distances. The map can be simplified to a scalar value because we don’t have to reconstruct the depth information to assess the transducer motion of a line scan. Figure 45 demonstrates an example of disparity calculation. The calculated image is a distance map for each pixel. Regions, which have color different from the background, are moving in left direction. Since the motion is only one-dimensional the color coding is also represented in 1D. The color mapping indicates how the disparity map should be read.

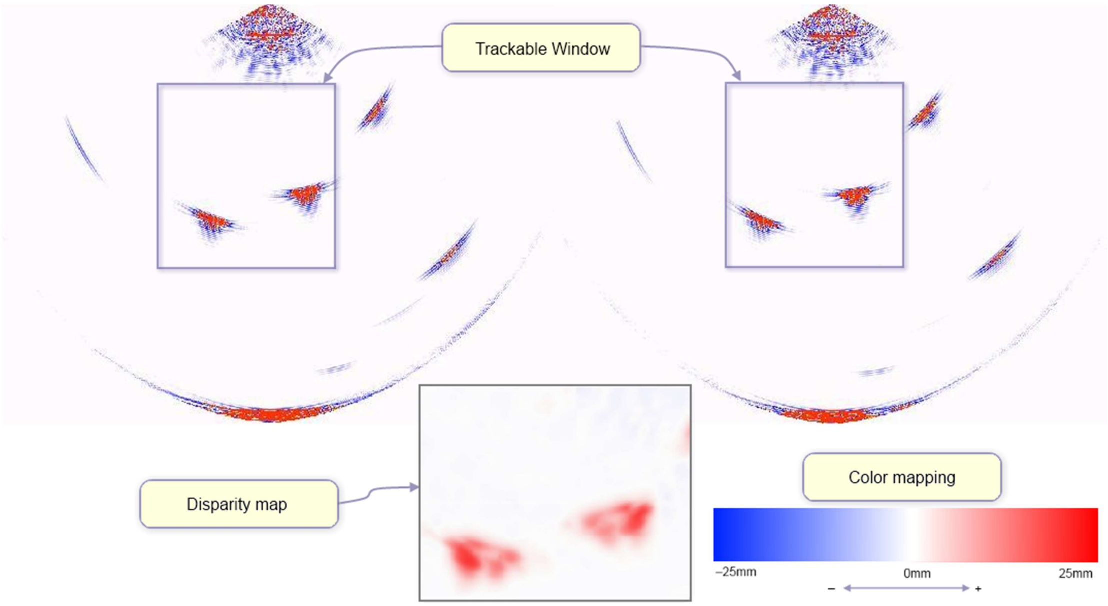

Figure 45: Disparity estimation example for a pair of sector-scans.

4.2.3. Disparity Estimation Methods Overview

One of the interesting applications of disparity estimation is stereo reconstruction – one of the most challenging tasks in Image Analysis and Computer Vision. Disparity, estimated on a stereo-image pair, can be turned into a depth map by a set of simple formulations. Based on this depth map, one can perform a stereo reconstruction that recreate a visible part of 3D world and render it from different point of views and different textures. Another application of disparity estimation extends the ability of multi-view camera setups. This approach encodes a video sequence by means of calculating the disparity between each view pair. The disparity contains less information than the original image, and enables decreasing significantly the size of video data.

There are four groups of different disparity algorithms:

1. Feature-based approaches. This method searches for matching characteristic image points, i.e. corners (Grimson, 1985).
2. Area-based approaches. This approach matches image pixels, if there exists a certain similarity in the regions around these pixels (Scharstein, 2002).
3. Phase-based approaches. These algorithms use phase information in the Fourier domain (Froehlinghaus, 1996).
4. Energy-based approaches. The disparity is found by minimizing the energy functional that penalizes deviations of the data and smoothness assumptions (Kolmogorov, 2002), (Mansouri, 1998), (Scharstein, 2002), (Slesareva, 2005).

The last class can be further grouped into probabilistic and variational approaches. The first type (Kolmogorov, 2002), (Scharstein, 2002) finds the disparity between two images by modeling the images and the disparity as a Markov random field. These models bring a minimization of discrete energy, which is usually done by graph cuts, belief propagation or dynamic programming algorithms. These methods are very fast and successful as they usually impose strict smoothness assumptions, modeling a piecewise constant disparity. However, for the case of smoothly varying depth, these methods lead to severe drawbacks if the assumption of the piecewise constant disparity is violated (Li, 2006). Moreover, since the probabilistic methods work only with integer values, they suffer from their discrete nature.

The second type of energy-based methods – the variational approaches do not suffer from these restrictions. These methods compute the disparity by minimizing the continuous energy functional. This can be done by a gradient descent method that requires computing the steady-state of the partial differential equation of diffusion-reaction type. First successful application of the variational method for the optical flow computation was described by Horn and Schunk (Horn, 1981). Since that time different applications of variational methods in area disparity estimation and optical flow computation have been developed (Alvarez, 2002), (Zimmer, 2008), (Slesareva, 2005). In this work, we limit ourselves to rectified images (sector-scans are de-facto rectified) with displacement only in one direction. The disparity in this case becomes a scalar value.

4.3. Variational Methods

Variational methods, or calculus of variations, are a field of mathematics that deals with extreme value functional, opposite to ordinary calculus that deals with functions[8]. Such a functional is formulated as integral involving an unknown function or/and its derivatives as arguments. Most interesting for us are the functions that bring the functional to its extreme value: minimum or maximum.

Nowadays, variational methods are widely used in computer vision and image processing. There are depth perception and depth-reconstruction, 3D reconstruction, stereo vision and many other fields, where variational methods become handy. Since they are global methods, they operate on the entire image domain. They recover the disparity map that we are searching for as a minimizer of the appropriate functional that we will call *energy functional*.

Let’s assume an image pair $I_1(u,v), I_2(u,v)$, where (u,v) denotes the point coordinates on the image. Disparity map for such an image pair can be calculated as a solution $z(u,v)$ to the functional of the form:

$$E\big(z(u,v)\big) = \iint_{\Omega} F\left(I_1(u,v), I_2(u,v), z(u,v), \frac{\partial z(u,v)}{\partial u}, \frac{\partial z(u,v)}{\partial v}\right) du\, dv \qquad 4.3\text{-}1$$

This equation can be rewritten in a more general form:

$$E\big(z(u,v)\big) = \iint_{\Omega} F\left(u, v, z(u,v), \frac{\partial z(u,v)}{\partial u}, \frac{\partial z(u,v)}{\partial v}\right) du\, dv \qquad 4.3\text{-}2$$

The integration domain Ω is the entire image domain and the unknown function $z(u,v)$ has the same dimension as the input set of images. We rewrite the partial derivatives of the solution function $z(u,v)$ in a shorter notation for simplicity:

$$z_u \coloneqq \frac{\partial z(u,v)}{\partial u} \qquad 4.3\text{-}3$$

$$z_v \coloneqq \frac{\partial z(u,v)}{\partial v} \qquad 4.3\text{-}4$$

---

[8] *Definition based on materials from http://en.wikipedia.org/wiki/Variational_methods*

The functional $E\big(z(u,v)\big)$ has two terms, the *data term* and the *smoothness term*. These two terms influence the process of finding a solution in a different way. The data term provides information about the depth (or transducer shift in our case), and the smoothness term distributes this information. In some image regions the data term does not yield useful information. In this case the smoothness term gives these regions information calculated from neighboring regions. Such an approach guaranties that the resulting depth map will be dense.

$$E\big(z(u,v)\big) = \iint_{\Omega} DataTerm(u,v,z) + SmoothnessTerm(z_u, z_v)\, du\, dv \qquad 4.3\text{-}5$$

4.3.1. Pre-smoothing Step

In order to eliminate the influence of noise and other image errors and to prepare discreet image data more suitable for derivative calculation via difference schemes, we apply a smooth filter on the input images. By smoothing, the results of data processing are more relevant and robust and of improved quality (Condell, 2006), (Kosov, 2007). Instead of the original images $I_i(u,v)$, we will use a pre-smoothed version according to formulation 4.3-6. For smoothing we choose a Gaussian low-pass filter, e.g. by convolving the original image with the Gaussian kernel K_σ where σ is a standard deviation parameter.

$$I_i^\sigma = K_\sigma * I_i \qquad 4.3\text{-}6$$

The influence of the parameter σ will be considered in the following part of this chapter. It greatly affects the result of depth-map computation. Since we don't go to operate original image data but their pre-smoothed version, we omit the sign σ. However, writing I_i we assume a pre-smoothed image I_i^σ. Also, without loss of generality, we write I_1, I_2 assuming I_i, I_{i+1} correspondingly.

4.3.2. Minimization Functional

The minimization of the functional 4.3-2 should result in solution $z(u,v)$ that is the depth-map we are looking for. This solution brings the whole functional $E(z(u,v))$ to its minimum. If the functional 4.3-2 is *strictly convex*[9], then the solution $z(u,v)$ is unique.

In order to minimize the functional 4.3-2 one has to solve the corresponding *Euler-Lagrange equation* 4.3-7.

---

[9] *A strictly convex function is a real-valued function f defined on an interval, where for two points x and y in its domain and any t in [0; 1] the following holds: f(tx+(1-t)y) ≤ tf(x)+(1-t)f(y).*

$$F_z - \frac{d}{du}F_{z_u} - \frac{d}{dv}F_{z_v} = 0 \qquad 4.3\text{-}7$$

This variation calculus formulation was developed by *Leonard Euler* (April 15, 1707 – September 18, 1783) and *Joseph-Lois Lagrange* (January 25, 1736 – April 10, 1813) in the 1750s. Therefore, this equation is called in honor of these mathematicians Euler-Lagrange equation.

Function $z(u,v)$ should satisfy the Euler-Lagrange equation 4.3-7 and maximize the functional 4.3-2. F is a given function with continuous first order partial derivatives. Therefore, the Euler-Lagrange equation 4.3-7 is a partial derivative equation and the unknown function $z(u,v)$ must satisfy it.

In order to minimize functional 4.3-2, we have to solve the Euler-Lagrange equation with homogeneous Neumann boundary conditions by means of discrete numerical schemes. The Euler-Lagrange equation is discretized with a finite-differences scheme to be able to work on discrete images. At the end we obtain linear or nonlinear system of equations, which have to be solved by one of the numerical iterative schemes known.

As it was described previously, the energy functional consists of two parts: the data term and the smoothness term (formulation 4.3-5). Since both terms have their own meaning, we will introduce them separately in the following part of this chapter.

4.3.3. Data Term

The data term is a number of combined assumptions that certain features of the input images do not change but stay constant (or almost unchanged) from image to image. It informs about the depth-field and holds the constancy assumptions that are used. Usually a *brightness constancy assumption* is used as a general assumption.

The brightness constancy assumption (or gray value constancy assumption) expects that all corresponding scene objects (or sector scan features in case of ultrasound images) of two images are of same color. Looking at a 3D scene taken from different points of view (see Figure 46) we can observe, that objects near to the cameras are shifted more than objects, which are far from the cameras. Estimating the shift of each pixel for such an image pair will allow us to calculate distances to those objects (and their pixels). Besides, same objects on both views have almost the same shape, size and color. Figure 46 demonstrates that any object keeps its color on each view and how the shift changes for differently located objects. Thus we assume that the gray value of the pixel does not change by shifting an object or a camera and formulate this assumption as equation 4.3-8.

$$I_1(u_1, v_1) = I_2(u_2, v_2) \qquad 4.3\text{-}8$$

where (u_1, v_1) are the coordinates of the selected pixel of the first image and $(u_2, v)_2$ the coordinates of the same pixel of the second image. This means, that the gray value of the pixel with coordinates (u_1, v_1) for image I_1 is equal to the gray value of the pixel with coordinates $(u_2, v_2\,)$ for image I_2.

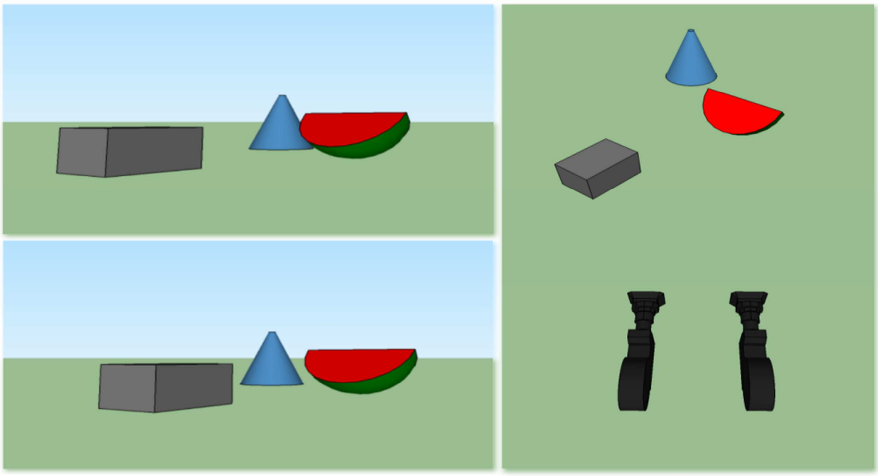

Figure 46: A scene with geometric primitives. Right scene: camera setup.
Left top: right camera view. Left bottom: left camera view.

The *"Acoustic Mouse"* transducer is moved only in one direction. The resulting shift is described by the unknown function $z(u, v)$. We express $(u_2, v_2\,)$ through the function $z(u, v)$ and rewrite equation 4.3-8:

$$I_1(u_1, v_1) = I_2(u_1 + z(u_1, v_1), v_1) \qquad 4.3\text{-}9$$

or

$$I_1(u_1, v_1) - I_2(u_1 + z(u_1, v_1), v_1) = 0. \qquad 4.3\text{-}10$$

Of course, equation 4.3-10 holds for the idealized scenes and it cannot be satisfied easily by any choice of function $z(u, v)$. Equation 4.3-11 accommodates this shortcoming:

$$|I_1(u_1, v_1) - I_2(u_1 + z(u_1, v_1), v_1)| \rightarrow min\,, \qquad 4.3\text{-}11$$

or with a squared norm

$$|I_1(u_1, v_1) - I_2(u_1 + z(u_1, v_1), v_1)|^2 \rightarrow min. \qquad 4.3\text{-}12$$

Equations 4.3-11 and 4.3-12 serve minimizing the difference between first and second image under the shift $\mathrm{z(u, v)}$. We use equation 4.3-12 to deal with negative and positive deviations in the same manner. Furthermore, quadratic penalizing leads to a linear system of equations (Black, 1991), (Mèmin, 1998), (Kosov, 2007).

After this step we can write the data term under the gray value constancy assumption:

$$DataTerm(u, v, z) = |I_1(u, v) - I_2(u + z(u, v), v)|^2. \qquad 4.3\text{-}13$$

4.3.4. Smoothness Term

The smoothness term results from the additional assumption of a globally smooth disparity field; neighbored regions belong to the same object and have similar depth. The smoothness term redistributes the computed information and blurs depth outliers. It also fills problematic regions with data calculated from neighboring regions when the data term doesn’t yield reliable information.

The simplest smoothness term is based on homogeneous regularizer:

$$SmoothnessTerm(z_u, z_v) = \varphi|\nabla z|^2, \qquad 4.3\text{-}14$$

with: $|\nabla z| = \sqrt{z_u^2 + z_v^2}$.

The parameter φ is introduced to control how much the smoothness term may prevail above the data term. The larger the parameter φ, the smoother is the result. Too large values of φ can completely destroy the result given by the data term. Therefore, the parameter φ has to be chosen carefully.

Forming the Euler-Lagrange equation based on the general notation 4.3-7, we differentiate the smoothness term 4.3-14 turning it into the Laplacian Δz. The Laplacian is a core of a simple linear diffusion process that is equivalent to the Gaussian blur filter (Weickert, 1998).

4.3.5. The Euler Lagrange Equation

After we have constructed the data term and the smoothness term, we are able to combine them in our functional 4.3-5:

$$E\big(z(u, v)\big) = \iint_\Omega \left|I_1(u, v) - I_2(u + z(u, v), v)\right|^2 + \varphi|\nabla z|^2 \, du \, dv. \qquad 4.3\text{-}15$$

Before forming the Euler-Lagrange equation, we implement a penalizing function $\Psi(s^2)$ for data improvement. In formulation 4.3-15 we use a quadratic penalizer. In this case outliers get too much influence on the estimation process. Brox et al. (Brox, 2004) suggest to apply a concave function $\Psi(s^2)$ which is given by the absolute value function

$$\Psi(s^2) = \sqrt{s^2 + \lambda^2}, \qquad 4.3\text{-}16$$

where λ is a small constant. Function 4.3-16 is convex by definition and leads to a robust state making it easier to minimize the energy functional. Furthermore, function Ψ penalizes the outliers gentler and can be controlled by the parameter λ.

Considering the smoothness term, we can notice, that the constructed smoothness assumption implies a resulting disparity without discontinuities. However, this is not the case for real scenes, and neither for ultrasound sector scans. We want the boundaries preserved but not smoothed. The Laplacian in the current formulation of the smoothness term 4.3-14 corresponds to the Gaussian blurring process that is isotropic in all directions and doesn't preserve any edges or boundaries. When we want to preserve discontinuities and edges from smoothing we have to modify smoothing in regions with discontinuities. We apply piecewise smoothness function as a penalizer of disparity variations. Thus we use the same function Ψ introduced in equation 4.3-16 for the smoothness term.

Adding penalizer Ψ into functional 4.3-15 leads to a robust energy (Black, 1991), (Mèmin, 1998):

$$E\big(z(u,v)\big) = \iint_\Omega \Psi\left(\left|I_1(u,v) - I_2(u+z(u,v),v)\right|^2\right) + \varphi\Psi(|\nabla z|^2)\, du\, dv. \qquad 4.3\text{-}17$$

We apply the same function Ψ to both the data term and the smoothness term. We can use different functions or the same type of function but with different parameter values for λ.

Function F in this case should is written as follows:

$$F = \Psi\left(\left|I_1(u,v) - I_2(u+z(u,v),v)\right|^2\right) + \varphi\Psi(|\nabla z|^2). \qquad 4.3\text{-}18$$

Now we may set up the Euler-Lagrange equation (see equation 4.3-7). First, we perform the partial differentiation for the data term 4.3-13:

$$\frac{dF}{dz} = \Psi'(|I_1(u,v) - I_2(u+z,v)|^2) \cdot -2\big(I_1(u,v) - I_2(u+z,v)\big) I_{2u}(u+z,v). \qquad 4.3\text{-}19$$

The smoothness term of the Euler-Lagrange equation can be derived according to:

$$\frac{d}{du}F_{z_u} + \frac{d}{dv}F_{z_v} = 2\varphi\, div(\Psi'(|\nabla z|^2) \cdot \nabla z), \qquad 4.3\text{-}20$$

with: $\Psi'(s^2) = \frac{\lambda}{\sqrt{s^2+\lambda^2}}$ and λ the contrast regulation parameter.

Now, we can cancel the common factor "–2" in both equations and combine equations 4.3-19 and 4.3-20 into the Euler-Lagrange equation.

$$\begin{aligned}\Psi'(|I_2(u+z,v)-I_1(u,v)|^2)&\\ \cdot\big(I_2(u+z,v)-I_1(u,v)\big)I_{2u}(u+z,v)&\\ -\varphi\, div(\Psi'(|\nabla z|^2)\cdot\nabla z)=0.&\end{aligned} \qquad 4.3\text{-}21$$

Before discretizing or applying some numerical scheme to this equation we describe the diffusion process and explain how discontinuities can be preserved for improved results.

Diffusion is a physical process that equilibrates concentration differences and preserves mass. A mixture of liquids in a jar is an example for a real diffusion process with uniform temperature transport and slow mixing of liquids. Mathematically diffusion equation can be written in PDE form (Partial Differential Equation) by means of the Fick’s law (Fick, 1855) and mass balance:

$$\partial_t u = div(D\nabla u). \qquad 4.3\text{-}22$$

In the anisotropic case, the diffusion flux $D\nabla u$ is not parallel to ∇u and the diffusion tensor D is a symmetric positive definite matrix describing the diffusion power as a function of direction angle. In the isotropic case, the diffusion flux is parallel to ∇u and the diffusion tensor degenerates to the scalar valued diffusivity function g. In this paper we deal only with isotropic diffusion.

If the diffusion tensor D is constant over the whole image domain, we call the process homogeneous diffusion; space-dependent filtering is called inhomogeneous diffusion. For example, the linear diffusion is homogeneous, since it does not depend on the image structure and can be treated as a Gaussian convolution (blurring) process (Weickert, 1998).

The Gaussian convolution (i.e. linear diffusion filtering) is common in image processing. However, it has some important disadvantages. During smoothing the flat regions of the image, it blurs also all image structures, which are semantically important - edges or other discontinuities. It also dislocates image structures. Nonlinear diffusion filtering can be a remedy to these problems.

Opposite to linear diffusion, nonlinear diffusion does not affect the image domain similarly. It attenuates the smoothness power depending on image peculiarities, such as edges. The main idea of nonlinear diffusion filtering is to smooth the entire image domain but with different strength depending on the image gradient. We reformulate diffusion equation 4.3-22 and add a diffusivity function that is sensitive to image gradients and acts as an attenuation function of the diffusion process:

$$\partial_t u = div(g(|\nabla u|^2)\nabla u). \qquad 4.3\text{-}23$$

The diffusivity function g has to be a monotonically decreasing and continuously differentiable function. In literature, among nonlinear diffusivities, the Charbonier and the Perona-Malik diffusivity functions are popular (Weickert, 2001), (Cohen, 1993), (Schnörr, 1994). For our work, we will use the Charbonier diffusivity function, since it fits our case with acceptable results. In their paper (Charbonnier, 1994), Charbonier et. al. suggest a slight modification of the Perona-Malik diffusivity (Perona, 1990). The Charbonier diffusivity function 4.3-24 does not only reduce the diffusivity power in regions with greater gradient being more likely edges but also possesses an edge-preserving regularization without enhancing edges. Therefore it does not suffer from stair-casing effect, unlike the Perona-Malik diffusivity function:

$$g_{Ch}(|\nabla u|^2) = \frac{\lambda}{\sqrt{|\nabla u|^2 + \lambda^2}},\ with\ \lambda > 0, \qquad 4.3\text{-}24$$

where λ is an adjustable contrast parameter. The flux function 4.3-25 of equation 4.3-24 shows that the Charbonier diffusivity leads to an edge preserving behavior, since the flux function is positive in the whole interval:

$$\Phi_{Ch}(s) = g_{Ch}(s^2) \cdot s = \frac{\lambda \cdot s}{\sqrt{s^2 + \lambda^2}},\ with\ \lambda > 0, \qquad 4.3\text{-}25$$

The parameter λ is the adjustable contrast regulator: diffusivity tends to zero for structures with $|\nabla u|^2 > \lambda$, since they are regarded as edges; for structures with $|\nabla u|^2 < \lambda$ diffusivity tends to one and those structures are regarded as interior regions. Figure 47 plots the Charbonier diffusivity and its flux function.

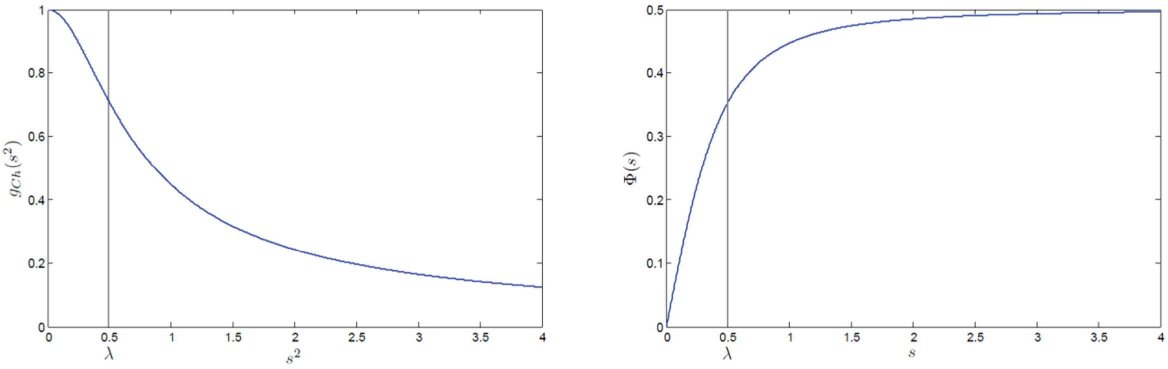

(a) **(b)**

Figure 47: The Charbonier regularization: (a) diffusivity, (b) flux.

Now we return to formulation 4.3-19 and 4.3-20. We notice that the function $\Psi'(|\nabla z|^2)$ from 4.3-20 has the same meaning as the diffusivity function $g_{Ch}(|\nabla u|^2)$ in 4.3-24 and the term $\Psi'(|\nabla z|^2) \cdot \nabla z$ is the same as the flux $\Phi_{Ch}(s)$ from 4.3-25. This observation shows the similarities between diffusion processes and the smoothness term of the optical flow formulation.

In equation 4.3-17 we stated that we use penalizing technique for the control of outliers in the data term. After setting up the data term, we improve its robustness by applying a regularizing function. To simplify matters, we used the same Charbonier diffusivity function for penalizing but with another parameter λ. We distinguish the λ parameter by indices the letters d for the data term and the letter s for the smoothness term respectively. Let us modify the minimizer 4.3-17 and the Euler-Lagrange equation 4.3-21 according to these extensions and we obtain equations 4.3-26 and 4.3-27:

$$E\big(z(u,v)\big) = \iint_{\Omega} \Psi_d\left(\left|I_1(u,v) - I_2(u+z(u,v),v)\right|^2\right) + \varphi\Psi_s(|\nabla z|^2)\,du\,dv. \qquad 4.3\text{-}26$$

The non-quadratic penalization Ψ'_d in the data term of the equation 4.3-27 renders the estimation more robust. This strategy allows regularizing the outliers in a not so severe manner than in quadratic setting.

$$\begin{gathered}\Psi'_d(|I_2(u+z,v) - I_1(u,v)|^2)\\ \cdot\big(I_2(u+z,v) - I_1(u,v)\big)I_{2u}(u+z,v) -\\ \varphi\, div(\Psi'_s(|\nabla z|^2)\cdot\nabla z) = 0.\end{gathered} \qquad 4.3\text{-}27$$

Now we are ready to discretize the equation 4.3-27 and estimate the solution of the minimizer 4.3-26.

4.4. Numerical Scheme

To solve the equation 4.3-27 numerically, we derive a Jacobi-like iteration numerical scheme, but we have to get rid of the implicitness in functions $I_2(u+z,v)$ and $I_{2u}(u+z,v)$. The first order Taylor series can be applied to this problem (Brox, 2004), but this method allows only small perturbations and shifts. For transducer tracking by optical flow analysis of sector scans we cannot guarantee this condition. Linear interpolation is another approach to get rid of implicitness in the data term. This method is closer to numerical schemes and deals with discrete data with large displacements, which allows overcoming the problem of first order Taylor series (Kosov, 2007). In practice, the input sector scans $I_i(x,y)$ are represented as two-dimensional matrices or discrete functions: $I_i(x,y)$: $N^+ \times N^+ \to R$.

In other words, the arguments of these discretized functions must be natural numbers including zero. However, the value of the function $z(u,v) \in Q$ is a rational number. Therefore, the value of the argument $x + z \in Q$ is rational as well. We apply the linear interpolation method to overcome this problem: we present the term $z(u,v) \in Q$ as a sum of two values – an integer value $A \in N^+$ and a small floating point value $b \in R$, where $|b| < 1$. Using this notation we can reform I:

$$I(u+z,v) = I(u+A+b,v). \qquad 4.4\text{-}28$$

Using linear interpolation, the parameters of the function I are also integer:

$$I(u+A+b,v) = (1-|b|)\cdot I(u+A,v) + |b|\cdot I(u+A+sgn(b),v). \qquad 4.4\text{-}29$$

Simplifying equation 4.4-29 we obtain:

$$I(u+A+b,v) = (1-|b|)\cdot I(u+A,v) + |b|\cdot I(u+A+sgn(b),v) = I(u+A,v) + |b|\cdot\big(I(u+A+sgn(b),v) - I(u+A,v)\big). \qquad 4.4\text{-}30$$

Let us look more precisely on a selected term 4.4-31:

$$|b|\cdot\big(I(u+A+sgn(b),v) - I(u+A,v)\big). \qquad 4.4\text{-}31$$

We notice that a term like 4.4-31 can be understood as a first derivative of I and can be substituted with the forward or backward difference scheme with a grid step $\Delta u = 1$. Equation 4.4-32 shows the transformation of this term:

$$|b|\cdot\big(I(u+A+sgn(b),v) - I(u+A,v)\big) = sgn(b)\cdot|b|\cdot\big(I_u(u+A,v)\big) = b\cdot\big(I_u(u+A,v)\big). \qquad 4.4\text{-}32$$

Note, that for $b \geq 0$ we use a forward and for $b < 0$ a backward difference approximation.

Now we can form 4.4-32 back into 4.4-30 and obtain the approximation 4.4-33.

$$I(u+A+b,v) = I(u+A,v) + b\cdot\big(I_u(u+A,v)\big). \qquad 4.4\text{-}33$$

Since the function $I_u(u+z,v)$ is a piecewise constant function, we also assume the approximation 4.4-34:

$$I_u(u+z,v) = I_u(u+A+b,v) \approx I_u(u+A,v). \qquad 4.4\text{-}34$$

The values A and b are input data set initially. Based on experience we choose $A = \pm 8$ for larger shift between sector scans. For small shifts of the sensor positions we choose $A = 0$. The initial value of b is chosen to be constant in the interval (-1,+1). Without loss of generality, we may substitute two terms of the Euler-Lagrange equation 4.3-27 by symbolic constants. We do this for the simplicity of explanations.

$$G \coloneqq \Psi'_d(|I_2(u+z,v) - I_1(u,v)|^2), \qquad 4.4\text{-}35$$
$$g \coloneqq \Psi'_s(|\nabla z|^2).$$

Rewriting equation 4.3-27 and using the shortened terms 4.3-35, we get our new Euler-Lagrange equation 4.4-36:

$$G\cdot\big(I_2(u+z,v) - I_1(u,v)\big)\cdot I_{2u}(u+z,v) - \varphi\, div(g\cdot\nabla z) = 0. \qquad 4.4\text{-}36$$

Now we develop the Euler-Lagrange equation 4.4-36 according to equations 4.4-28 to 4.4-34:

$$G\cdot\big(I_2(u+A,v) - I_1(u,v) + b\cdot I_{2u}(u+A,v)\big)I_{2u}(u+A,v) - \varphi\, div(g\cdot\nabla z) = 0. \qquad 4.4\text{-}37$$

We go to discretize this version of the Euler-Lagrange equation 4.4-37. After discretization, we will solve it with respect to b and obtain a new $b*$, which is the new input for the next iteration step. There exist several approaches to discretize a system of linear equations. One of them is the time-marching numerical approach. When discretizing the Euler-Lagrange equation 4.4-27 we obtain a non-linear system of equations. Thus, we can refer to the time-marching numerical scheme that considers this equation as a steady state of the evolution 4.4-38:

$$\frac{dz}{dt} = \Psi'(|I_2(u+z,v) - I_1(u,v)|^2) \cdot \left(I_2(u+z,v) - I_1(u,v)\right) \cdot I_{2u}(u+z,v) - \varphi\, div(\Psi'(|\nabla z|^2) \cdot \nabla z). \tag{4.4-38}$$

The time-marching approach indicates that at some moment in time we will achieve a steady state when function $z(u,v)$ does not change in time, i.e. $\frac{dz}{dt} \xrightarrow[t\to\infty]{} 0$.

This scheme is iterative and can take a lot of computation time to gain a steady-state. For better performance one can use a multi-grid method (Brand, 1977) or the linearization approach. However, when using the time-marching approach the convergence and steady state can be reached only for a large number of iterations.

Another discretization method of linear differential equations is the Successive Over Relaxation technique or SOR scheme (Young, 1971) that speeds up the convergence of the numerical algorithm greatly. The main idea of the SOR algorithm is an iterative Jacobi-like scheme based on an "over-prediction" by means of linear extrapolation. Let us apply this scheme to our problem formulation 4.4-37. Rearranging 4.4-37 we get:

$$G \cdot \left(I_2(u+A,v) - I_1(u,v)\right) \cdot I_{2u}(u+A,v) + b \cdot G \cdot I_{2u}^2(u+A,v) - \varphi\, div(g \cdot \nabla z) = 0. \tag{4.4-39}$$

First, we discretize the smoothness term of 4.4-39. Let us denote

$$z_{i,j} = z(i\Delta u, j\Delta u),\ g_{i,j} = g(i\Delta u, j\Delta v),\ G_{i,j} = G(i\Delta u, j\Delta v)$$

and rewrite the smoothness term of the Euler-Lagrange equation separately:

$$SmTerm_{ELE} = -\varphi div(g \cdot \nabla z) = -\varphi div\left(g_{i,j} \cdot \nabla z_{i,j}\right) = -\varphi\left(\partial_u\left(g_{i,j} \cdot \left(z_{i,j}\right)_u\right) + \partial_v\left(g_{i,j} \cdot \left(z_{i,j}\right)_v\right)\right). \tag{4.4-40}$$

Now we discretize the term $\partial_u\left(g_{i,j} \cdot \left(z_{i,j}\right)_u\right)$:

$$\partial_u\left(g_{i,j} \cdot \left(z_{i,j}\right)_u\right) = \partial_u\left(g_{i+1/2,j} \cdot \frac{z_{i+1,j} - z_{i,j}}{\Delta u}\right) = \frac{g_{i+1,j} + g_{i,j}}{2} \cdot \frac{z_{i+1,j} - z_{i,j}}{\Delta u} - \frac{g_{i,j} + g_{i-1,j}}{2} \cdot \frac{z_{i,j} - z_{i-1,j}}{\Delta u}. \tag{4.4-41}$$

The second term $\partial_v\left(g_{i,j}\cdot\left(z_{i,j}\right)_v\right)$ can be discretized in the same way. Assuming grid steps in u and v directions equal to 1, i.e. $\Delta u = \Delta v = 1$, we can rewrite equation 4.4-40:

$$SmTerm_{ELE} = -\varphi div(g\cdot\nabla z) = -\varphi\left(\frac{g_{i+1,j}+g_{i,j}}{2}\cdot\left(z_{i+1,j}-z_{i,j}\right) - \frac{g_{i,j}+g_{i-1,j}}{2}\cdot\left(z_{i,j}-z_{i-1,j}\right) + \frac{g_{i,j+1}+g_{i,j}}{2}\cdot\left(z_{i,j+1}-z_{i,j}\right) - \frac{g_{i,j}+g_{i,j-1}}{2}\cdot\left(z_{i,j}-z_{i,j-1}\right)\right). \quad 4.4\text{-}42$$

Simplifying 4.4-42 we get:

$$SmTerm_{ELE} = -\varphi\ div(g\cdot\nabla z) = -\frac{\varphi}{2}\Big(\left(g_{i+1,j}+g_{i,j}\right)z_{i+1,j} + \left(g_{i,j}+g_{i-1,j}\right)z_{i-1,j} + \left(g_{i,j+1}+g_{i,j}\right)z_{i,j+1} + \left(g_{i,j}+g_{i,j-1}\right)z_{i,j-1} - \left(4g_{i,j}+g_{i+1,j}+g_{i-1,j}+g_{i,j+1}+g_{i,j-1}\right)z_{i,j}\Big). \quad 4.4\text{-}43$$

For the Tichonov diffusivity function, where

$$g_{i,j} = 1, \forall i,j$$

we get the standard Laplacian discretization:

$$SmTerm_{ELE} = -\varphi\ div(\nabla z) = -\varphi\left(z_{i+1,j} - 2z_{i,j} + z_{i-1,j} + z_{i,j+1} - 2z_{i,j} + z_{i,j-1}\right). \quad 4.4\text{-}44$$

One can notice that equations 4.4-43 and 4.4-44 represent high-pass filtering. We continue discretizing of 4.4-39 with the discretization of the data term of the Euler-Lagrange equation omitting the function argument indexing:

$$DataTerm_{ELE} = G_{i,j}\cdot\left((I_2)_{i+A,j} - (I_1)_{i,j}\right)\cdot(I_{2u})_{i+A,j} + b\cdot G_{i,j}\cdot(I_{2u}^2)_{i+A,j}. \quad 4.4\text{-}45$$

Now we combine both terms and build the resulting discretization of the Euler-Lagrange equation 4.4-46, setting $z_{i,j} = A + b$ according to equation 4.4-28:

$$G_{i,j}\cdot\left((I_2)_{i+A,j} - (I_1)_{i,j}\right)\cdot(I_{2u})_{i+A,j} + b\cdot G_{i,j}\cdot(I_{2u}^2)_{i+A,j} - \frac{\varphi}{2}\Big(\left(g_{i+1,j}+g_{i,j}\right)z_{i+1,j} + \left(g_{i,j}+g_{i-1,j}\right)z_{i-1,j} + \left(g_{i,j+1}+g_{i,j}\right)z_{i,j+1} + \left(g_{i,j}+g_{i,j-1}\right)z_{i,j-1} - \left(4g_{i,j}+g_{i+1,j}+g_{i-1,j}+g_{i,j+1}+g_{i,j-1}\right)(A+b)\Big) = 0. \quad 4.4\text{-}46$$

Then we perform Jacobi iteration by choosing all the terms b' from the discretized Euler-Lagrange equation except of the argument of the $G_{i,j}$ function from the next iteration step:

$$\begin{aligned} G_{i,j} \cdot \left((I_2)_{i+A,j} - (I_1)_{i,j} \right) \cdot (I_{2u})_{i+A,j} + b' \cdot G_{i,j} \cdot (I_{2u}^2)_{i+A,j} & \\ - \frac{\varphi}{2} \Big(\left(g_{i+1,j} + g_{i,j} \right) z_{i+1,j} + \left(g_{i,j} + g_{i-1,j} \right) z_{i-1,j} & \\ + \left(g_{i,j+1} + g_{i,j} \right) z_{i,j+1} + \left(g_{i,j} + g_{i,j-1} \right) z_{i,j-1} & \\ - \left(4g_{i,j} + g_{i+1,j} + g_{i-1,j} + g_{i,j+1} + g_{i,j-1} \right) (A + b') \Big) & \\ = 0 & \end{aligned} \qquad 4.4\text{-}47$$

where

$$G_{i,j} = \Psi'_d \left(\left| (I_2)_{i+A,j} + |b| \cdot \left((I_2)_{i+A+sgn(b),j} - (I_2)_{i+A,j} \right) - (I_1)_{i,j} \right|^2 \right).$$

Now let us rearrange all the b' to the left hand side of the equation:

$$b' = \frac{ \begin{gathered} G_{i,j} \cdot \left((I_2)_{i+A,j} - (I_1)_{i,j} \right) \cdot (I_{2u})_{i+A,j} \\ - \frac{\varphi}{2} \begin{pmatrix} \left(g_{i+1,j} + g_{i,j} \right) z_{i+1,j} + \left(g_{i,j} + g_{i-1,j} \right) z_{i-1,j} + \left(g_{i,j+1} + g_{i,j} \right) z_{i,j+1} \\ + \left(g_{i,j} + g_{i,j-1} \right) z_{i,j-1} - \left(4g_{i,j} + g_{i+1,j} + g_{i-1,j} + g_{i,j+1} + g_{i,j-1} \right) A \end{pmatrix} \end{gathered} }{ -G_{i,j} \cdot \left(I_{2u}^2 \right)_{i+A,j} - \frac{\varphi}{2} \left(4g_{i,j} + g_{i+1,j} + g_{i-1,j} + g_{i,j+1} + g_{i,j-1} \right) }. \qquad 4.4\text{-}48$$

The new value of the solution is calculated using the previous value of *A* and the newly calculated value of *b*:

$$z' = A + b'. \qquad 4.4\text{-}49$$

In this case, the value of b' has not to satisfy $|b'| < 1$.
The implementation of the SOR numerical scheme (Young, 1971) follows the following steps:

1. Initial guess for $z_{i,j}$ for all points (*i*,*j*).
2. Define a scalar value $0 < w_n < 2$.
3. Apply equation 4.4 - 48 and 4.4 - 49 to all interior points *(i,j)* and obtain $z'_{i,j}$.
4. Calculate $z_{i,j}^* = w_n z'_{i,j} + (1 - w_n) z_{i,j}$.
5. Stop if the method has already reached the convergence threshold.
6. Replace $z_{i,j} = z_{i,j}^*$.
7. Repeat from step 2.

For the scalar $w_n=1$ one can recover the Jacobi scheme, while the value $w_n<1$ under-relaxes the solution. In ideal case, the value w_n has to be chosen in such a way, that it provides the optimal rate of convergence, thus this value is not restricted to a fixed constant. After some numbers of iterations the estimating process reaches the convergence state. We can stop iterating with the output solution $z_{i,j}$. It is also possible to perform a given number of iterations. In this case we can overestimate or underestimate the problem, however with the advantage of equal running times for each input sector scan pair.

The solution $z_{i,j}$ represents the horizontal shift for each pixel of the input sector scans. These values are a relative measure, i.e. in pixels, but not integer values. Therefore they can be part of the pixel dimension as well. The acoustic-mouse algorithm has to simplify $z_{i,j}$ somehow since we want to get a scalar value as output with appropriate resolution. The resolution is given as a parameter of the sector-scan reconstruction module. In this way we obtain values for the transducer motion for the given pair of sector scans.

For the simplification algorithm we choose a min-max function: we find the value Δ that corresponds to the maximum absolute value of the resulting optical-flow; the value Δ is the shift in pixels, which is to be converted into millimeters. For this conversion one uses the parameter “resolution” of the reconstruction module. The described technique and algorithms allow us to obtain a relative shift for the given pair of sector-scans. Accumulating the relative shift for each of iterations, we can track the absolute transducer position.

Appendix B contains the parameter calibration strategies to allow a proper parameter selection. We suggest addressing to this appendix for a more detailed description of the calibrated parameters.

Chapter 5. Experimental Part: Approaches and Solutions

As was shown before, the progress made in recent years in computing, real-time signal processing, microelectronics and micro-packaging is promising to meet the technical challenges of a “self-tracker” system development, as we have called the manual quantitative inspection equipment. We have outlined developments in ultrasonic system engineering that are essential for the realization of the “self-tracker” inspection system. However, we still would need matrix transducers for transducer motion tracking: optical flow analysis of sector scan image sequences as an ill posed problem is challenging for more sophisticated and time consuming approaches. Moreover, linear arrays do not focus in 3D. Therefore we have to limit research and development to the principle viability: algorithms and the laboratory demonstrator are only developed for linear transducer motion with the view on later integration of free surface scanning including transducer swivelling.

The experiments described in this chapter prove the algorithm performance in respect to accuracy of position measurement and the ability to identify previous transducer positions after lift-off situations.

5.1. Experimental Setup of the “Acoustic Mouse”

The experiments have been conducted using the phased array system described in (von Bernus, 2006). We have used test samples with artificial flaws and samples without flaws.

5.1.1. System Components

As presented by Figure 48 the experimental setup consists of the ultrasonic equipment, the ultrasonic transducer, the test sample, and the computer with software developed for the experiments.

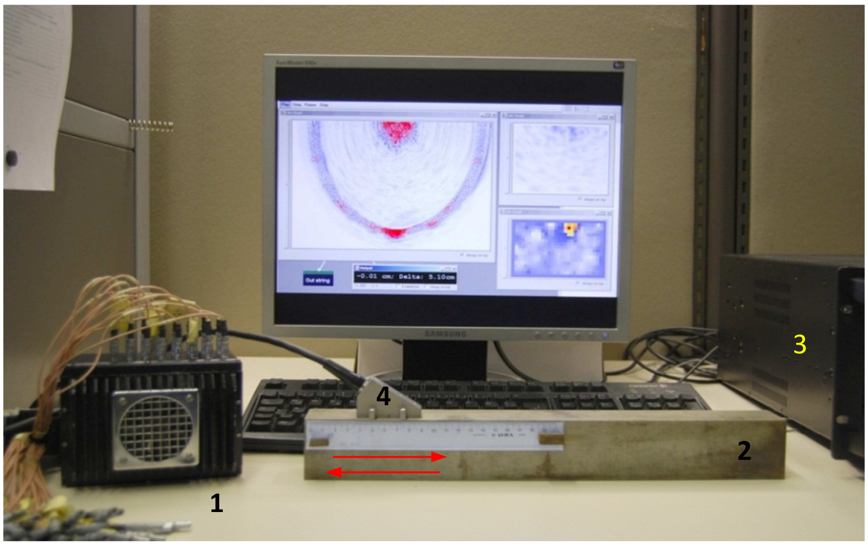

Figure 48: Setup for Transducer Motion Tracking Experiments.

The numbers given in Figure 48 indicate the main components:

1. Ultrasonic Multi-Channel Microelectronics (16-channel µUSE Module, IEEE1394 (Fire Wire, i.Link) - 800Mbit/s)
2. Fine grained structural ferrite steel test sample (see Figure 49)
3. Personal Computer
4. Linear Phased Array Transducer

The multichannel ultrasonic microelectronics, µUSE was developed by (Bulavinov, 2005) and also described in (Bulavinov, 2005). The computational module is designed for fast real-time data-pre-processing of mechanized ultrasonic inspection data. The µUSE-frontend is capable to provide test data at very high repetition rates: each channel of the module can be programmed to function as a transmitting and receiving channel. They can be operated in parallel. The full A-scan information of each channel is processed in real-time. The electronic design meets all standards of ultrasonic instrument specifications.

For our experiments we have used commercial linear phased array transducers. They are different in respect to technical characteristics that determine their specific use in NDT: number of elements, frequency, active aperture, etc. We scanned only plane surfaces. All transducers have been used without wedges. Table 4 lists the array transducers.

	Transducer number	**Frequency (MHz)**	**Number of elements**	**Pitch (mm)**	**Aperture (mm)**	**Near-field (mm steel)**	**Focal Ø(mm)**
1.	5L16 – A1	5	16	0,59	9,6	36	2,5
2.	2L16 – A1	2	16	0,75	12	30	3,1

Table 4: Transducer parameters and dimensions.

The transducer #2 2L16-A1 can be also operated in shear wave mode due to the small element aperture of 0,75 mm less than half the shear wave length of 0,8 mm.

5.1.1.1. Test Specimen

We used test specimen with plane surface and optimal coupling conditions to minimize the coupling error for unambiguous evaluation of the tracking algorithm. One test specimen contains side drilled holes, the other one a fatigue crack. The side drilled holes have point like reflector characteristics and reduce the problem of ill-posed optical flow analysis due to their constant geometry in the third space dimension. The fatigue crack was chosen for its point like crack tip diffraction characteristic.

The test specimen can be seen in the photo of Figure 49, and its dimensions in the drawing of Figure 50, respectively Figure 51 for the second test block.

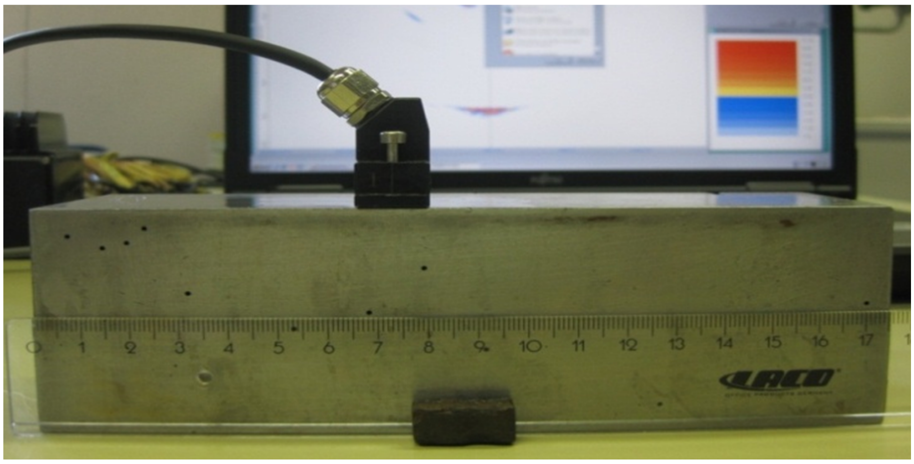

Figure 49: Test specimen with side drilled holes and fatigue crack.

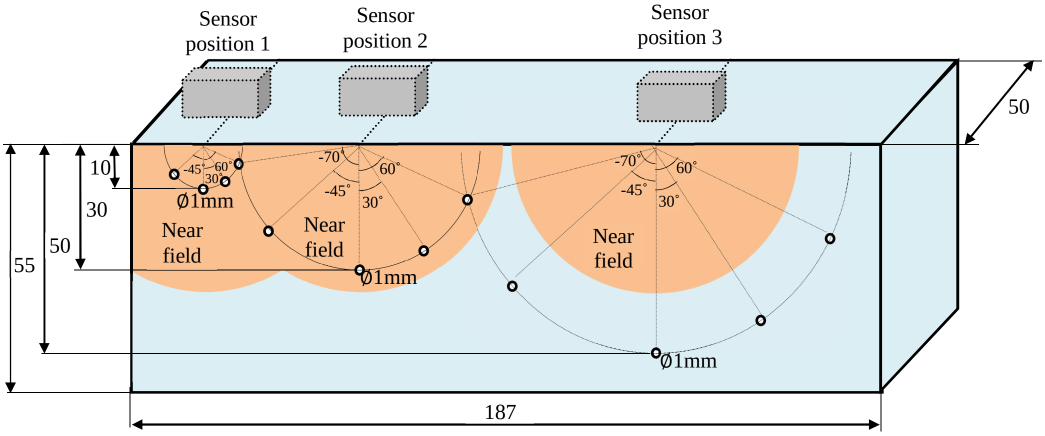

Figure 50: Dimensions of test specimen TK1, all numbers in mm. (Bulavinov, 2005).

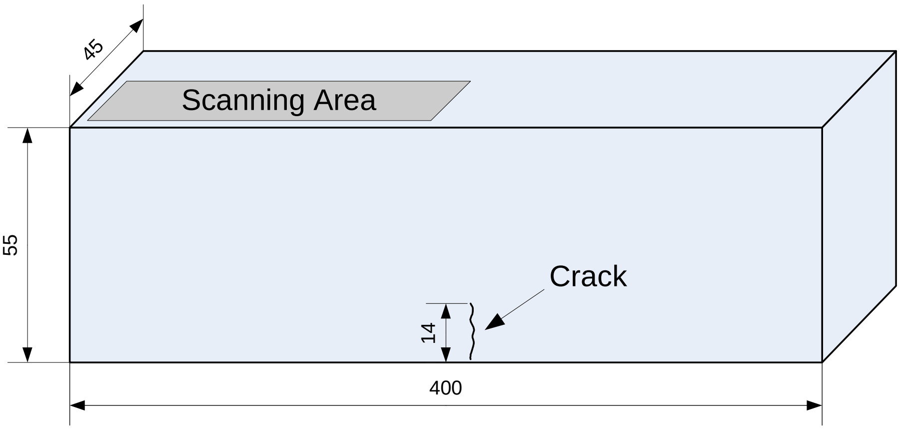

Figure 51: Dimensions of test specimen TK2, all numbers in mm.

5.1.1.2. Personal Computer and Software

We have used a high performance computer with two Intel® Xeon® Processors E5405 2 GHz (Cores 8), RAM of 4GB, and the graphic card NVIDIA GeForce 8800 GTX for our experiments. For implementing the *"Acoustic Mouse"* software, we have applied the programming language C#.NET.

The software package has been developed as Lab for user's convenience. It is structured by software modules with an optimized data flow for real time computing by its appropriate pipe-lining. The software package includes the following modules:

- Sector Scan Reconstruction Module SSRM: The SSRM can be implemented on GPU using CUDA technology or on CPU with the disadvantage of losing reconstruction speed; the choice depends on the computer configuration.
- Low-Pass Pre-filtering Module LPPM: This module was described in the previous chapter 4.3.1. We used it before applying the Optical Flow Module to obtain a pre-smoothed input. Pre-smoothing attenuates also additive noise and temporal aliasing effects in the image sequence. The filter reduces the contribution of high image fluctuation called *high frequencies* for more accurate estimation of the overall image gradient. In our experiments, smoothing is carried out on the input image.
- Optical Flow Calculation Module OFCM: This module calculates the optical flow field of two consecutive windowed sector scans. The applied variation minimization method is based on a gray-value constancy assumption that describes the motion model inside the set input image. Obtaining a 1D flow field, we can estimate the shift of sector scans used in the estimation process. We apply Gaussian filter for smoothing the resulting image. The Gaussian filter attenuates outliers in the flow field. Eventually, we calculate the maximum image value as the shift between two input sector scans.

- 2D Viewer Module 2DVM: This module visualizes 2D data by colour-mapping with programmable value intervals. By default, the map ranges colours from white to red through blue colour. Additionally, we can achieve image amplification or attenuation by appropriate gain parameter setting. Another type of visualization is a text data, which can output any results we want to print. We have also realized a text field visualizer with the opportunity for updating the measurement status.

In Figure 52 the outlined sequential algorithm execution is shown. The central idea is based on the analysis of the image information of sector-scans reconstructed by the SPA – technique. Corresponding to the specific objective of our research, the motion is tracked linearly along one axis or scan direction. The sequence of sector-scan images constitutes an optic flow field between two consecutive frames of this sequence. The position and positional changes of the *“Acoustic Mouse”* transducer are determined by optic flow analysis applying the variational method. Sector scans can be considered as image frames and differential methods for motion estimation can be applied. Moreover, optical flow techniques also include the problem of inferring to the structure of objects. Thus, we may structure the acoustic noise by computing patterns as a function of transducer position.

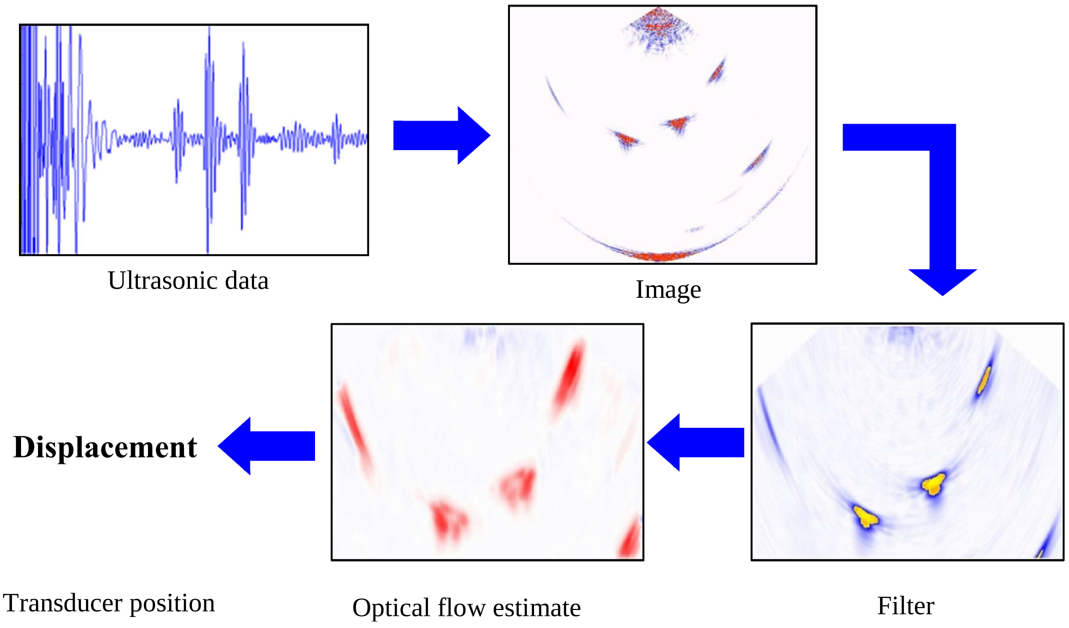

Figure 52: Software Modules.

The sector scan images backscattered acoustic noise and geometric reflectors but also signals imaged in the near surface zone called dead zone of a transducer. The dead zone is caused by the transducer characteristics and by the coupling quality and does not contain relevant information about the transducer position. Geometric reflectors, when present in the sector scan, are used for additional verification of computed position data.

In our case, the scan is linear and therefore one dimensional and we can substitute the vector field by a scalar field. In order to correctly estimate direction and velocity of transducer motion, we have to identify invariant optical flow field features of two consecutive frames. These additional constraints help to overcome the aperture problem of the optical flow algorithm. For this reason, we have chosen the variation method as one of the common techniques for image processing. As an important issue, we could recover the optical flow when minimizing the energy functional. Therefore, we could also take advantage of maximum entropy solver techniques.

5.2. Robustness Experiment

The robustness of the applied optical flow algorithm can be tested in respect to time dependent drift phenomena by an easy experiment: we place the transducer in one fixed position without any transducer motion. We compute the optical flow field and the resulting transducer motion that should be zero beside the effect of measurement and algorithmic errors. Therefore, the stability of the zero motion experiment informs about inherent algorithmic variation errors.

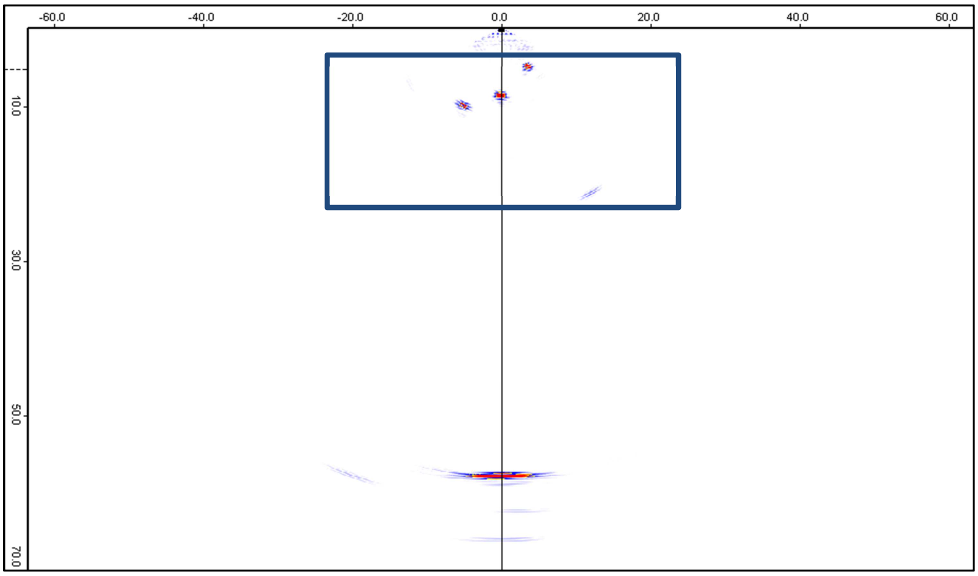

Figure 53: Sector Scan with Analysis Window.

We used the test block TK 1 with side drilled holes to avoid the contribution of stochastic noise variations caused by even smallest position or coupling changes. The transducer #1 5L16-A1 was positioned on test block TK1 above the side drilled hole #3 (counted from the left side) as it can be seen in Figure 50. The sound exit point distance to the specimen edge was 20 mm. The side drilled hole of Ø1 mm is located inside the indicated array near-field in a depth of 6.7 mm. The sector scan angle was chosen from -65° to +65°; the sound velocity of the longitudinal mode was determined as c_l = 5920 mm/sec. The analysis window for optical flow mapping covers an area of 45 mm x 25 mm of the array near-field including the side drilled holes. The sector scan image is characterized by the dead zone close to the transducer position, the back wall image at the bottom and the side drilled hole images in the center of the sector scan. The sector scan with the analysis window is shown in Figure 53 above.

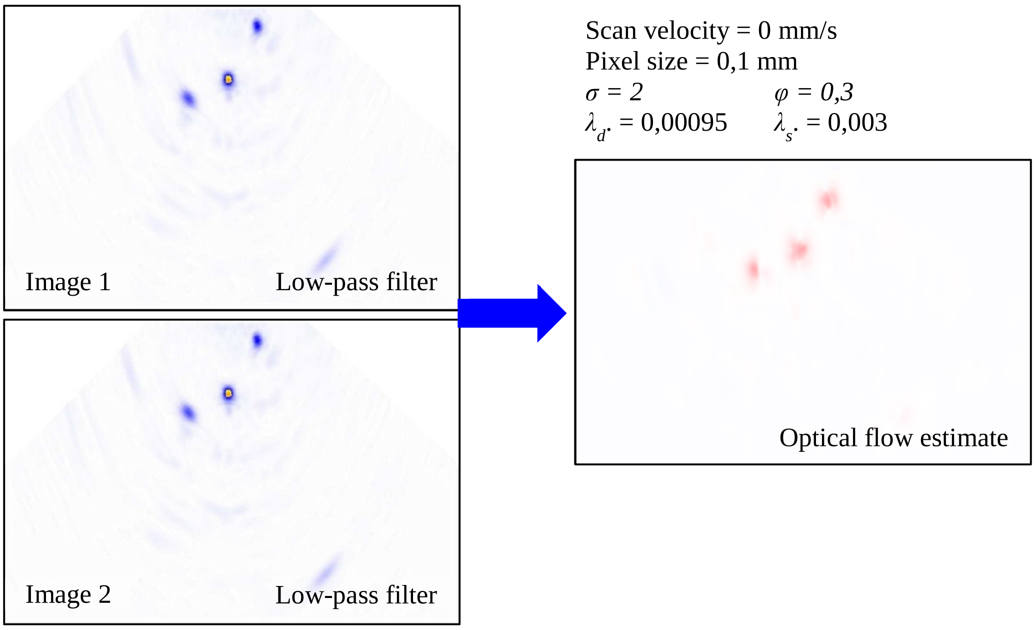

Figure 54: Window Sequence with Optical Flow Image.

An exemplary window image sequence is shown in Figure 54 together with the optical flow map. As expected, the optical flow estimation yields negligible small values as it can be seen in the color map. The map is rather homogeneous with values close to zero. Only the side drilled holes can be seen by choosing an appropriate sensitive scale. The mean value X of computed motion of hundred image pairs is less than half a micrometer. However, all values of the color map indicate a positive motion (in one direction) only. Negative values would appear in blue color. Nevertheless, this obvious algorithmic drift is much too small to be of technical concern being even smaller than the standard deviation of fluctuations pictured in Figure 55. We may conclude:

The mean value X and its standard deviation SD were stable without any noticeable time drift:

Stability Measure: $X = 0{,}0005 \pm 0{,}02$ (mm)

In ultrasonic testing we need for practical reasons an absolute accuracy of transducer position measurement of some few millimeters, a relative accuracy between two measurement positions in the range of half a wavelength. The applied wavelength λ of the 5 MHz transducer was 1.18 mm and we may conclude that the stability measure meets the requirements.

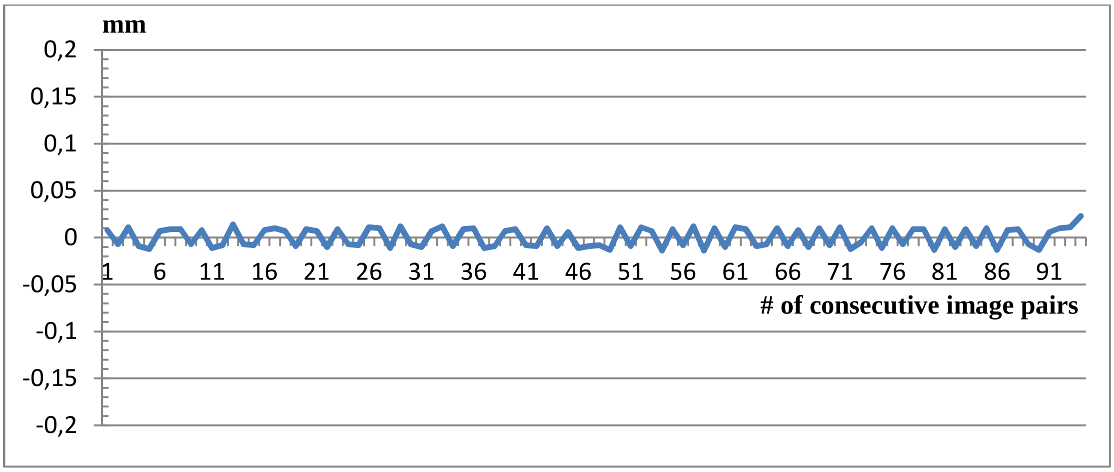

Figure 55: Algorithmic Fluctuations of Optical Flow Estimation.

5.3. Scanning Experiments

Scanning experiments have been performed with the following objectives:

- Accuracy of transducer position measurement
- Characterization of analysis window for optical flow mapping

Different error sources influence the achievable accuracy like calibration of optical flow in length units of the transducer motion and image features like local resolution, noise and artifacts. Artifacts can be caused by acoustic phenomena like multiple reflections at specific flaw or specimen geometries and by the applied image reconstruction algorithm called reconstruction artifacts.

The specification of the analysis window to be set by the inspection engineer is even more difficult in respect to the full picture on the required image content. The experimental strategy is based on worst case experiments complimented by some plausible assumptions.

5.3.1. Motion Tracking of Manipulator Supported Scans

The accuracy of transducer motion tracking is investigated by repeated measurements of the length of the linear scan as part of the calibration procedure and by the analysis of variations of computed step distances. We call the step distance scan index when it is constant along the full scan. The analysis of scan index variations can be done only by manipulator supported scanning that provides the required detailed position information.

We separate the problem of image content to conclude on the achievable accuracy of our optical flow algorithm. Therefore we experiment with real reflectors in the analysis window and with windows only filled by acoustic noise. For worst case consideration we took sector scan reconstructions with images blurred by reflector and reconstruction artifacts that usually are filtered for more precise flaw imaging. We have investigated the transducer positioning accuracy with all three transducers described above. Since there is no significant difference we limit our presentation on measurements with the transducer #1 5L16-A1 of Table 4. The 5 MHz array transducer with active 16 elements was scanned by a precision linear manipulator along the surface of test specimen TK1 as indicated in Figure 56.

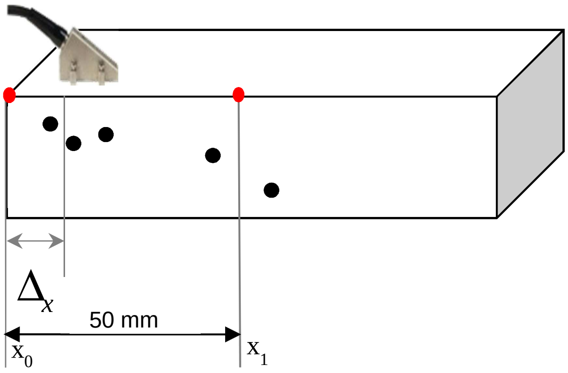

Figure 56: Scan on Test Specimen with side drilled holes.

The length of the full scan was 50 mm, the scan index 0.1 mm. The scanner has a specified absolute accuracy of 0.1 mm with a relative accuracy between two positions of 0.01 mm. This accuracy appears reasonable for ultrasonic inspections requiring a relative accuracy less than half a wavelength for high-end imaging systems based on synthetic aperture principles. However, we can only guess the error caused by the probe holder. Especially when starting the scan and coming to a stop the probe holder may cause a systematic shift that shortens the length of the scan. The size of this error cannot be measured directly but it can be seen by optical flow analysis.

In Figure 57, an exemplary sector scan sequence is shown with the image of side drilled holes #6, #7, #8 of test specimen TK 1, counted from the left edge. The analysis window was set in the focal area of the array transducer. For worst case considerations we have not processed the image; the reflectors are blurred and we can see the pulse train artifacts of the side drilled hole. The two sector scans given in Figure 57 represent the sector scan sequence for the scan index of 0.2 mm. The sector scan angle was chosen between -65° and +65°.

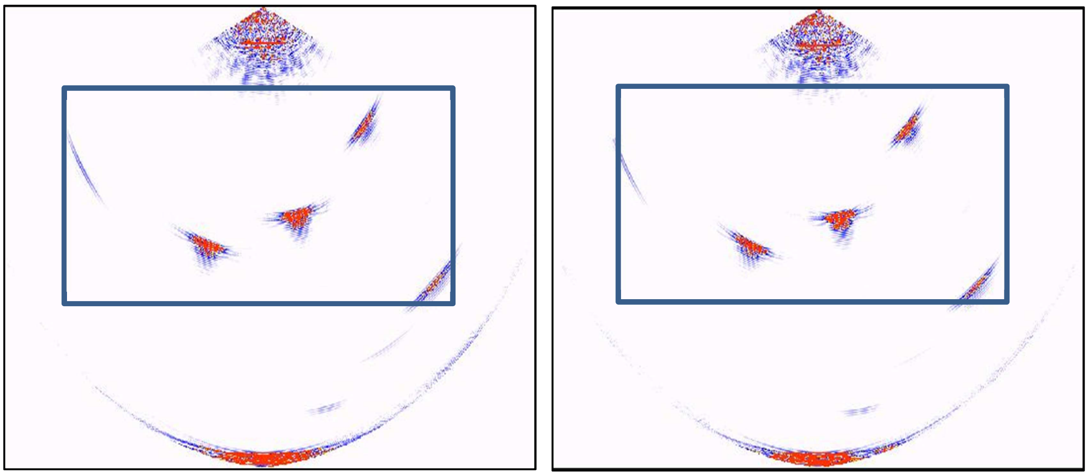

Figure 57: Exemplary Sector Scan Sequence with Analysis Window.

The details of the image windows are shown in Figure 58 together with the optical flow for the transducer motion of 0.2 mm.

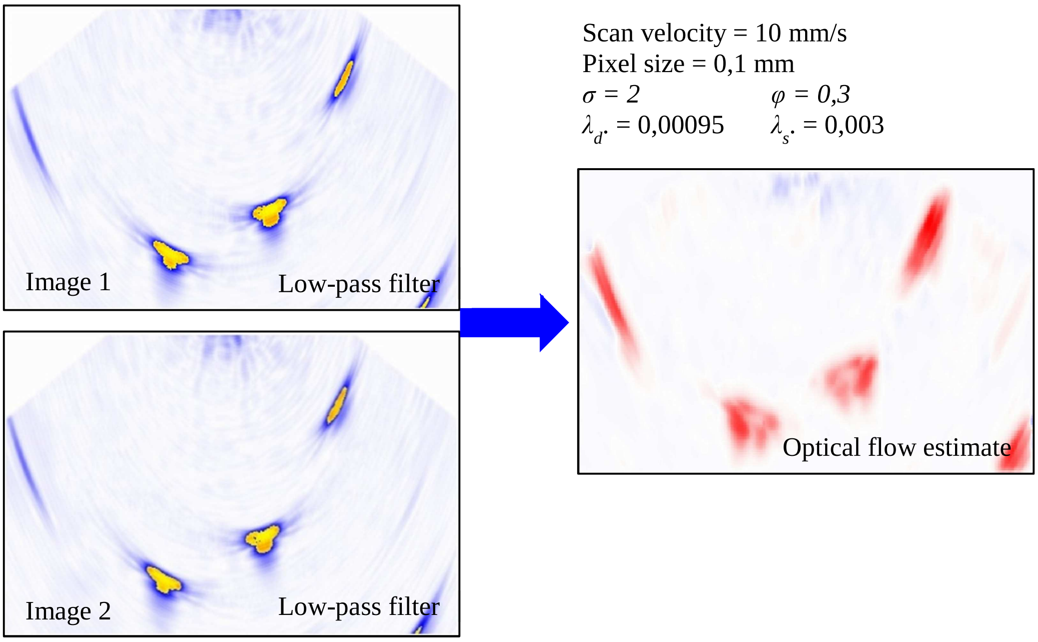
Scan velocity = 10 mm/s
Pixel size = 0,1 mm
$\sigma = 2$ $\varphi = 0{,}3$
$\lambda_{d'} = 0{,}00095$ $\lambda_{s'} = 0{,}003$

Figure 58: Representative Calibrated Optical Field.

For the frequency of 5 MHz the scan index of 0.1 mm was the smallest one that yields stable motion results. The maximum scan velocity had to be limited to 10 mm/sec due to the available efficient computing power for fast real-time optical flow analysis.

The scanner provides position information for each scan index point. Therefore we can analyze the position accuracy for all image sequences taken during the scan. We analyzed the accuracy at each scan index point and analyzing the optical flow for image pairs with a position change of 0.1 mm. Repeated measurements show excellent reproducibility as shown in Figure 59. The step index number 500 corresponds to the end of the scan at 50 mm distance from the starting position. The error free curve would be a straight line with

$$\Delta x = 0{,}1 \text{ mm} \quad \text{expected straight line}$$

The mean deviation of stochastic errors DV could be determined as:

$$DV = \pm\, 0{,}004 \text{ mm}$$

The data scattering of stochastic nature was separated by trend phenomena by fitting the experimentally evident trend. This trend changes the position correlation up to 0,01 mm. Reason for the observed trend might be slow changes of the probe holder situation but also caused by features of the measured acoustic images. The value is that small that it could not be analyzed. We also assume that there is no growing error in long term since the trend is oscillating around the correct value, too.

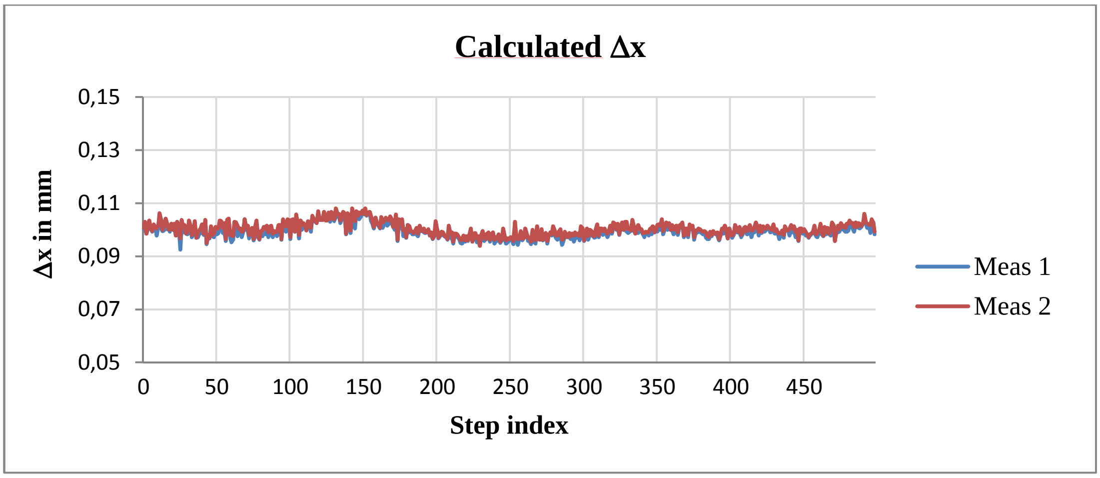

Figure 59: Accuracy and trend of indexed transducer position evaluation with step index 0,1 mm.

We have increased the scan index to 0.2 mm and 0.3 mm to understand the influence of the scan index on the achievable accuracy of transducer motion tracking. As Figure 60 and Figure 61 show, the measurement accuracy is not affected. Only minor changes can be observed within the estimated variation limits. Therefore, we may use scan index of 0.2 mm for faster scanning but with images of 0.1 mm pixel resolution.

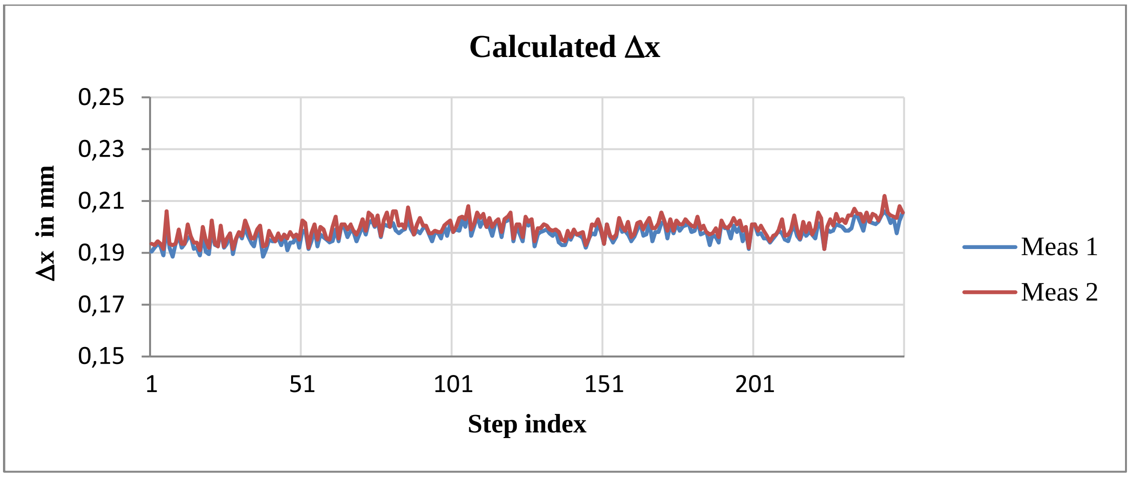

Figure 60: Accuracy and trend of indexed transducer position evaluation with step index 0.2 mm.

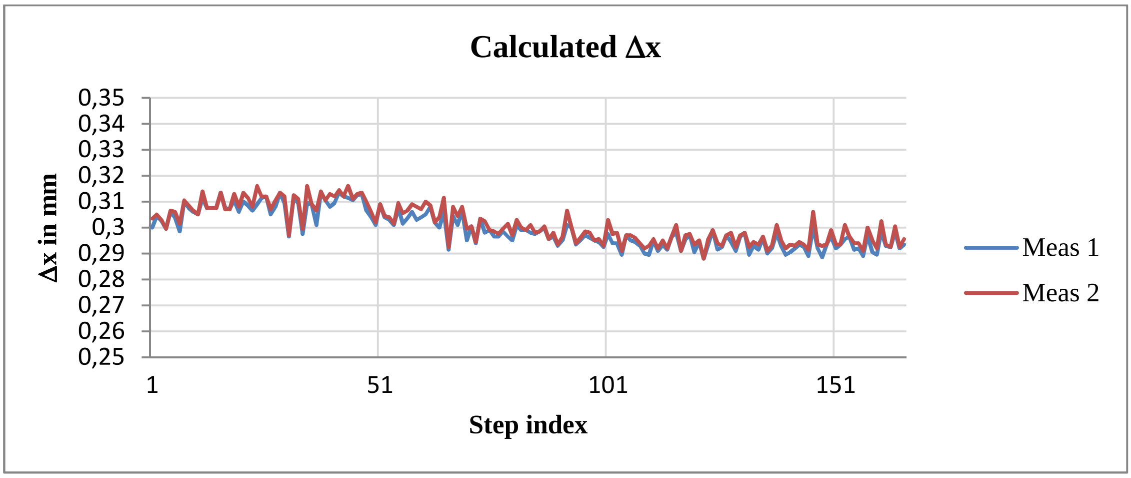

Figure 61: Accuracy and trend of indexed transducer position evaluation with step index 0.3 mm.

The influence of any long term trend can be also assessed by repeated measurements of the end position of the scan. In our experiment, the end position was at x = 50 mm. In Figure 62 we present the results of repeated measurements. All results show a systematic shorter computed scan length that is still not significant in respect to the required position accuracy of the transducer. We may explain this systematic shortening by probe holder changes during starting and ending the scan. The systematic error was taken into consideration when computing the measurement variation relative to the mean value of all results. The statistical basis corresponds to 10 measurement results taken under same conditions as described above.

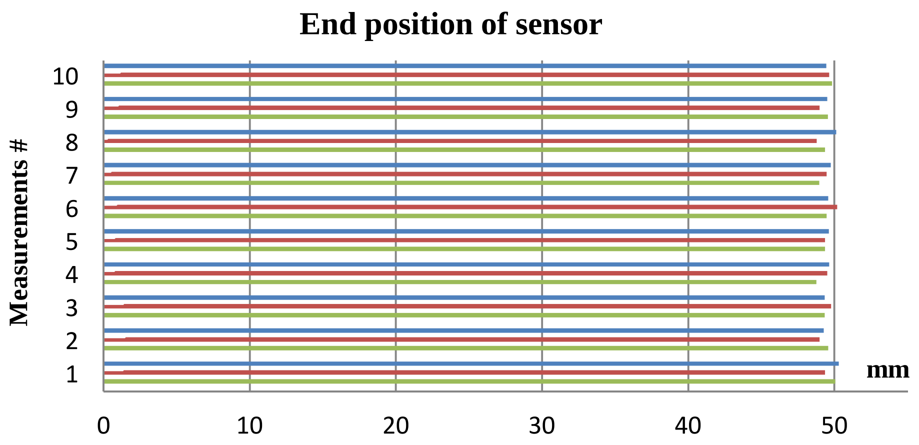

	1	2	3	4	5	6	7	8	9	10
🟦 Meas. Pos (0.1mm)	50,31	49,28	49,34	49,64	49,63	49,57	49,76	50,12	49,51	49,44
Error % (0.1mm)	1,3	1,44	1,32	0,72	0,74	0,86	0,48	0,24	0,98	1,12
🟥 Meas. Pos. (0.2mm)	49,35	48,99	49,78	49,52	49,37	50,2	49,46	48,8	48,98	49,65
Error % (0.2mm)	1,3	2,02	0,44	0,96	1,26	0,4	1,08	2,4	2,04	0,7
🟩 Meas.Pos (0.3mm)	50,07	49,59	49,34	48,76	49,37	49,46	48,96	49,37	49,56	49,84
Error % (0.3mm)	0,14	0,82	1,32	2,48	1,26	1,08	2,08	1,26	0,88	0,32

Figure 62: End Position Accuracy.

The mean value X of the measured end position is calculated as:

$$X = (49{,}47 \pm 0{,}75)\ \text{mm}$$

We may conclude: the relative position accuracy is significantly smaller than the applied half wave length. Synthetic aperture techniques can be applied also for manual scanning controlled by the optical flow analysis. The absolute error of less than 1 mm or about 1.5% of the scan length has no meaning for practical inspections.

5.3.2. Motion Tracking of Manual Scanning

However, these results are based on mechanical smooth scanning. Therefore we scanned also manually investigating the repeatability and accuracy of computed and measured scan lengths.

We used the same test block TK1 with the same scanning area for comparative motion estimation: the transducer #1 5L16-A1 was positioned and moved 50 mm by hand along the same scan as described above. All other parameter settings have been the same like the analysis window of 45mm x 25 mm in the near-field (see Figure 57). The sector scan angle was chosen from -65° to +65°; the sound velocity of the longitudinal mode was c_l = 5920mm/sec.

Image sequences have been analyzed for each computed scan index of 0.2 mm. The manual scanning speed of about 5 mm/sec was estimated. Figure 63 shows the sector scan at the end position with images of the side drilled holes 5 and 6.

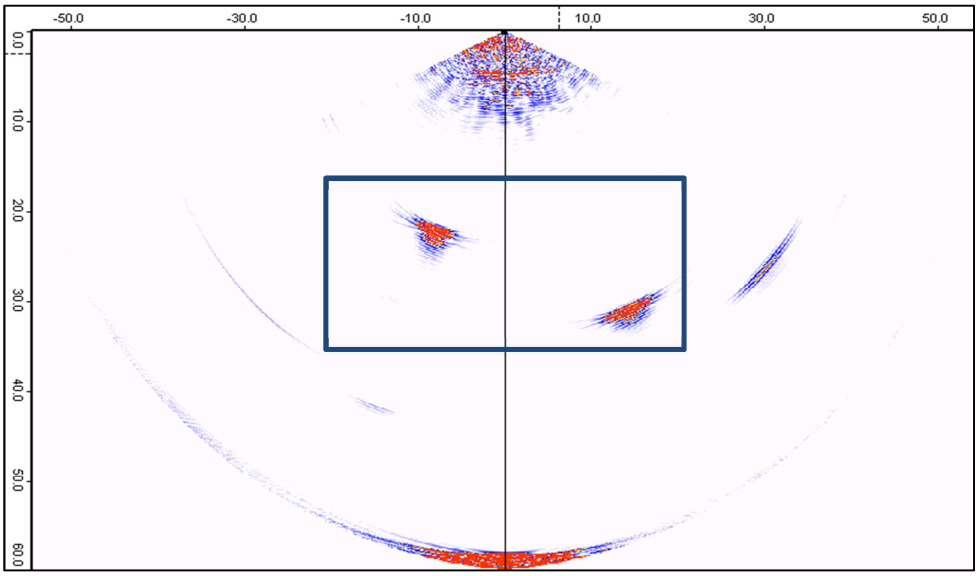

Figure 63: Manual Scanning: Sector Scan of End Position.

In Figure 64 we illustrate the visibility of transducer motion relative to the side drilled holes by an image sequence with scan distance of 0.2 mm close to this end position.

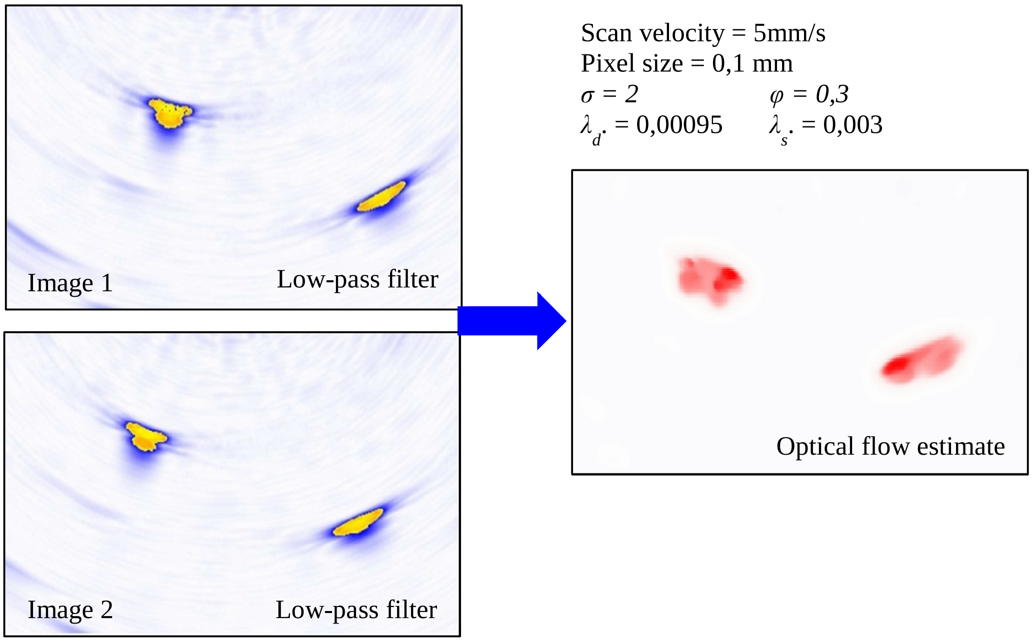

Scan velocity = 5mm/s
Pixel size = 0,1 mm
$\sigma = 2$ $\varphi = 0{,}3$
$\lambda_d. = 0{,}00095$ $\lambda_s. = 0{,}003$

Figure 64: Optical Flow Estimate during manual Scanning.

For the accuracy evaluation of end position calculation we repeated analogue to the mechanical scan ten times the manual scan. The procedure was the same as outlined above for mechanical scanning. Figure 65 contains the results of estimation.

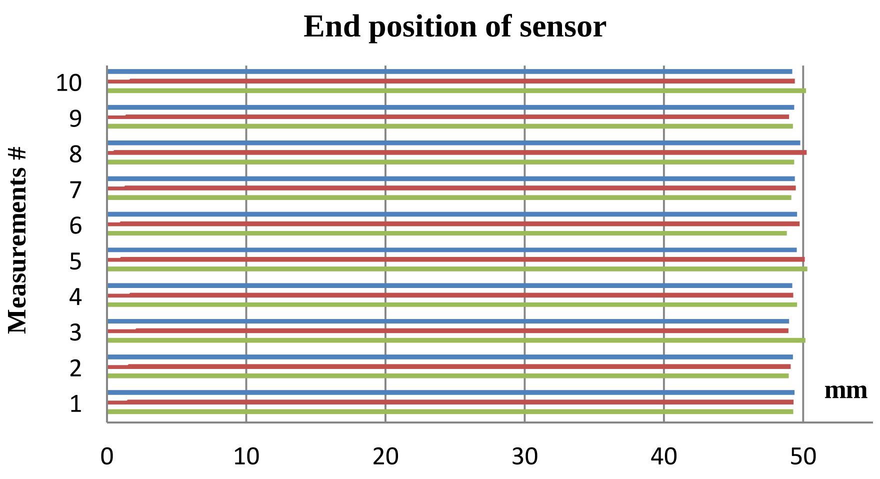

	1	2	3	4	5	6	7	8	9	10
🟦 Meas. Pos (0.1mm)	49,38	49,27	48,99	49,21	49,54	49,56	49,39	49,78	49,36	49,21
Error % (0.1mm)	1,4	1,46	2,02	1,58	0,92	0,88	1,22	0,44	1,28	1,58
🟥 Meas. Pos. (0.2mm)	49,3	49,1	48,93	49,28	50,1	49,73	49,47	50,24	48,99	49,4
Error % (0.2mm)	1,4	1,8	2,14	1,44	0,2	0,54	1,06	0,48	2,02	1,2
🟩 Meas.Pos (0.3mm)	49,28	48,96	50,15	49,56	50,3	48,83	49,15	49,34	49,26	50,2
Error % (0.3mm)	1,44	2,08	0,3	0,88	0,6	2,34	1,7	1,32	1,48	0,4

Figure 65: Accuracy of scan end position measurement (manual scanning).

The mean value X of the measured end position is calculated as:

$$X = (49{,}45 \pm 0{,}76)\ \text{mm}$$

As expected, the influence of non-constant scanning speeds and less controlled coupling is not significant. The tracking errors are within the required limits also for manual scanning. Nevertheless, we have to manage acoustic images without geometric reflectors and lift-off situations that comprise also poor, insufficient coupling.

5.4. Motion Tracking by Noise Evaluation

As discussed in chapter 1.3 the acoustic noise is not white, it contains for example information that can be used as a fingerprint for the transducer position. According to our analysis, we have to decrease that part of acoustic noise that cannot be correlated to transducer position. This part of acoustic noise is caused by microstructure grain boundary reflections for example in steel. The longitudinal mode generates much less grain boundary noise in relation to localized reflectors with interfaces of high impedance change – about one order of magnitude less than shear waves. Further, the contrast for detecting smallest reflector signal amplitudes can be improved by focusing, as discussed above. Recommended practice of coarse grain material inspection is based on the use of low frequency longitudinal transducers with sound fields focused into the region of interest. Based on this proved state-of-the-art inspection experience, we expect better tracking performance with longitudinal waves and we have to apply migration based image reconstruction with synthetic focusing into the complete synthetic near-field of the array aperture. However, we can focus only into the plane of the reconstructed sector scan; we would need matrix array transducers of sufficient large synthetic apertures to focus into space.

The experiments described below proved the expectations: shear wave sector scan sequences could not be used for transducer motion tracking as long as no reflector was imaged. However, longitudinal wave reconstructions could be used for optical flow analysis. As we assume, the possibility to estimate the optical flow of longitudinal wave sector scans is given by same order of magnitude grain boundary noise signals and reflector signals by small structural discontinuities of the steel microstructure. The optical flow estimate is also acting in some way as a filter of non-correlated image contribution.

The Figure 66 and Figure 67 received from (Kröning, 2012) show this effect: the data of a 2MHz sector scan root image of a cracked stainless steel weld have been processed by advanced stochastic filter techniques. In Figure 66, we may only identify the root indication and the crack but the image is full of noise caused by the grain structure. After filtering, the grain noise disappears but real even small reflectors appear like the crack tip indication hidden before in the noise (Figure 67).

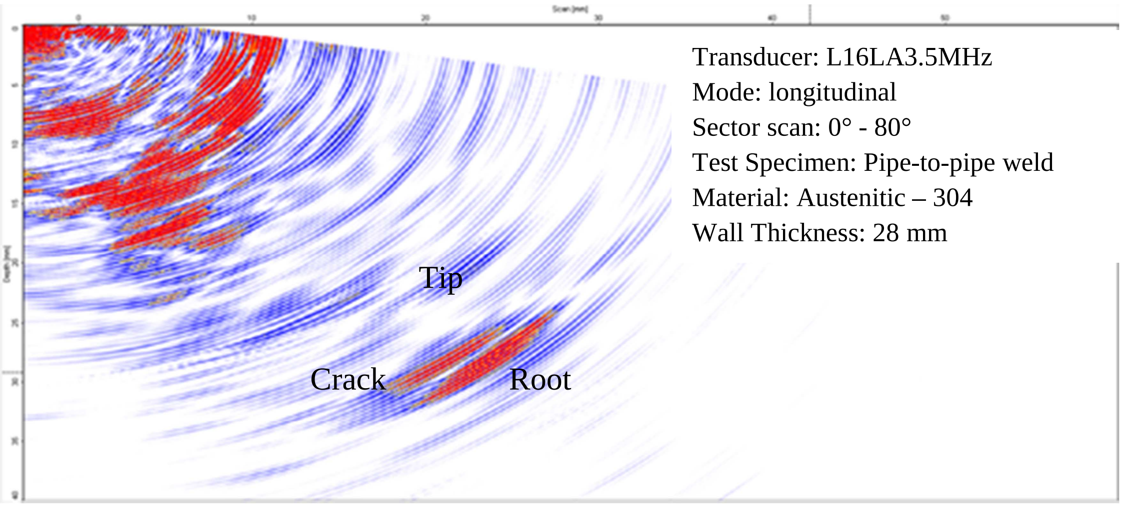

Transducer: L16LA3.5MHz
Mode: longitudinal
Sector scan: 0° - 80°
Test Specimen: Pipe-to-pipe weld
Material: Austenitic – 304
Wall Thickness: 28 mm

Figure 66: Longitudinal Migration Sector Scan of an Austenitic Pipe Weld (Dalichow, 2012).

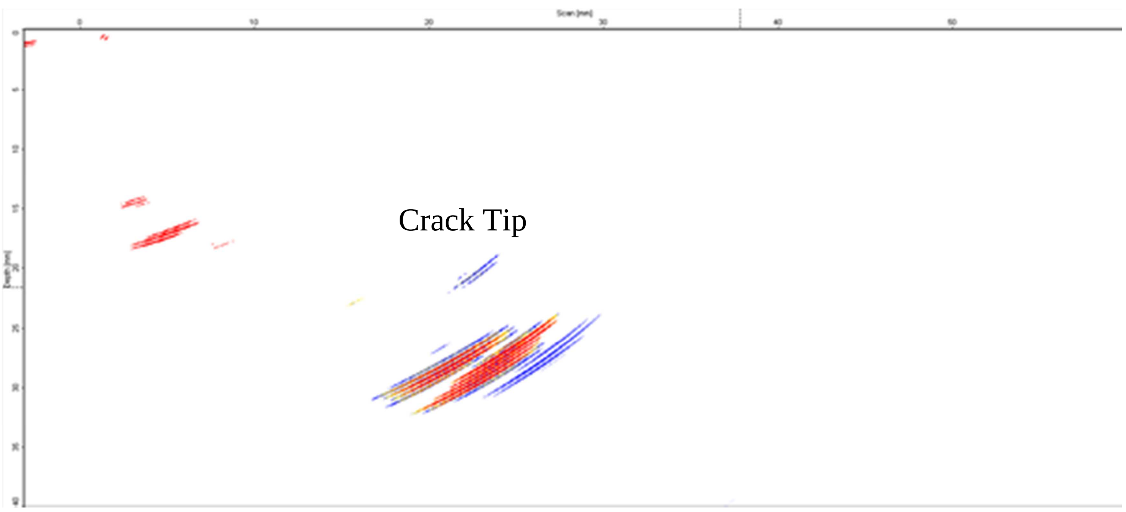

Figure 67: Sector Scan after Noise Filtering (Dalichow, 2012).

In the following we discuss transducer motion tracking by optical flow estimate of acoustic noise images. The experiments are made with the same equipment described in chapter 5.3.1. The only difference is the scanned area that was chosen on a position of test specimen TK 2 up to the position of the crack. The length of the scan was 70 mm, the scan index 0.5 mm. The analysis the same window size was experiment with side drilled holes.

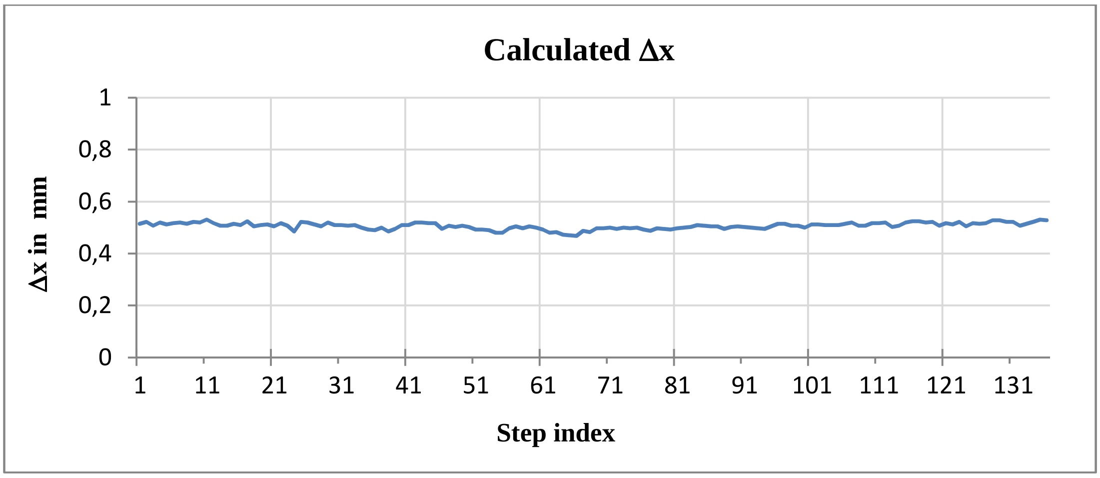

Figure 68: Accuracy of Scan Index Estimates during Automated Scanning.

We computed the optical flow for all consecutive image pairs. Since the scan was made by precision manipulator we could compare the encoder position data with the computed data as shown in Figure 68. Figure 68 indicates the errors or differences for each scanner step of a length of 0.5 mm. Perfect results without any measurement or algorithmic error would be represented by a straight line with Δx = 0.5 mm.

As it can be seen, the accuracy of measurement is about the same we could achieve with reflector images even when we have no clear picture about the nature of the optical flow image. A typical optical flow field of this experiment is shown in Figure 69.

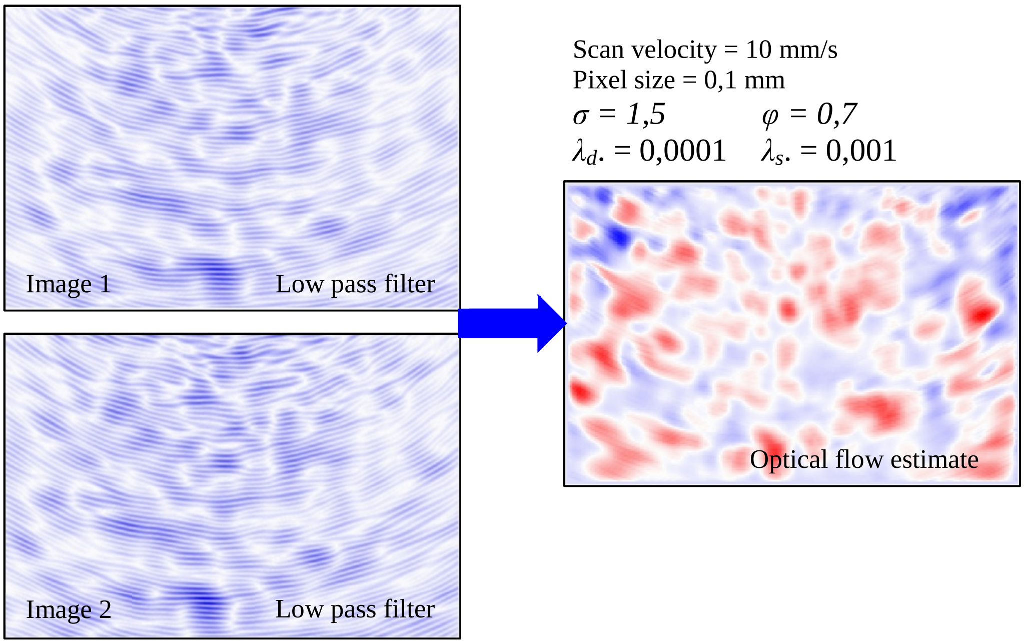

Scan velocity = 10 mm/s
Pixel size = 0,1 mm
$\sigma = 1{,}5$ $\varphi = 0{,}7$
$\lambda_d. = 0{,}0001$ $\lambda_s. = 0{,}001$

Figure 69: Optical Flow Field Estimate for Window Pairs with Acoustic Noise (Longitudinal Mode).

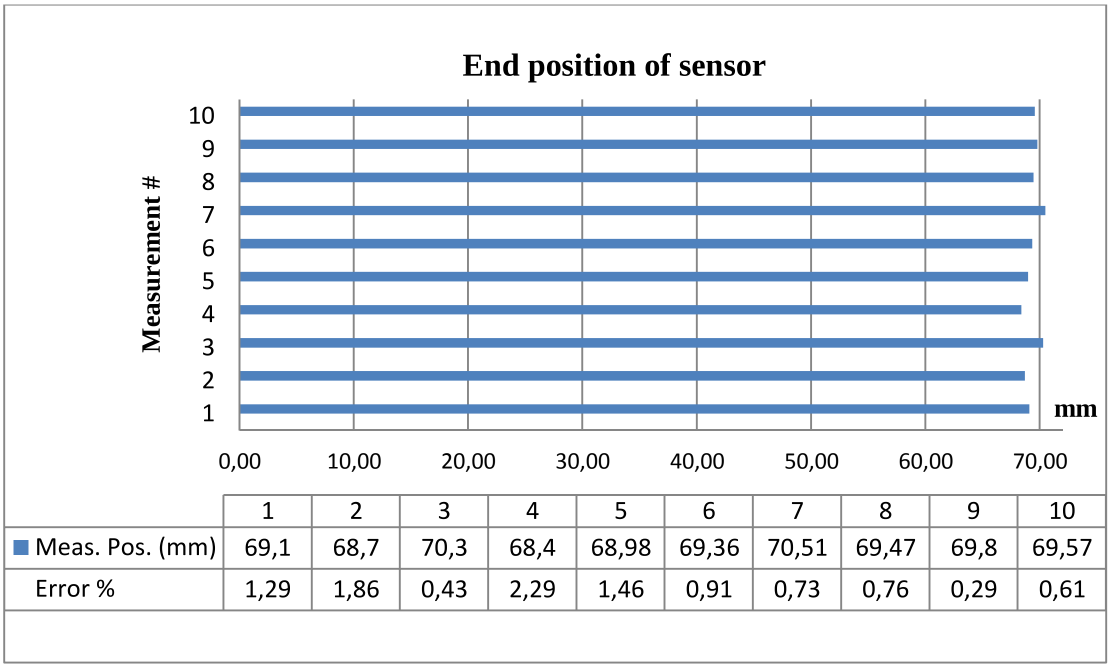

	1	2	3	4	5	6	7	8	9	10
■ Meas. Pos. (mm)	69,1	68,7	70,3	68,4	68,98	69,36	70,51	69,47	69,8	69,57
Error %	1,29	1,86	0,43	2,29	1,46	0,91	0,73	0,76	0,29	0,61

Figure 70: Variations of End Position Measurement (Noise Images).

We analyzed also the accuracy of end position measurement according to the procedure discussed in chapter 5.3.1 and 5.3.2. Results are given by Figure 70. The mean value and the mean deviation of end position data are:

$$X = (69.42 \pm 0.63)\ \text{mm}$$

This result is confirming the principle viability of transducer motion tracking by acoustic image sequences containing only noise. Certainly, we have still to continue with systematic investigations on different steel grades as an engineering task but we believe also in the further development of matrix arrays with better focusing in space. We expect that the grain boundary noise contribution can be decreased further by about one order of magnitude with simultaneously increased contrast for real local spot reflectors.

5.5. Lift-off Experiment

During automated scanning, the transducer is in continuous contact with the surface. Any loss of coupling or transducer lift-off can be monitored and considered during data evaluation. However, during manual scanning, the inspector has to remove the sensor from the surface occasionally when poor coupling is noticed or when he wants to repeat measurements of specific interest in more detail. Consequently, the “self-tracker” equipment has to identify the previous transducer position to continue the measurement and to select relevant A-scan data for best scanning performance.

The “lift-off” experiment established the accuracy of identifying previous transducer position after lift-off; the same experimental setup was used. The new input images are correlated to existing images stored in a pipeline. While scanning about 50 mm, we found two corresponding transducer positions within approximately 3 seconds. This allows the inspector to perform manual scanning as usual. The accuracy of repositioning by corresponding acoustic images is in the range of about +/- 0.5 mm or roughly half the wavelength.

For the lift-off experiment, we implemented a sub-module that controls the coupling quality and enables the inspector to place the transducer on a previously scanned position on the specimen surface. The scheme of this process is described in Figure 71.

Firstly, we have to implement a coupling-decoupling detection module. Depending on the transducer used, we have to select the appropriate coupling detection method. The best way to detect coupling quality is the analysis of the back-wall A-scan indication imaged by the sector scan for most of the inspection problems. This is simply done by choosing a monitoring window and a threshold. The coupling is considered to be good if the A-scan amplitude exceeds the threshold value. In case the component back-wall is not part of the inspected volume or there is no back wall at all with reflector signals of constant amplitude, we may identify other methods for coupling monitoring. One method applicable for almost all inspection geometries is the monitoring of the coupling noise. This method asks for more computing and calibration efforts since we have to analyze the statistics of near surface noise as a function of the applied transducer and the surface quality. Here we limit our experiments on the back-wall reference method.

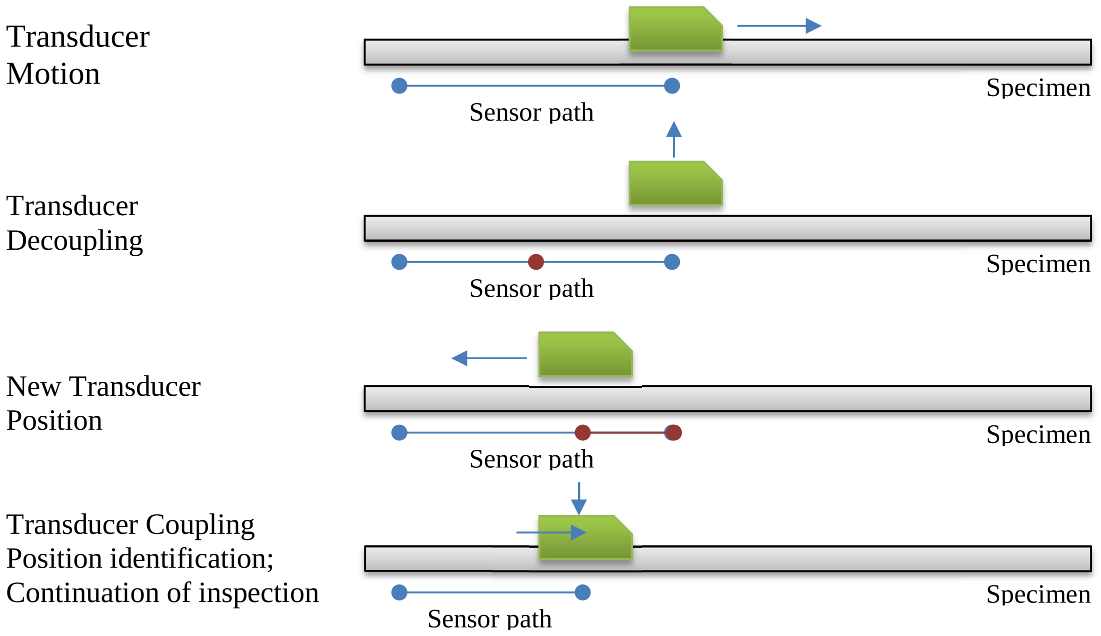

Figure 71: Scheme of the lift-off experiment.

The first step comprises the calibration of the amplitude threshold for the specific transducer and component geometry. In our experiment, the test specimen is a plate with constant wall thickness with the advantage that the back wall signal amplitude should be constant around a defined mean value with a certain mean deviation indicating accepted coupling variations. For some materials we may notice additional variations by local attenuation changes that can be considered by component related calibration. By setting an appropriate time-of-flight gate with the calibrated lowest accepted amplitude as a threshold, the system can identify loss of coupling.

As mentioned above, for some inspection problems we would have to analyze the coupling noise. Here we outline only the principal viability of this approach. Figure 72 shows two A- scans, one for good coupling, the other one for poor coupling contact. The set time-of-flight gate points to the signal change of the near surface zone known also as dead zone. In our example, the gate covers the depth zone between 3 mm and 7 mm. The signals have been measured for the 5 MHz transducer #1 of Table 4 on test block TK1. The nature of signal variations is rather stochastic due to the complex phenomena of wave field interaction at the surface-transducer wedge interface. Further, a complete loss of coupling might change also the statistics of near surface signals. This procedure is already applied for automated inspections and part of service companies' know-how (Engl, 2011).

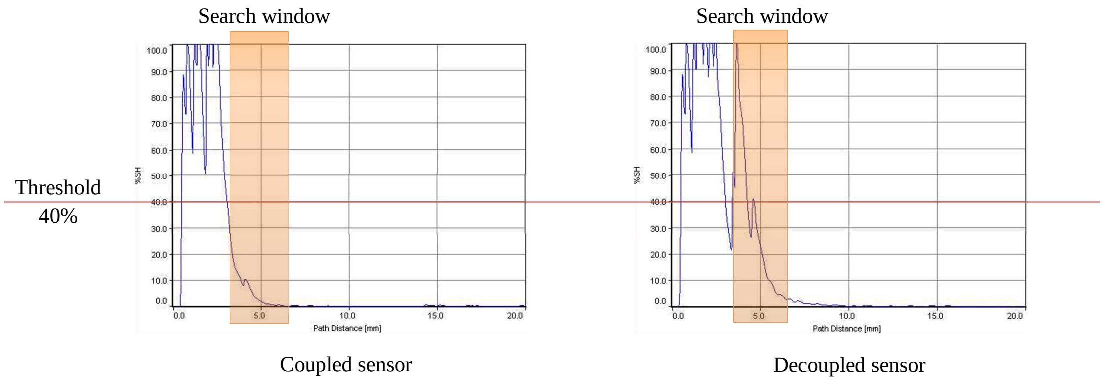

Figure 72: Coupling Control by Near Surface Signal Analysis.

The second step is the repositioning. After lift-off and regaining a good coupling we have to identify the actual transducer position. The actual processed acoustic image will be compared with previously measured valid images stored in a small databank. The data bank is filled with intermediate sector scans representing the last scanned surface area. The interval between stored positions (here called scan index for repositioning) can be also parameterized. It should be set in such a way that the overlap of two consecutive sector scans is not less than 50%. The size of the area with intermediate data stored for repositioning can be defined by the operator. By default, it is set to be 100% of the scanned area.

After discovering poor coupling, both the last measured valid sector scan and its position are stored in an array of check points. With this information, the algorithm waits for re-coupling. When good coupling is regained and a sector scan for this unknown position is available, the correct transducer position has to be determined in relation to the previously measured positions. This can be achieved by applying cross-correlation methods between the last sector scan and the stored sector scans. Cross-correlation is convolution-based and has the following analytical form:

$$(f * g)(x) \coloneqq \int f(x - x')\, g(x')\, dx' \qquad 5.5\text{-}1$$

f and *g* are symbolizing input sector scans, * is a convolution operator.

We can write 5.5-1 for two dimensions:

$$(f * w)(x, y) \coloneqq \iint_{-\infty}^{\infty} f(x - x', y - y')\, g(x', y')\, dx' dy' \qquad 5.5\text{-}2$$

Image based cross-correlation algorithm is also known as phase correlation and usually performed in the frequency domain. In the frequency domain convolution is simply a multiplication, i.e. FFT-2D and IFFT-2D are calculated according to:

$$\mathcal{F}[\mathrm{f} * \mathrm{g}] = \mathcal{F}[\mathrm{f}] \cdot \mathcal{F}[\mathrm{g}] \qquad 5.5\text{-}3$$

where $\mathcal{F}$ is a Fourier transformation operator.

In image processing, phase correlation is a method of image registration. It uses a fast frequency-domain approach to estimate the relative translative offset between two similar images (Wikipedia, 2012).

After obtaining the result R we have to perform an inverse Fourier transform:

$$R = \mathcal{F}[f * g]; \qquad r = \mathcal{F}^{-1}[R] \qquad 5.5\text{-}4$$

The last step would be the determination of the maximum value for each of the scan pairs. Phase-correlation of two input images returns an image that contains peaks at positions where the second image is similar to the first one: the peak amplitude relates to the grade of similarity. Applying phase-correlation to sector scans, enforcing a goodness threshold to the correlation and summing up all values, one obtains a numeric similarity number for each stored sector scan. Selecting the maximal value, one obtains the most probable sector scan and its position, thus determining the actual position of the transducer. If none (or less than three sector scans) exceed the set threshold, a negative answer will be generated: the actual transducer position is not found, the transducer was moved to a position outside the scanned area with stored data. In this case the inspector may reposition the transducer and repeat the test or he may set a new position input with correct coordinate values and continue the inspection.

We have tested the viability of the outlined image similarity correlation including the developed code by experiment. We used the test specimen TK1 with side drilled holes. We scanned the surface by manipulator to get the immediate feedback of the real transducer position to be compared with the found one by correlation after lift-off. The constant scanning speed was 5 mm/sec, the scan length with two lift-offs was 100 mm, the scan index 0.2 mm. After each lift-off, the scanner was moved backwards onto the already scanned area. In Figure 73 some of the results of the lift-off experiments are shown.

In this figure, the plotted green line represents the transducer position data provided by the scanner, the red line informs about the calculated values. During motion tracking, several sector scans were also stored with their position data as “check point positions”. These positions are marked by blue balls in the figure.

Lift-offs and position search intervals are highlighted by colored bars. Lift-off and repositioning of the transducer were programmed to be performed in 2 seconds. Position search was performed within 3 seconds. This time is usually enough for searching through 100 sector scans. However, time depends on sector scan resolution, its size and on the processor clock speed.

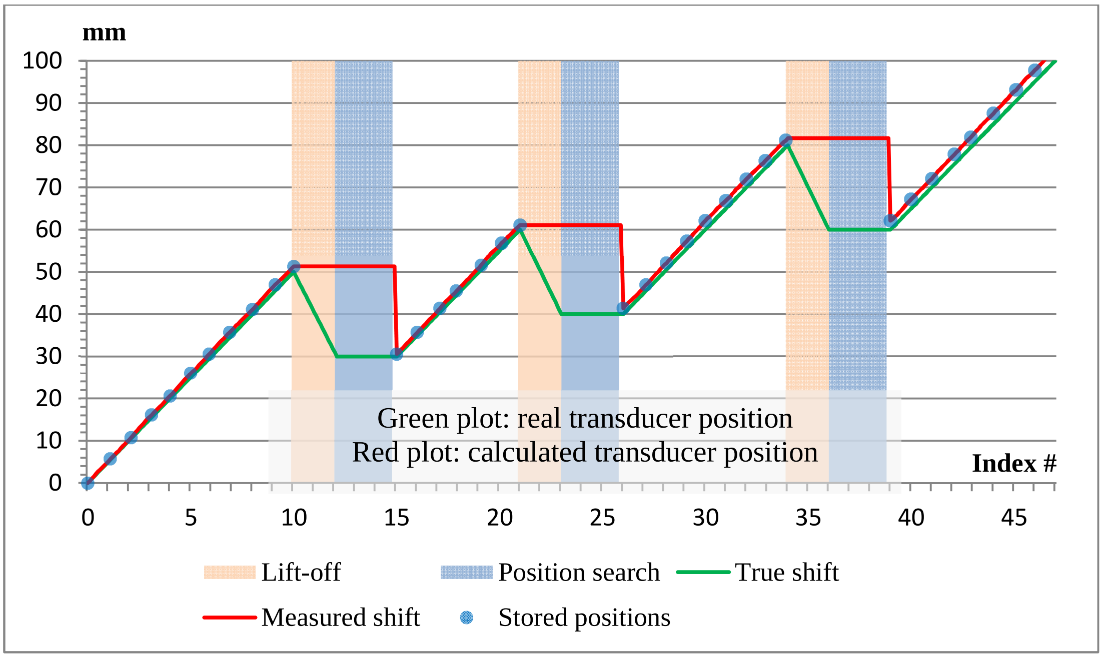

Figure 73: Quantitative representation of the lift-off experiment.

In Figure 74 we compare the transducer position, taken from the manipulator encoder, with the values calculated by the optical flow algorithm. During lift-off and position searching the position error is set to zero.

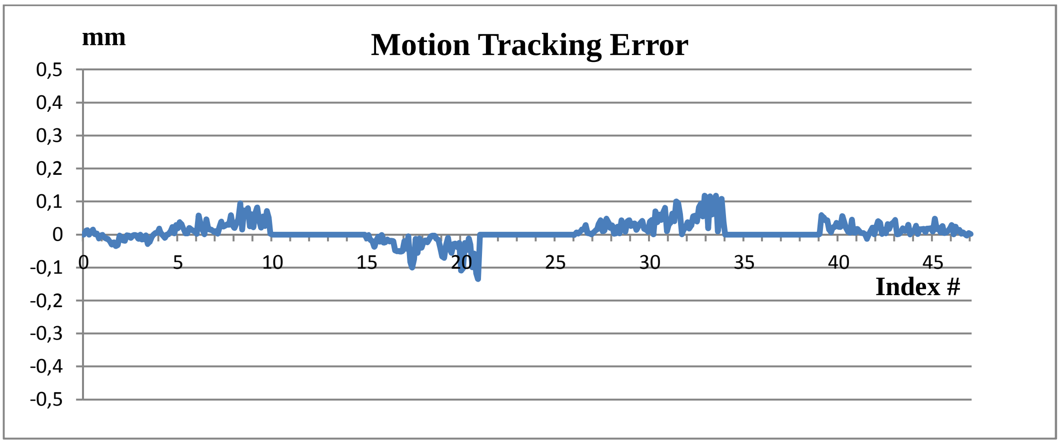

Figure 74: Transducer Motion Tracking Error.

Unfortunately, the developed algorithm is not robust in respect to the required content of acoustic images. The state of development limits its application to images of real reflectors. Imaging of acoustic noise patterns that may include real reflectors of low amplitude will not provide the necessary contrast for image correlation as described. However, the developed algorithm can be applied successfully when reflectors are imaged. The error of repositioning is in the range of 5-10 % of the storage increment size depending on the image contrast, the coupling quality and the scanning speed.

We suggest progress by improving the spatial image resolution by 3D spatial focusing. 3D synthetic focusing by matrix arrays will reduce the contribution of acoustic grain boundary noise significantly. As a result, we may image real reflectors that can be correlated by optical flow evaluation to the transducer position. However, matrix arrays with large apertures are not available until today.

Nevertheless, the “check point positions” help to overcome this problem just by interpolation of scanned positions since we have not to image any reflector for this part of scan.

The “lift-off” experiment proved the achievable accuracy of identifying previous transducer position after transducer lift-off. The reasonably short time of 2-3 seconds needed for the position identification allows the inspector to perform manual scanning as usual. The positioning accuracy of corresponding measurements is in the range of about +/- 0.5 mm or roughly half the wavelength.

Chapter 6. Conclusion and Outlook

We could prove the ultrasonic transducer tracking concept by optical flow estimate of acoustic image sequences measured during scanning. The technical realization of this self-tracker or *“Acoustic Mouse”* principle will enable the future use of manual testing of components when automated standards are required. The achievable accuracy of transducer position calculation is good even for synthetic aperture scans that require a precise relative position measurement better than half of the applied wave length. We could demonstrate that acoustic noise images can be analyzed with an accuracy of transducer position measurement of same order when we apply longitudinal waves less sensitive to grain boundary noise.

The *“Acoustic Mouse”* has become a viable technology by taking advantage of advanced ultrasonic array techniques with real-time migration for high resolved and high contrast reflector imaging. The image reconstruction is position controlled similar to SAFT measurements. We could measure sector scan images in real-time with synthetic focusing and noise filtering algorithms that enabled fast image sequences of required quality for optical flow analysis.

Until now, we are limited to linear scans. For manual scanning on component surfaces we would need 3D images for position measurement on the surface including information about transducer “swiveling”. 2D images gained by linear arrays would pose an ill problem. There are numerical approaches for adequate solvers of this type of ill-posed problem but the algorithmic complexity would not allow a practical real-time solution during scanning.

However, we may expect first matrix arrays for 3D imaging in the next future that will help to develop more general solutions for the *“Acoustic Mouse”* needed for practical manual testing. Applying migration to matrix array A-scan data we focus into 3D with further reduction of grain boundary noise and increase of signal amplitude of local reflectors. As a result of 3D focusing we assume that we can also track transducer motion when applying shear waves.

Following the trend in computing and IT we believe that already in the near future standards will be made available that speed up the computing time for scanning velocities up to 500 mm/sec. We need small computer units since we want to integrate the *“Acoustic Mouse”* into portable instruments for manual testing.

Appendix A

Elastodynamic equations

Elastic vibrations in liquids and gases are characterized by change of pressure p, particle displacement from its equilibrium position u, rate of vibrational motion v, displacement potential χ, and particle velocity φ. All these parameters are interrelated by the equations:

$$u = grad\ \chi\,,\ \mathrm{v} = grad\ \varphi,\ \mathrm{v} = \frac{du}{dt}\,,\ p = \frac{\rho\partial\varphi}{dt}, \qquad \text{A1-1}$$

where ρ is density of mass, and t is time.

Acoustic phenomena in solids are much more complex than in liquids and gases due to the shear elasticity of solids. Instead of the term pressure for liquids we use the notation stress

$$\sigma = \frac{F}{A} \qquad \text{A1-2}$$

i.e. the force F acting on an area A for solids. There are compressive and tensile stress states $\sigma_{xx}, \sigma_{yy}, \sigma_{zz}$, and shear stress states σ_{xy}, σ_{yz} etc. The stress state of solids is characterized by the third-rank tensor σ_{ij}, where i, j take the values of the coordinate axes x, y, z. This tensor is symmetric, i.e. $\sigma_{ij} = \sigma_{ji}$. Fluctuations in solids are characterized by changing stress σ_{ij}, particle displacement u_i and displacement potential. The notation "particle velocity" is not widely used; more common is the term "deformation" for fluctuations in solids. The deformation is expressed by the displacement field of the material. It can be written as strain tensor ε_{ij}, similar to stress tensor:

$$\varepsilon_{xx} = \frac{du_x}{dx} \qquad \text{A1-3}$$

is for example the deformation along the axis x. For symmetric strain tensors the quantity ε_{xy} can be written as:

$$\varepsilon_{xy} = \left(\frac{\partial u_x}{\partial u_y} + \frac{\partial u_y}{\partial x}\right) / \, 2 \qquad \text{A1-4}$$

Similar relations hold for other values of ε_{ij}.

We consider only isotropic acoustic media. In isotropic media the sound velocities are independent from the propagation direction.

The relation between stress and strain is called Hooke´s law. In general notation, it is written as:

$$\sigma_{ij} = \delta_{ij} \mathit{\Lambda} \varepsilon_{ii} + 2\mu\varepsilon_{ij} \qquad \text{A1-5}$$

with $\delta_{ij} = 1$, when $i = j$; and $\delta_{ij} = 0$, when $i \neq j$; $\mathit{\Lambda}$ and μ are the Lamé constants.

In material science Young’s modulus E and Shear modulus G are commonly used:

$$E = \frac{\mu(3\mathit{\Lambda} + 2\mu)}{\mathit{\Lambda} + \mu}; \qquad G = \mu \qquad \text{A1-6}$$

Another important elastic constant, the Poisson’s ratio is defined as:

$$v = \frac{\mathit{\Lambda}}{2(\mathit{\Lambda} + \mu)} = \frac{E}{2G} - 1 \qquad \text{A1-7}$$

The elastic properties of isotropic media are characterized by independent elastic constants.

The wave equation for solids is set up by applying Newton’s second law to the elementary volume dx, dy, dz. We obtain the following equation for axis x:

$$\rho\frac{\partial^2 u_x}{\partial t^2} = \frac{\partial \sigma_{xx}}{\partial x} + \frac{\partial \sigma_{xy}}{\partial y} + \frac{\partial \sigma_{xz}}{\partial z} \qquad \text{A1-8}$$

Similar equation can be formed for y and z; substituting them into equation (A1-5), we obtain the wave equation for elastic media:

$$\rho\frac{\partial^2 u_x}{\partial t^2} - (\mathit{\Lambda} + \mu)\frac{\partial \varepsilon}{\partial x} - \mu\nabla^2 u_x = 0 \qquad \text{A1-9}$$

with the Laplace operator

$$\nabla^2 = \frac{\partial^2}{\partial x^2} + \frac{\partial^2}{\partial y^2} + \frac{\partial^2}{\partial z^2} \qquad \text{A1-10}$$

In matrix-vector notation the wave equation can be written:

$$\rho \frac{\partial^2 u}{\partial t^2} = (\Lambda + \mu) grad\ div\ u + \mu \nabla^2 u \qquad \text{A1-11}$$

For $\mu = 0$, and equal particle displacements $u_x = u_y = u_z = u$ for every direction (scalar), we obtain the wave equation for gas and liquids:

$$\frac{\partial^2 u}{\partial t^2} = c^2 \nabla^2 u \qquad \text{A1-12}$$

with the ultrasonic wave velocity:

$$c = \sqrt{\Lambda / \rho} \qquad \text{A1-13}$$

Two modes of volume waves exist in solid media propagating at different velocity. We can proof it with the help of equations (A1-9) and (A1-11). Any vector can be presented as a sum of the scalar potential φ and the vector potential Ψ:

$$u = u_l + u_t = grad \varphi + curl \Psi \qquad \text{A1-14}$$

Substituting (A1-14) into (A1-11) taking into account:

$$curl\ u_l = 0; \quad div\ u_t = 0, \qquad \text{A1-15}$$

we obtain the following equitation:

$$\frac{\partial^2 u_l}{\partial t^2} - c_l^2 \nabla^2 u_l = 0 \qquad \text{A1-16}$$

with $$c_l = \sqrt{\frac{(\Lambda + 2\mu)}{\rho}} = \sqrt{\frac{E(1-v)}{\rho(1+v)(1-2v)}}$$

and

$$\frac{\partial^2 u_t}{\partial t^2} - c_t^2 \nabla^2 u_t = 0 \qquad \text{A1-17}$$

with $$c_t = \sqrt{\frac{\mu}{\rho}} = \sqrt{\frac{E}{2\rho(1+v)}}$$

Equations (A1-16) and (A1-17) are the wave equations for the two wave modes with the velocities c_l and c_t (Aleshin, 1989), (Ermolov, 1991).

Appendix B

Parameter calibration

As described above the result of optical flow estimate depends on various parameters that are specific or the image type. The parameters have to be set for each iteration step but will not be changed during the complete measurement. A strict balance of all parameter values leads to a more robust and correct solution of the energy functional and in consequence to a more precise shift calculation. Calibrating these parameters for the specific acoustic images of the inspection problem enables the presetting of algorithm arguments for different material types, transducers, and noise characteristics. The parameters established can be used further for analogue inspection problems.

The following parameters have to be determined by experiments:

1. Gaussian Blur parameter σ.
2. Weighting parameter φ of the energy functional.
3. Data term robustness parameter λ_d.
4. Smoothness term diffusivity parameter λ_s.

The first parameter σ is by type a standard deviation parameter described in formulation 4.3-6:

$$I_i^{\sigma} = K_{\sigma} * I_i$$

This parameter effects the pre-smoothing of input images. Its maximum preset value of 3 covers almost 99 % of the whole Gaussian function area with similar results if the entire Gaussian distribution would have been applied. Typical σ preset values usually lie in the interval of $(0, 3)$. The more we blur the input images, the less detailed and less noisy are the images to be processed for optical flow calculation. If we blur too much, we attenuate too many details together with the noise. As an experienced based rule, we may set σ values between (0.5; 2) for acoustic images without any geometric reflector when we have to analyze the noise pattern, respectively between (1.5; 3) for input images with visible reflectors.

The second parameter φ is a weighting parameter between the data term and the smoothness term in energy functional formulation. It defines the dominance of the smoothness term over the data term. Setting this value to 0 we cancel the effect of the smoothness term and the result becomes very sharp and noisy with a lot of artifacts. For bigger values of φ we obtain smoother solutions but attenuating more details. In our experimental part we have chosen the value interval (0.1; 1.2). The recommended way of using this parameter is to decrease its value with the iteration process imitating a coarse to fine strategy. However, this leads to algorithm complexities and the overall running time efficiency will slow down: as a drawback of this strategy one has to recalibrate other parameters after changing the weighting parameter φ. For that reason, we use a constant value taken from the before mentioned interval for the whole iteration process.

The third and the fourth parameter are the data term robustness parameter λ_d and the smoothness term diffusivity control parameter λ_s. These parameters represent the contrast parameter λ of the diffusivity function Ψ mentioned in the energy functional formulation (4.3-17). In this thesis we set $\lambda_s < \lambda_d$. Both parameters lie in the interval (0.003; 0.5). Applying this parameter with the value chosen from the left side of the interval will lead to sharper edges and flat blurred surfaces. This process is a nonlinear diffusion filtering that blurs the flat areas of the input images and brings higher contrast to the edges. Too small values of λ lead to a lot of artifacts. For larger values the diffusivity function Ψ (its first derivative) tends to become a linear diffusion filter that can be described by Tychonoff diffusivity function $\Psi(s^2) = s^2$.

Glossary

Symbols

ρ	medium density
E	Young’s modulus
G	Shear modulus
v	Poisson’s ratio
c	velocity of ultrasonic wave
Θ	phase angle
φ	group angle
α_G	geometric attenuation
α_A	the attenuation due to absorption
α_S	attenuation due to scattering
S_{ij}	elastic constant, elastic compliances
∇	gradient operator
∇^2 or Δ	Laplace operator
g	anisotropy factor
Λ	Lamé constant
μ	Lamé constant
V	volume of the scatterers
d	grain size
N	series number

$\boldsymbol{\Psi}$	vector potential
G	number of grains
R_{nf}	near field distance
A	aperture
λ	wavelength
ϑ	focus diameter
f	frequency
Z	acoustic impedance
R	refraction coefficient
C_{ph}	phase velocity
C_{ij}	elastic constant, elastic stiffnesses
$\boldsymbol{\Phi}$	fiber orientation
C	group velocity
α	attenuation coefficient
α_D	attenuation coefficient for diffusion scattering
α_p	attenuation coefficient for stochastic or phase scattering
α_r	attenuation coefficient for Rayleigh scattering
d_r	distance to the reflector
α_h, α_t	absorption losses
$A_{i,j}$	information matrix
I_0	initial intensity
x	distance of wave propagation
I_1, I_2	input image pair
(u, v)	image coordinates
$z(u, v)$	solution function
$E(z(u, v))$	energy functional

Ω	image domain
σ	standard deviation parameter
K_σ	Gaussian convolution kernel
λ_d	data term regularizer
λ_s	smoothness term regularizer
div	divergence operator
g_{Ch}	Charbonier diffusivity function
sgn	sign function

Acronyms

FF	Far-Field, Fraunhofer zone
NF	Fresnel zone, Near-Field
F	Beam Focus
D	Beam Spread
QNDT	Quantitative Nondestructive Testing
NDT	Nondestructive Testing
QUT	Quantitative Ultrasonic Testing
FM	Fracture Mechanic
AM	Acoustic Mouse
SAFT	Synthetic Aperture Focus Technique
UT	Ultrasonic Testing
RF	Repetition Frequency
SDH	Side Drilled Hole
FBH	Flat Bottom Hole
PC	Personal Computer
PA	Phased Array
EMAT	ElectroMagnetic Acoustic Transducer

NPP	Nuclear Power Plant
FAD	Failure Assessment Diagram
PoD	Probability of Detection
A-Scan	One-dimensional display of ultrasonic signal amplitude as function of time.
B-Scan	Two-dimensional view of cross sectional plane through the test object.
C-Scan	Image of the results of an ultrasonic examination showing a cross-section of the test object parallel to the scanning surface.
D-Scan	Image of the results of an ultrasonic examination showing a cross-section of the test object perpendicular to the scanning surface and perpendicular to the projection of the beam axis on the scanning surface.

Bibliography

Achenbach, J. D. 2000. Quantitative nondestructive evaluation. *International Journal of Solids and Structures.* 2000, Vol. Vol. 37, Issues 1-2.

Aires, K.R.T., Santana, A.M., Medeiros, A.A.D. 2008. *Optical Flow Using Coöour Information.* New York : ACM, 2008. 978-1-59593.

Aleshin, N.P., Belyi, B.E., Vopilkin, A.H. 1989. *The methods of acoustical testing for metalls.* Moscow : Mashostroenie, 1989.

Altman, C., Such, K. 1991. *Reciprocity, Spatial Mapping and Time Reversal in Electromagnetics.* Dordrecht : Kluwer, 1991.

Alvarez, L., Deriche, R., S'anchez, J., Weickert, J. 2002. Dense disparity map estimation respecting image derivatives: a PDE and scale-space based approach. 2002, pp. 13(1/2):3–21.

ANSI. 2001. *ANSI/ASNT CP-189, Standart for Qualification and Certification of Nondestructive Testing Personnel.* s.l. : American Society for Nondestructive Testing, 2001.

Arnold, W. 2008. Ultrasound Absorption in Solids. [book auth.] M.L. Munial, M. Vorländer, P. Költzsch, M. Ochmann, A. Cummings, W. Maysenhölder, W. Arnold F. P. Mechel. *Formulas in Acoustics.* Berlin, New York : Springer, 2008.

ASME. 2010. *ASME Boiler and Pressure Vessel Code, Section V: Nondestructive Testing.* s.l. : American Society of Mechanical Engineers, 2010. 978079832486.

—. 2001. *ASME Boiler and Pressure Vessel Code, Section XI: Rules for Inservice Inspection of Nuclear Power Components.* New York : ASME International, 2001.

ASNT. *NDT Handbook Vol. 7, Ultrasonic Testing.* Columbus, OH, USA : The American Society for Nondestructive Testing.

Atomgesetz. 1959. *Gesetz über die friedliche Verwendung der Kernenergie und den Schutz gegen ihre Gefahren.* s.l. : www.juris.de, 1959.

Baldev Raj, T. Jayakumar, M.Thavasimuthu. 2007. *Practical Nondestructive testing.* s.l. : Narosa Publishing House Pvt. Ltd, 2007.

Barron, J., Fleet, D., Beauchemin, S. 1994. *Performance of optical flow techniques.* 1994. pp. 43–77.

Bernus, L., Kröning, M., Boulavinov, A., Reddy, K.,Yastrebova, O., Kudalkar, V. 2006. *Verfahren zur ortsaufgelösten, zerstörungsfreien Werkstückuntersuchung. DE 102006027182A1* 2006.

Bertovic, M., Gaal, M., Müller, C. *Investigating human factors in manual ultrasonic testing: testing the human factor model.* s.l. : 4th European-American workshop on reliability of NDE.

Biondi, B. 2006. *Three Dimensional Seismic Imaging.* s.l. : Society of Exploration Geophysicists, 2006. 0-07-011117-0.

Black, M. J., Anandan, P. 1991. Robust dynamic motion estimation over time. Maui, HI : IEEE Computer Society Press, 1991, pp. 292–302.

Bleistein, N., Cohen, J., Stockwell J. Jr. 2001. *Mathematics of Multidimensional Seismic Imaging, Migration, and Inversion.* New York : Springer, 2001.

BMU, Nuclear Safety in Germany. 1999. *Report under the Convention on Nuclear Safety by the Government of the Federal Republic of Germany.* s.l. : http://www.bmu.de, 1999.

Boehm, R., Brackrock, D., Kitze, J., Brekow, G., Kreutzbruck, M. 2009. Saft for Crack Surface Analysis - Comparison of Modeling and Phased Array Measurements. *5th International Workshop of NDT Experts, 12-14 Oct 2009, Prague.* 2009.

Boehm, R., Hauser, T., le Gal, P., Rotter, B., Bleck, A., Hesselmann, W. 1992. Richtungsabhängigkeit der Schallgeschwindigkeit in austenitischen Plattierungen. *Fortschrittsberichte der Jahrestagung 1992 der deutschen Gesellschaft für zerstörungsfreie Prüfung.* 1992, Vol. Bericht 33.2.

Bolotina, I., Dennis, M., Mohr, F., Kröning, M., Reddy, K. M., Zhantlessov, Y. 2012. 3-D Ultrasonic Imaging by Cone-Scans and Acoustic Antennas. *Proceedings of the 18th World Conference on Nondestructive Testing, Durban, SA.* 2012.

Bolotina, I., Kröning, M., Mohr, F., Reddy, K. M., Soldatov, A., Zhantlessov, Y. 2012. Ultrasonic Arrays for Quantitative Nondestructive Testing - an Engineering Approach. *Physical Mesomechanics.* January, 2012.

Bolotina, I., Kröning, M., Reddy, K. M. 2010. NDT and its value for structural safety assessment. *Proceedings of the Conference on Optical Techniques and Nano Tools for Material and Life Sciences ONT4MLS.* Minsk, Belorus. Minsk, Belorus : Stepanov Institute for Physics, Belorussian National Academy of Science, 2010.

Brand, A. 1977. Multi-level adaptive solutions to boundary-value problems. *Mathematics of Computation.* 1977.

Brox, T., Bruhn, A., Papenberg, N., Weickert, J. 2004. High Accuracy Optical Flow Estimation Based on a Theory for Warping. s.l. : Springer, 2004.

Bruhn, A., Weickert, J., Feddern, C., Kohlberger, T., Schnörr, C. 2003. *Variational optic flow computation in real-time.* Saarbrücken, Germany : Dept. of Mathematics, Saarland University,, 2003.

BS7910. 1997. *Guide on methods for assessing the acceptability of flaws in structures.* London : British Standard Institution BSI, 1997.

—. 2005. *Guide on methods for assessing the acceptability of flaws in structures.* s.l. : British Standard Institutions, 2005.

Bulavinov, A. 2005. *Der getaktete Gruppenstrahler (The Sampling Phased Array), Dissertation.* Saarbrücken : University of Saarland, 2005.

—. 2005. *Sampling phased array.* 2005.

Bulavinov, A., Kroening, M., Reddy, K. M. 2007. *Real-Time Quantitative Ultrasonic Inspection.* Buenos Aires : Proceedings of the IV Pan-American Conference for Nondestructive Inspection, 2007.

Cartz, L. 1995. *Nondestrutive Testing: Radiography, Ultrasonics, Liquid Penetrant, Magnetic Particle, Eddy Current.* s.l. : ASM International, 1995.

Chang, Y.F., Ton, R.C. 2001. Kirchhoff Migration of Ultrasonic Images. *Materials Evaluation.* 2001, Vols. 59,3.

Charbonnier, P., Blanc-Feraud, L., Aubert, G., Barlaud M. 1994. Two deterministic halfquadratic regularization algorithms for computed imaging. 1994.

Chiao, R. Y., Thomas, L. J. 1994. Analytical Evaluation of Sampled Aperture Ultrasonic Imaging Techniques for NDE. *IEEE Transactions on Ultrasonics, Ferroelectrics and Frequency Control.* 1994, Vols. 41,4.

Chuse, R., Carson, B. 1993. *Pressure vessels: the ASME code simplefied.* s.l. : McGraw-Hill, 1993.

Cioclov, D. 2005. *FAD for Leight-Weight Structures.* Saarbrücken : private communication, 2005.

Cioclov, D., Dobmann, G., Kröning, M. 2005. Ein Beitrag der quantitativen zfP mit Ultraschall im Zusammenhang mit probabilistischer Bruchmechanik zur Lbensdauerbewertung von Komponenten. [book auth.] Proceedings. *Herausforderungen neuer Werkstoffe an die Forschung und Werkstoffprüfung.* Berlin : s.n., 2005.

Cioclov, D., Kröning, M. 2000. Integration of NDT Reliability into FAD-based Probabilistic Analysis of Pressure Vessel Integrity. [book auth.] ASME PVP 410. *AssessmentMethodologies for Preventing Failure: Deterministic and Probabilistic Aspects and Weld Residual Stress.* s.l. : ASME PVP, 2000.

—. 1999. Probabilistic Fracture Mechanics Approach to Pressure Vessel Reliability Evaluation. [book auth.] Pressure Vessels and Piping Division American Society of American Engineers. *Probabilistic and Environmental Aspects of Fracture and Fatigue, ASME PVP386.* s.l. : ASME PVP, 1999.

Cobb, A.C., Fisher, J., Michaels, J.E. 2009. Model-Assisted Probability of Detection for Ultrasonic Structural Health Monitoring. *Proceedings of he 4th European-American Workshop on Reliability of NDE.* Berlin : s.n., 2009.

Cohen, I. 1993. Nonlinear variational method for optical flow computation. [book auth.] In: Eighth Scandinavian Conference on Image Analysis. Volume 1. 1993.

Condell, J. V., Scotney, B. W., Morrow, P. J. 2006. The effect of presmoothing image sequences on the computation of optical flow. Berlin, Heidelberg : Springer, 2006, pp. 780--791.

Courant, R. 1943. Variational Methods for the Solution of Problems in Equilibrium and Vibrations. *Bull. Amer. Math. Society.* 1943, Vol. 49.

Dalichow, M., Dennis, M., Kröning, M., Mohr, F., Reddy, K. M., Yastrebova, O. 2012. Advances in 3-D Ultrasonic Imaging for Quantitative Flaw Evaluation. *Proceedings of the 9th International Conference on NDE in Relation to Structural Integrity for Nuclear and Pressurized Components.* 2012.

Dalichow, M., Heumüller, R., Kröning, M., Schmid, R. 1986. *Crack depth measurements in stainless steel pipes - methods and reliability.* Erlangen : Siemens Kraftwerk Union AG, 1986.

Dampfkesselbestimmungen. 2004. *Technische Regeln für Dampfkessel (TRD).* Berlin : Verband der technischen Überwachungsvereine e.V., 2004.

De Castro, E., Morandi, C. 1987. *Registration of Translated and Rotated Images Using Finite Fourier Transforms.* 1987.

den Dekker, A. J., van den Bos, A. 1997. Resolution: A Survey. *J. Opt. Soc. Am.* A, 1997, Vol. Vol. 14, No.3.

Deutsch, V. 2000. History of NDT - Instruments. *Proceedings of the 15th World Conference on Nondestructive Testing.* Rome : s.n., 2000.

E. Bray, R. Stanley. 1989. *Nondestructive Evaluation: a Tool in Design, Manufacturing, and Service.* s.l. : Mc Graw-Hill Series in Mechanical Engineering, 1989.

Engl, G. 2011. *Coupling Control by Statistic Analysis of Near Surface Signals.* Erlangen : IntelligeNDT GmbH, 2011.

ENIQ, European Network for Inspection Qualification. 2007. *ENIQ Report 31, 3rd issue.* Brussels : s.n., 2007. EURO 22906 EN.

Ermolov, I. N., Aleshin, N.P., Potapov, A.I. 1991. *Nondestructive testing.* Moscow : Vysshaia shkola, 1991.

Fick, A. 1855. *Poggendorff's Annalen.* 1855.

Froehlinghaus, T., Buhmann, J. 1996. Regularizing phase based stereo. 1996, pp. 451–455.

Fuh, C.-S., Maragos, P. 1989. Region-based optical flow estimation. 1989, pp. 130 - 135 .

Gajewski, D. 2010. *Vorlesungsskript: Angewandte Geophysik II.* Hamburg : Universität Hamburg, 2010.

Galvin B., McCane B., Novins K., Mason D., Mills S. 1998. *Recovering motion fields: an analysis of eight optical flow algorithms.* Southampton, England : s.n., 1998.

Gandossi, L., Simola, K. 2007. *Sensitivity of Risk Reduction to Probability of Detection Curves (PoD) level and Detail.* s.l. : Institute for Energy, 2007. EUR 21902 EN.

Gebhardt, W. 1996. *Einsatz von miniaturisierten Beschleunigungssensoren zur Positionsbestimmung von Ultraschallprüfköpfen.* Saarbrücken : IZFP - Bericht, 1996.

Georgiou, G.A. 2006. *Probability of Detection (PoD) curves - Derivation, Applications and Limitations.* Norwich, UK : HSE Books, 2006.

Georgiou, G.A., Drewry, M., Beye, E. 2006. *Probability of Detection (PoD) Curves - Derivation, Applications and Limitations.* Norwich, UK : Health and Safety Executive HSE, 2006. Research Report 454.

Gherman, B., Mardes, S. 1994. *The Mysterious Rays of Dr. Roentgen.* s.l. : Simom & Schuster Children's Publishing, 1994.

Glasser, O. 1993. *Wilhelm Conrad Roentgen and the early history of the Roentgen rays.* s.l. : Norman Publishing, 1993.

Glocker, B., Komodakis, N., Tziritas, G., Navab, N., Paragios, N. 2008. Dense Image Registration through MRFs and Efficient Linear Programming. 2008.

Green, R. 1981. *Effect of metallic microstructure on ultrasonic attenuation.* s.l. : Metallurgical society of the American Institut of Mechanical Engineers, 1981.

Grimson, W.E.L. 1985. Computational experiments with a feature based stereo algorithm. 1985, pp. 17–34.

Harold, B., Mordfin, L. 1992. *Nondestructive Testing Standards - Present and Future.* s.l. : American Society for Testing and Materials (ASTM), 1992.

Healy, A., Vernal, M. 2002. *A Method for Computing Optical Flow via Graph Cuts.* 2002.

Hellier, Charles J. 2001. *Handbook of Nondestructive Evaluation.* 2001. 0-07-028121-1.

Horn, B., Schunk, B. 1981. *Determining Optical Flow.* s.l. : MIT, 1981. pp. 185–203.

IAEA. 2006. *Fundamental Safety Principles, IAEA Safety Standards Series SF-1.* Vienna : IAEA International Atomic Energy Agency, 2006. 92-0-110706-4.

IRCP, International Commission on Radiological Protection. 2007. *Recommendations of the International Commission on Radiological Protection.* Oxford, UK : Pergamon Press, 2007. IRCP Publication 103.

Kiric, M. 2006. Structural Integrity Assessment Applying Ultrasonic Testing. *Proceedings of the 16th. European Conference on Fracture.* Alexandropolis, Greece : s.n., 2006.

Kiric, M., Kurai, J. 2008. Testing for Detection and Evaluation of Cracks. *The Challenge of Materials and Weldments - Structural Integrity and Life Assessment.* 2008.

Kolmogorov, V., Zabih, R. 2002. *Multi-camera scene reconstruction via graph cuts.* s.l. : Springer, 2002.

Kolsky, H. 1963. *Stress waves in solids.* New York : Dover, 1963.

Kosov, S. 2007. *Multi-view3D reconstruction using variational methods, Master Thesis.* Saarbrücken : UdS, 2007.

Kosov, S., Thormählen, T., Seidel, H. P. 2009. *Accurate Real-Time Disparity Estimation with Variational Methods.* Vegas, USA : s.n., 2009.

Krautkrämer, J., Krautkrämer, H. 1990. *Ultrasonic Testing of Materials.* New York : Springer Verlag, 1990. 3540512314.

Kretov, E. 1995. *Ultrazvukavaya defektoskopiya v energomashinostroenii.* St. Petersburg : Radioavionika, 1995. ISBN 5-88877-001-9.

Kröning, M. 2012. *Denoising of Sector Scans.* Saarbrücken : privatecommunication, 2012.

—. 2011. *Manual Flaw Evaluation.* Saarbrücken : private communication, 2011.

—. 1986. *P-Scan Pipe Inspection, private communication.* Saarbrücken : s.n., 1986.

—. 2011. *Registration Sensitivity and Critical Flaw Dimensions.* Saarbrücken : private Mitteilung, 2011.

—. 1982. *Siemens-KWU NDT Laboratory Report.* Saarbrücken : private communication, 1982.

KTA 3201.4, Sicherheitstechnische Regel des KTA. *KTA 3201.4 Komponenten des Primärkreises von Leichtwasserreaktoren.* s.l. : http://www.kta-gs.de/.

KTA 3211.4, Sicherheitstechnische Regel des KTA. *KTA 3211.4 Druck- und aktivitätsführende Komponenten von Systemen außerhalb des Primärkreises.* s.l. : http://www.kta-gs.de/.

Kuna, M. 2010. *Numerische Beanspruchungsanalyse von Rissen.* s.l. : Vieweg und Teubner Verlag, 2010. 3834810061.

Kurai, J., Kiric, M. 2009. Experience in Nondestructive Testing of Processes. *Security and Reliability of Damaged Structures and Defective Materials.* 2009.

Kußmaul, K. 1984. German Basis Safety Consept Rules out Possibility of Catastrophic Failure. *Nucl. Engineering Int.* 1984.

Larson, (ed.) Brian. 2011. *Introduction to Ultrasonic Testing.* Ames, IO, USA : NDT Education Resource Center, Iowa State University, 2011. www.ndt-ed.org.

Li, G., Zucker, S.W. 2006. Differential geometric consistency extends stereo to curved surfaces. s.l. : Springer, 2006, pp. 44–57.

Li, Y. 2011. *Development of a Robot-Based Magnetic Flux Leakage Inspection System.* Saarbrücken : Universität des Saarlandes, 2011. Dissertation.

Lifsitz, I., Parkomovskii, G. 1950. *Theory of propagation of ultrasonic waves in polycrystals.* Moscow : Nauka, Eksperimentalnaya i teoreticheskaya fizika, 1950.

Lober, D. 2011. *Metallograf.* s.l. : www.metallograf.de, 2011.

Lücke, K. 1956. *Ultrasonic Attenuation caused by thermoelastic heat flow.* New York : American institut of physics, 1956. Vol. 27.

Mansouri, A., Mitiche, A., Konrad, J. 1998. *Selective image diffusion: application to disparity estimation.* Chicago, IL : s.n., 1998. pp. 284–288.

Mason, W. 1958. *Physical acoustic and the properties of solids.* Princeton : D. van Nostrand company, 1958.

Mason, W., McSkimin, H. 1948. *Energy losses of sound waves in metals due to scattering and diffusion.* s.l. : Journal of the Acoustical Society of America, 1948.

Mechel, F.P., Munjal, M. L. , Vorländer, M., Költzsch, P., Ochmann, M., Cummings, A., Maysenhölder, W., Arnold, W. 2008. *Formulas in Acoustics.* s.l. : Springer, 2008.

Mèmin, E., Pèrez, P. 1998. A multigrid approach for hierarchical motion estimation. Bombay, India : Narosa Publishing House, 1998, pp. 933–938.

Meyer, P., Anderson, J.W. 2000. Ultrasonic Testing Using Phased Arrays. *Proceedings of 15th World Conference on Nondestructive Testing.* Rome : s.n., 2000.

Microsoft. 1999. *Microsoft Press Release.* 1999.

MIL-HDBK-1823. 1999. *Nondestructive Evaluation System Reliability Assessment.* 1999.

Mischerwelding. 2011. Pipe System. *www.mischerwelding.sk/praceen.html.* 2011.

Moles, M.D.C. 2007. *Advances in Phased Array Ultrasonic Technology Applications.* Waltham, MA : Olympus NDT, 2007. 0-9735933-4-2.

MPA. 2011. *Metallographie 100 online.* Stuttgart : Materialprüfanstalt Stuttgart, 2011.

Müller, C., Elaguine, M., Bellon, C., Ewert, U., Zscherpel, U., Schmach, M., Redmer, B., Ryden, M., Ronneteg, U. 2006. PoD (Probability of Detection) Evaluation of NDT Techniques for Cu-Canisters for Risk Assessment of Nuclear Waste Encapsulation. [book auth.] ECNDT 2006. *Proceedings of the ECNDT.* Berlin : s.n., 2006.

Müller, W., Schmitz, V., Schäfer, G. 1988. Reconstruction by the Synthetic Aperture Focusing Technique. *Nuclear Engineering and Design, Proceedings.* 1988.

Nuclear, Electric. *Assessment of the integrity of structures containing defects, R/H/R6 Revision 3.* Barnwood, Gloustershire : Nuclear Electric.

Olympus. 2011. *Olympus Technical Notes - Ultrasonic Transducers.* s.l. : Olympus, 2011.

Papadakis, E.P. 1999. *Ultrasonic Instruments and Devices.* s.l. : Academic Press, 1999.

Perona, P., Malik, J. 1990. Scale-space and edge detection using anisotropic diffusion. 1990, pp. 629–639.

Personalzertifizierung, DGZFP. 2008. *Zerstörungsfreie Prüfung - Qualifizierung und Zertifizierung von Personal der zerstörungsfreien Prüfung - Allgemeine Grundlagen; Deutsche Fassung EN 473:2008 DIN EN-473.* Berlin : s.n., 2008.

PISC II, Programme for the Inspection of Steel Components. 1986. *The Round Robin Test of the PISC II Programme: Plates and Ultrasonic Procedures Used.* Brussels : European Programme for the Inspection of Steel Components (PISC); Nuclear Energy Agency, Committee on the Safety of Nuclear Installations, 1986. CSNI No. 118.

P-scan. 2011. P- scan. *www.p-scan.dk.* [Online] Force Technology, Denmark, 2011. http://www.p-scan.dk.

Pudovikov, S., Bulavinov, A., Kröning, M. 2008. Ultrasonic Inspectability of Austenitic Steel and Dissimilar Weld Joints. *Proceedings of the 34. MPA Seminar "Werkstoff- & Bauteilverhalten in der Energie- & Anlagentechnik.* 2008.

Pudovikov, S., Bulavinov, A., Pinchuk, R., Ramanan, S.V. 2010. Quantitative Ultraschallprüfungen an anisotropen Materialien mittels Sampling Phased Array Technik. 2010, DGZfp.

Razvan, R. 2009. Some remarks on the history of fracture mechanics. [book auth.] ASM '09. *Proceedings of the 3rd International Conference on Applied Mathematics, Simulation, Modelling.* 2009.

Reddy, K.M. 2011. *Simulation Tools for Ultrasonic Testing (private communication).* Chennai : Lucidsoft, 2011.

—. 2011. *Ultrasonic Imaging (private communication).* Chennai : Lucidsoft, 2011.

Rihar, G. 2000. Lack of Fusion in Welded Joints. *Proceedings of the 15th World Conference on Nondestructive Testing.* Rome, Italy : s.n., 2000.

Rockstroh, B., Kappes W., Walte, F., Bessert, S., Montnacher, J., Nemec, D, Goetz. J., Herrmann, W., Krefeld D.B., Schatto H-J., Gohlke, B., Gerken, C. 2005. *Optimierte Prüfsysteme für Eisenbahnräder und Radsätze.* Rostock : DGZfP, 2005.

Rummel, W.D. 1998. *Probability of Detection as a Quantitative Measure of Nondestructive Testing.* www.asnt.org : ASNT Back to Basics, 1998.

—. 2008. *Probability of Detection As a Quantitative Measure of Nondestructive Testing End-to-End Process Capability.* www.asnt.org/publications/materialseval/basics/Jan98 : The American Society for Nondestructive Testing, 2008.

Sackenreuther, H., Maurer, A., Koch, R. 2009. Industrieller Einsatz von synchronisierten standard Knickarm-Robotern in Verbindung mit neuester Gruppenstrahlertechnik. [book auth.] DGzfP Deutsche Gesellschaft für zerstörungsfreie Prüfung. *Proceedings of the Annual German NDT Conference.* s.l. : DGzfP, 2009.

Salecker, G. 1996. *Disaster on the Mississippi: The Sultana Explosion April 27, 1865.* s.l. : Naval Institute Press, 1996.

Sava, P., Yan, J. 2008. Isotropic angle-domain elastic reverse-time migration. *Geophysics 73.* Nr. 6, 2008, Vols. pp 229-239.

Scharstein, D., Szeliski, R. 2002. *A taxonomy and evaluation of dense two-frame stereo correspondence algorithms.* 2002. pp. 7–42.

Schneiden-Schweißen-Heft-2. 1974. Erstarrungsgefüge und Textur von Schmelzschweißplattierungen aus Chrom-Nickel-Stählen für Kernreaktorkomponenten. *Schneiden und Schweißen, Heft 2.* 1974.

Schnörr, C. 1994. Segmentation of visual motion by minimizing convex non-quadratic functionals. *In: Twelfth International Conference on Pattern Recognition. Volume A., Jerusalem, Israel, IEEE Computer Society Press.* 1994.

Selby, G. 2011. *xLPR: Extremely Low Probability of Rupture - NDE integration into probabilistic fracture mechanics.* Recife : CAND Rio de Janeiro, 2011. CAND week, November 2011.

Serabian, S. 1980. *Frequency and grain size dependency of ultrasonic attenuation in polycrystalline materials.* s.l. : British Journal of Non-Destructive Testing, 1980. Vol. 22.

Silk, M.G., Stoneham, A.M., Temple, J.A.G. 1987. *The Reliability of Non-destructive Inspection.* Bristol : Adam Hilger, 1987.

Slesareva, N., Bruhn, A, Weickert, J. 2005. *Optical flow goes stereo: A variational method for estimating discontinuity-preserving dense disparity maps.* 2005.

SNT. 2001. *Recommended Practice No. SNT-TC-1A.* s.l. : American Society for Nondestructive Testing, 2001.

Sokoloff, S.Y. 1937. *Means for indicating flaws in materials.* s.l. : United States Patent 2164125, 1937.

Spears, W., Hamann, J., Maxim, P., Kunkel, T, Heil, R., Zarzhitsky, D., Spears, D., Karlsson, C. *Where are you?* Laramie : Computer Science Department, University of Wyoming.

Stephens, R.I., Fuchs, H.O. 2001. *Metal Fatigue in Engineering.* s.l. : John Wiley and Son, 2001.

Subra, S. 2003. *Fatigue of Materials.* s.l. : The Press Syndicate of the University of Cambridge, 2003.

SwRI. 1978. *News Release.* San Antonio, Texas, USA : Southwest Research Institute, 1978.

Totemeier, T.C., Gale, W.F. 2004. *Smittells Metals Reference Book.* Burlington, MA : Elsevier Butterworth-Heineman, 2004.

Vary, A. 1988. *Concepts for interrelating ultrasonic attenuation, microstructure and fracture toughness in polycrystalline solids.* s.l. : Material Evaluation, American society for Nondestructive testing, 1988. Vol. 46.

von Bernus, L., Bulavinov, A., Dalichow, M., Joneit, D., Kröning, M., Reddy, K. M. 2006. Sampling Phased Array: A New Technique for Signal Processing and Ultrasonic Imaging. *Insight.* 2006, Vols. 48, 9.

W.M. Brown, J.L. Walker, and W.R. Boario. 2004. Sighted Automation and Fine Resolution Imaging. *IEEE Transactions on Aerospace and Electronic Systems.* 2004, Vol. 40, 4, pp 1426 - 1445.

Wang, C.-Y., Achenbach, J. D., Hirose, S. 1996. Two-Dimensional Time Domain BEM for Scatteringof Elastic Waves in Solids of General Anisotropy. *International Journal Solids.* 1996, Vol. 33, 26.

Weber, F. 1963. *Zur Geschichte der deutschen Dampfkessel-Bestimmungen: hundert Jahre Ringen um eine industrielle Selbstverwaltung.* s.l. : VDI, Verein Deutscher Ingenieure, 1963.

Weickert, J. 1998. *Anisotropic diffusion in Image Processing.* s.l. : Teubner-Verlag, 1998.

Weickert, J., Bruhn, A., Schnörr, C. 2003. Lucas/Kanade meets Horn/Schunck: Combining local and global optic flow methods. Saarbrücken, Germany : Dept. of Mathematics, Saarland University, 2003.

Weickert, J., Schnörr C. 2001. A theoretical framework for convex regularizers in pde-based computation of image motion. *Int. J. Comput. Vision.* 2001.

Wikipedia. 2011. *Linear Elasticity, http://en.wikipedia.org/wiki/Linear elasticity [Online].* 2011.

—. 2011. *Optical Mouse, en.wikipedia.org/wiki/optical_mouse [Online].* s.l. : Internet, 2011.

—. 2012. *Phase Correlation, http://en.wikipeda.org/wiki/Phase_correlation [Online].* s.l. : Wikipedia, 2012. Vol. http://en.wikipeda.org/wiki/Phase_correlation.

—. 2011. *Ultrasound, http://en.wikipedia.org/wiki/Ultrasound [Online]*. 2011.

Wöhler, A. 1855. Theorie rechteckiger eiserner Brückenbalken mit Gitterwänden und mit Blechwänden. *Zeitschrift für das Bauwesen.* 1855.

Wolfram, Demonstration Project. 2011. *Anisotropic Elasticity, http://demonstrations.wolfram.com/Anisotropic Elasticity [Online]*. 2011.

Workman, G. L., Kishoni, D., Moore P.O. 2007. *Ultrasonic Testing.* s.l. : American Society for Nondestructive Testing, 2007. ISBN: 978-1-57117-105-4.

Xiao, J., Cheng, H., Sawhney, H., Rao, C., Isnardi, M. 2006. Bilateral Filtering-based Optical Flow Estimation with Occlusion Detection. 2006.

Yastrebova, O., Kröning, M., Bulavinov, A. 2008. *Real-time Measurement of Relative Sensor Position Changes using Ultrasonic Signal Evaluation.* Stuttgart : 34. MPA-Seminar, 2008.

Young, D. 1971. Iterative Solution of Large Linear Systems. New York : Academic Press, 1971.

Zhantlessov, Y. 2012. *Ultraschalltomographie mit verteilten Elementen in einer synthetischen Apertur, Dissertation (to be submitted).* Saarbrücken : Universität des Saarlandes, 2012.

Zimmer, H., Bruhn, A., Valgaerts, L., Breuß, M., Weickert, J., Rosenhahn, B., Seidel, H.P. 2008. *PDE-Based Anisotropic Disparity-Driven Stereo Vision.* 2008.

List of Figures

List of Tables